

TWO-DIMENSIONAL DAM BREAK ANALYSES OF BERDAN DAM

A THESIS SUBMITTED TO
THE GRADUATE SCHOOL OF NATURAL AND APPLIED SCIENCES
OF
MIDDLE EAST TECHNICAL UNIVERSITY

BY

ÇAĞLA IRMAK ÜNAL

IN PARTIAL FULFILLMENT OF THE REQUIREMENTS
FOR
THE DEGREE OF MASTER OF SCIENCE
IN
CIVIL ENGINEERING

SEPTEMBER 2019

Approval of the thesis:

TWO-DIMENSIONAL DAM BREAK ANALYSES OF BERDAN DAM

submitted by **ÇAĞLA IRMAK ÜNAL** in partial fulfillment of the requirements for the degree of **Master of Science in Civil Engineering Department, Middle East Technical University** by,

Prof. Dr. Halil Kalıpçılar
Dean, Graduate School of **Natural and Applied Sciences**

Prof. Dr. Ahmet Türer
Head of Department, **Civil Engineering**

Prof. Dr. Zafer Bozkuş
Supervisor, **Civil Engineering, METU**

Examining Committee Members:

Prof. Dr. İsmail Aydın
Civil Engineering, METU

Prof. Dr. Zafer Bozkuş
Civil Engineering, METU

Prof. Dr. Mete Köken
Civil Engineering, METU

Assoc. Prof. Dr. Yakup Darama
Civil Engineering, Atılım University

Assist. Prof. Dr. Elif Oğuz
Civil Engineering, METU

Date: 04.09.2019

I hereby declare that all information in this document has been obtained and presented in accordance with academic rules and ethical conduct. I also declare that, as required by these rules and conduct, I have fully cited and referenced all material and results that are not original to this work.

Name, Surname: Çaęla Irmak Ünal

Signature:

ABSTRACT

TWO-DIMENSIONAL DAM BREAK ANALYSES OF BERDAN DAM

Ünal, Çağla Irmak
Master of Science, Civil Engineering
Supervisor: Prof. Dr. Zafer Bozkuş

September 2019, 129 pages

Dam break analyses of Berdan Dam were performed to determine the potential risk areas of floodplain and to help the preparation of emergency action plans. Digital elevation model created from bathymetric maps, flow hydrograph obtained for catastrophic condition, and sub-regions classified by land cover maps were integrated into HEC-RAS model. The reservoir of Berdan Dam and two-dimensional flow area was created on GIS-based geometric data which was converted from the digital elevation model to a triangulated irregular network. Breach parameters were calculated according to the selected dam breach mechanism. When all hydraulic and hydrological parameters were specified depending on variables and selected dam breach mechanism, simulations were run under piping and overtopping scenarios. Finally, the flood inundation maps were visualized on the digital elevation model with the help of RAS-Mapper in terms of depth, velocity, water surface elevation, and flood arrival time.

Keywords: Dam break analysis, HEC-RAS, GIS, two-dimensional model, inundation mapping

ÖZ

BERDAN BARAJI'NIN İKİ BOYUTLU YIKILMA ANALİZLERİ

Ünal, Çağla Irmak
Yüksek Lisans, İnşaat Mühendisliği
Tez Danışmanı: Prof. Dr. Zafer Bozkuş

Eylül 2019, 129 sayfa

Berdan Barajı'nın baraj yıkılma analizleri, taşkın yatağındaki potansiyel risk alanlarını belirlemek ve acil eylem planlarının hazırlanmasına yardımcı olmak amacıyla yapılmıştır. Batimetri haritalarından elde edilen dijital yükseklik modeli, katastrofik durum için elde edilen hidrograf ve arazi kullanım haritaları ile sınıflandırılan alt bölgeler HEC-RAS'ta iki boyutlu bir model üzerinde birleştirilmiştir. Dijital yükseklik haritasından düzensiz üçgen ağına dönüştürülen CBS tabanlı geometrik veri üzerinde Berdan Barajı'nın rezervuarı ve iki boyutlu akış alanı oluşturulmuştur. Seçilen baraj yıkılma mekanizmasına göre yıkılma parametreleri hesaplanmıştır. Bütün hidrolik ve hidrolojik parametreler seçilen çözüm metoduna bağlı olarak saptandıktan sonra, borulanma ve aşma yıkılma modlarına göre simulasyon tamamlanmıştır. Son olarak, taşkın yayılım haritaları hız, derinlik, su yüksekliği ve taşkın geliş süresi dağılımları olarak dijital yükseklik haritasının üzerinde RAS- Mapper aracılığıyla görüntülenmiştir.

Anahtar Kelimeler: Baraj yıkılma analizi, HEC-RAS, CBS, iki boyutlu model, taşkın yayılım haritası

To my dear grandmother Hatice Özbudak

ACKNOWLEDGEMENTS

First and foremost, I would like to express my gratitude to my precious mentor and advisor Prof. Dr. Zafer Bozkuş who provided unique support from the beginning to the end of this study. He changed my point of view with his constructive criticism and made a great contribution by finding solutions to the difficulties that I encountered.

I would like to thank the jury members of my thesis, Prof. Dr. İsmail Aydın, Prof. Dr. Mete Köken, Assoc. Prof. Dr. Yakup Darama, and Assist. Prof. Dr. Elif Oğuz for their contributions and interest in my work.

I would like to thank Suiş Proje team for their valuable contributions to this study. Numeric data of basic inputs were provided by them. In particular, I wish to thank my esteemed colleague Okan Çağrı Bozkurt. He shared all of his engineering knowledge and experience with me throughout this study.

Special mention goes to Abiddin Berhan Melek, Ezgi Budak, Meriç Kiranoğlu and Yankı Yolsever for their helpfulness and friendship. I deeply appreciate them not only for contributions to this work but also for their presence enlightening my life.

Lastly but not least, I would like to express my sincere gratitude to my family members who were always there for me. I am grateful to my dear parents Cemal and Cemile for their patience and full support. I would also like to thank my dear brother Cem Doruk for his mind-opening ideas and joyful moments we shared. They always believed in me and encouraged me to continue. This thesis would not have been possible without them.

TABLE OF CONTENTS

| | |
|--|-------|
| ABSTRACT | v |
| ÖZ | vi |
| ACKNOWLEDGEMENTS | viii |
| TABLE OF CONTENTS | ix |
| LIST OF TABLES | xii |
| LIST OF FIGURES | xiv |
| LIST OF ABBREVIATIONS | xviii |
| LIST OF SYMBOLS | xix |
| CHAPTERS | |
| 1. INTRODUCTION | 1 |
| 1.1. General Overview of Dam Break Modeling | 1 |
| 1.2. Literature Review | 3 |
| 1.3. The Objective of the Study | 9 |
| 1.4. Thesis Organization | 9 |
| 2. HYDRAULIC MODEL | 11 |
| 2.1. Hydraulic Model of HEC-RAS | 11 |
| 2.1.1. Discretization of Two-Dimensional Unsteady Flow Equations | 11 |
| 2.1.2. Sub-grid Bathymetry Approach | 12 |
| 2.1.3. Two-dimensional Shallow Water Equations | 13 |
| 2.1.4. Diffusion Wave Approximation | 14 |
| 2.2. Application of Numerical Methods | 15 |
| 2.2.1. Finite Difference Approximation | 15 |

| | |
|--|----|
| 2.2.2. Finite Volume Approximation | 16 |
| 2.2.3. Hybrid Discretization | 17 |
| 2.2.4. Discrete Scheme of Numerical Solver | 18 |
| 2.3. Solution Algorithm of HEC-RAS | 20 |
| 2.3.1. Calculation of Water Surface Elevation | 20 |
| 2.3.2. Complete Solution Procedure..... | 20 |
| 3. TWO-DIMENSIONAL DAM BREAK MODEL OF BERDAN DAM..... | 23 |
| 3.1. The Study Area | 23 |
| 3.1.1. General Characteristics of the Study Area | 23 |
| 3.1.2. Dam Characteristics | 26 |
| 3.2. Two-Dimensional Dam Break Model in HEC-RAS..... | 27 |
| 3.2.1. Integration of Geometric Data..... | 28 |
| 3.2.2. Determination of Reservoir Storage Area and 2D Flow Area | 30 |
| 3.2.3. Manning’s Roughness Coefficient of 2D Flow Area..... | 33 |
| 3.2.4. Determination of Mesh Size and Computational Time Interval | 37 |
| 3.2.5. Maximum Possible Discharge for Catastrophic Condition..... | 41 |
| 3.2.6. Dam Breach Parameters | 42 |
| 3.3. Complete Procedure of 2D Dam Break Analyses with HEC-RAS | 47 |
| 4. TWO-DIMENSIONAL DAM BREAK ANALYSES | 51 |
| 4.1. Dam Break Analyses..... | 51 |
| 4.2. Results of the Analyses with Piping Mode of Failure | 51 |
| 4.2.1. Flood Inundation for the Piping Elevation of 30 m with $0.80 \cdot n$ | 57 |
| 4.2.2. Flood Inundation for the Piping Elevation of 30 m with n | 60 |
| 4.2.3. Flood Inundation for the Piping Elevation of 30 m with $1.20 \cdot n$ | 63 |

| | |
|---|-----|
| 4.2.4. Flood Inundation for the Piping Elevation of 30 m with $n=0.060$ | 66 |
| 4.3. Results of the Analyses with Overtopping Mode of Failure | 71 |
| 4.3.1. Flood Inundation for Initial Water Level of 72 m with $0.80 \times \text{base } n$ | 76 |
| 4.3.2. Flood Inundation for Initial Water Level of 72 m with base n | 79 |
| 4.3.3. Flood Inundation for Initial Water Level of 72 m with $1.20 \times \text{base } n$ | 82 |
| 4.3.4. Flood Inundation for Initial Water Level of 72 m with $n=0.060$ | 85 |
| 4.4. Comparison of the Results for Settlement Area | 92 |
| 5. CONCLUSIONS | 95 |
| 5.1. Results of the Analyses | 95 |
| 5.2. Recommendations for Future Works | 97 |
| REFERENCES..... | 99 |
| APPENDICES | 103 |
| A. Details of Inputs of the Analyses | 103 |
| B. Results of the Analyses for Different Piping Elevations with Base n | 113 |
| C. Results of the Analyses for Different Initial Water Levels with Base n | 119 |
| D. Results of the Analyses for Different Initial Water Levels with $n=0.060$ | 125 |

LIST OF TABLES

TABLES

| | |
|--|----|
| Table 3.1. Characteristics of dam body | 26 |
| Table 3.2. Characteristics of Berdan reservoir | 27 |
| Table 3.3. Sub-regions and corresponding roughness coefficient values..... | 34 |
| Table 3.4. Manning’s roughness coefficient values used in analyses | 36 |
| Table 3.5. Dam breach mechanisms in HEC-RAS | 44 |
| Table 4.1. Maximum values for different piping elevations with base n at 2500 m away from the dam..... | 68 |
| Table 4.2. Maximum values for different piping elevations with base n at 3500 m away from the dam..... | 69 |
| Table 4.3. Maximum values for different piping elevations with base n at 5000 m away from the dam..... | 69 |
| Table 4.4. Comparison of maximum depths for piping..... | 70 |
| Table 4.5. Comparison of maximum WSE values for piping..... | 70 |
| Table 4.6. Comparison of maximum velocities for piping..... | 70 |
| Table 4.7. Maximum values for different initial water levels with $n=0.060$ at 2500 m away from the dam | 87 |
| Table 4.8. Maximum values for different initial water levels with base n at 2500 m away from the dam | 88 |
| Table 4.9. Maximum values for different initial water levels with $n=0.060$ at 3500 m away from the dam | 88 |
| Table 4.10. Maximum values for different initial water levels with base n at 3500 m away from the dam | 89 |
| Table 4.11. Maximum values for different initial water levels with $n=0.060$ at 5000 m away from the dam | 89 |

| | |
|--|----|
| Table 4.12. Maximum values for different initial water levels with base n at 5000 m away from the dam..... | 90 |
| Table 4.13. Comparison of maximum depths for overtopping | 90 |
| Table 4.14. Comparison of maximum WSE values for overtopping..... | 91 |
| Table 4.15. Comparison of maximum velocities for overtopping | 91 |
| Table 4.16. Comparison of maximum depths for piping and overtopping in the residential area | 93 |

LIST OF FIGURES

FIGURES

| | |
|--|----|
| Figure 2.1. Representation of computational grid with sub-grid bathymetry data.... | 13 |
| Figure 2.2. Representation of dual grid cell | 16 |
| Figure 2.3. Solution algorithm of HEC-RAS | 21 |
| Figure 3.1. Location of the study area | 23 |
| Figure 3.2. Tarsus district and Berdan Dam | 24 |
| Figure 3.3. Settlement Area | 25 |
| Figure 3.4. Digital Elevation Model (DEM) | 29 |
| Figure 3.5. Triangulated Irregular Network (TIN) | 29 |
| Figure 3.6. Reservoir and 2D flow area..... | 30 |
| Figure 3.7. The elevation-area-volume relationship of the reservoir of Berdan Dam | 31 |
| Figure 3.8. Integration of elevation-volume relationship into the model | 32 |
| Figure 3.9. Volume - elevation curve of Berdan reservoir | 32 |
| Figure 3.10. Sub-regions for different Manning's roughness coefficient in ArcGIS | 33 |
| Figure 3.11. Classification of sub-regions in RAS-Mapper | 34 |
| Figure 3.12. Sub-regions of the 2D flow area | 35 |
| Figure 3.13. Water surface elevation values for different mesh sizes | 38 |
| Figure 3.14. Mesh generation for 2D flow area..... | 39 |
| Figure 3.15. Mesh refinement in the vicinity of Berdan Dam..... | 39 |
| Figure 3.16. Map values of maximum velocity near Berdan Dam..... | 40 |
| Figure 3.17. Inflow and outflow hydrographs | 42 |
| Figure 3.18. Parameters of a trapezoidal breach (Bozkuş & Bağ, 2011) | 43 |
| Figure 3.19. Breach geometry at the connection | 46 |
| Figure 3.20. Breach progression curve | 46 |
| Figure 3.21. Calculated breach parameters for different mechanisms | 47 |

| | |
|---|----|
| Figure 3.22. Process chart of dam break analyses | 49 |
| Figure 4.1. A cross-section which is 2500 m away from the dam body | 52 |
| Figure 4.2. A cross-section which is 3500 m away from the dam body | 52 |
| Figure 4.3. A cross-section which is 5000 m away from the dam body | 53 |
| Figure 4.4. Maximum WSE values for different piping elevations with base n | 54 |
| Figure 4.5. Maximum velocities for different piping elevations with base n | 56 |
| Figure 4.6. Distribution of maximum depth for the piping elevation of 30 m with 0.80*base n..... | 57 |
| Figure 4.7. Distribution of maximum WSE for the piping elevation of 30 m with 0.80*base n..... | 58 |
| Figure 4.8. Distribution of maximum velocity for the piping elevation of 30 m with 0.80*base n..... | 58 |
| Figure 4.9. Distribution of flood arrival time for the piping elevation of 30 m with 0.80*base n..... | 59 |
| Figure 4.10. Distribution of maximum depth for the piping elevation of 30 m with base n..... | 60 |
| Figure 4.11. Distribution of maximum water surface elevation for the piping elevation of 30 m with base n | 61 |
| Figure 4.12. Distribution of maximum velocity for the piping elevation of 30 m with base n..... | 61 |
| Figure 4.13. Distribution of flood arrival time for the piping elevation of 30 m with base n..... | 62 |
| Figure 4.14. Distribution of maximum depth for the piping elevation of 30 m with 1.20*base n..... | 63 |
| Figure 4.15. Distribution of maximum water surface elevation for the piping elevation of 30 m with 1.20*base n | 64 |
| Figure 4.16. Distribution of maximum velocity for the piping elevation of 30 m with 1.20*base n..... | 64 |
| Figure 4.17. Distribution of flood arrival time for the piping elevation of 30 m with 1.20*base n..... | 65 |

| | |
|---|----|
| Figure 4.18. Distribution of maximum depth for the piping elevation of 30 m with $n=0.060$ | 66 |
| Figure 4.19. Distribution of maximum water surface elevation for the piping elevation of 30 m with $n=0.060$ | 67 |
| Figure 4.20. Distribution of maximum velocity for the piping elevation of 30 m with $n=0.060$ | 67 |
| Figure 4.21. Distribution of flood arrival time for the piping elevation of 30 m with $n=0.060$ | 68 |
| Figure 4.22. Maximum WSE values for different initial water levels with base n ... | 72 |
| Figure 4.23. Maximum velocities for different initial water levels with base n | 73 |
| Figure 4.24. Maximum WSE values for different initial water levels with $n=0.060$ | 74 |
| Figure 4.25. Maximum velocities for different initial water levels with $n=0.060$ | 75 |
| Figure 4.26. Distribution of maximum depth for initial water elevation of 72 m with $0.80 \cdot \text{base } n$ | 76 |
| Figure 4.27. Distribution of maximum water surface elevation for initial water elevation of 72 m with $0.80 \cdot \text{base } n$ | 77 |
| Figure 4.28. Distribution of maximum velocity for initial water elevation of 72 m with $0.80 \cdot \text{base } n$ | 77 |
| Figure 4.29. Distribution of flood arrival time for initial water elevation of 72 m with $0.80 \cdot \text{base } n$ | 78 |
| Figure 4.30. Distribution of maximum depth for initial water elevation of 72 m with base n | 79 |
| Figure 4.31. Distribution of maximum water surface elevation for initial water elevation of 72 m with base n | 80 |
| Figure 4.32. Distribution of maximum velocity for initial water elevation of 72 m with base n | 80 |
| Figure 4.33. Distribution of flood arrival time for initial water elevation of 72 m with base n | 81 |
| Figure 4.34. Distribution of maximum depth for initial water elevation of 72 m with $1.20 \cdot \text{base } n$ | 82 |

| | |
|--|----|
| Figure 4.35. Distribution of maximum water surface elevation for initial water elevation of 72 m with $1.20 \cdot n$ | 83 |
| Figure 4.36. Distribution of maximum velocity for initial water elevation of 72 m with $1.20 \cdot n$ | 83 |
| Figure 4.37. Distribution of flood arrival time for initial water elevation of 72 m with $1.20 \cdot n$ | 84 |
| Figure 4.38. Distribution of maximum depth for initial water elevation of 72 m with $n=0.060$ | 85 |
| Figure 4.39. Distribution of maximum water surface elevation for initial water elevation of 72 m with $n=0.060$ | 86 |
| Figure 4.40. Distribution of maximum velocity for initial water elevation of 72 m with $n=0.060$ | 86 |
| Figure 4.41. Distribution of maximum velocity for initial water elevation of 72 m with $n=0.060$ | 87 |
| Figure 4.42. Distributions of maximum water surface elevation for piping and overtopping modes of failure | 92 |

LIST OF ABBREVIATIONS

ABBREVIATIONS

DEM: Digital Elevation Model

GIS: Geographic Information System

HEC-RAS: Hydrologic Engineering Center – River Analysis System

TIN: Triangulated Irregular Network

USGS: United States Geological Survey

UTM: Universal Transverse Mercator

WGS: World Geodetic System

WSE: Water Surface Elevation

LIST OF SYMBOLS

SYMBOLS

S_f : friction slope

u : velocity term in x-direction (m/s)

v : velocity term in y-direction (m/s)

g : gravitational acceleration (m/s²)

ν_t : horizontal eddy viscosity coefficient

c_f : bottom friction coefficient

R : hydraulic radius (m)

f : Coriolis parameter

∇ : the vector of cell volumes (m³)

I_{avg} : average inflow rate (m³/s)

O_{avg} : average outflow rate (m³/s)

S : reservoir volume (m³)

n : Manning's roughness coefficient

B_{ave} : average breach width (m)

V_w : reservoir volume at the time of failure (m³)

V_{er} : volume of eroded material (m³)

V_{out} : volume of water that passes through the breach (m³)

W_b : bottom width of the breach (m)

h_b : height of the final breach (m)

h_0 : height of the breach base at an instant during the breach formation (m)

h_w : depth of water above the bottom of the breach (m)

t_f : breach formation time (hr)

C_b : coefficient which is a function of reservoir size

z : side slope of the breach

CHAPTER 1

INTRODUCTION

1.1. General Overview of Dam Break Modeling

In general, dam break analysis is performed by taking into consideration the requirements of the case study, the type, and qualification of the available data, the basic characteristics of the study area and the case-specific assumptions. Physical and numerical analysis methods which are developed for dam break phenomenon are applied with different approaches of specific dam breach mechanisms. There may be some limitations regarding computational time and costs considering the feasibility of hydraulic modeling. Thus, one- and two-dimensional models come into prominence in practical applications.

In one-dimensional models, unsteady flow computations are performed by one-dimensional Saint Venant equations at determined channel cross-sections with proper internal and external boundary conditions (Bozkuş, 2003; Bozkuş & Bağ, 2011; Bozkuş & Güner, 2001; Bozkuş & Kasap, 1998). The solution algorithms of software generally use governing equations of 1D flow. FLDWAV, SMPDBK, HEC-RAS, and MIKE11 are among the software most preferred and verified by the many studies.

On the other hand, in two-dimensional models in which flood spreads both over the river channel and the floodplain, the flood inundation map is investigated on a 2D flow area. In this manner, a 2D computational mesh that comprises the properties of terrain can be constructed. Then, a finite volume algorithm is introduced in order to solve the two-dimensional form of Saint Venant or Diffusion Wave equations which are represented as the fully dynamic and diffusive wave approaches, respectively (Altınakar, Mcgrath, Ramalingam, & Omari, 2010; Bates, Anderson, Baird, Walling, & Simm, 1992; Horritt & Bates, 2002; Neelz & Pender, 2009; Soulis, 1992). Different

2D equation sets are solved by frequently used software such as LISFLOOD-FP, HEC-RAS, TELEMAC-2D FLO-2D, MIKE 21.

Combined 1D-2D models can also be created by considering the computational costs. Large river systems can be analysed by using a one-dimensional model at river cross-sections and a two-dimensional model in the inundation areas where more detailed hydrodynamic computations are required (Brunner, Piper, Jensen, & Chacon, 2015). HEC-RAS 5.0.3, which was developed by the U.S. Army Corps of Engineers, is verified by numerous one- and two-dimensional studies. In addition, HEC-RAS is widely used in dam break analyses and flood inundation mapping since it is well integrated into GIS.

One-dimensional models are said to be sufficient for most of the dam break analyses. However, the results of the one-dimensional analysis are obtained only for determined cross-sections along the river. Therefore, the interpolation of cross-sections is required in inundation areas where 2D flow occurs. Besides, Qi & Altinakar (2012) stated that two-dimensional studies are generally more appropriate for highly unsteady dam break floods on wide and flat terrains by considering the rapidly varied flow which may lead to serious the stability and accuracy problems in a 1D analysis.

1.2. Literature Review

Dam breach mechanisms and related mathematical expressions have been developed with the analysis of physical and numerical models. These expressions are integrated into the solution algorithms of the software. Flood routing models have started to be used extensively in practical applications with the development of computational facilities of GIS-based software. Some of these studies were investigated to determine the parameters which are generally used in dam break analysis.

Ackerman & Brunner (2008) simulated a dam break analysis in HEC-RAS to investigate the flood inundation in the downstream region. The digital elevation model was converted to a triangulated network map so that it can be imported from Hec-GeoRAS to HEC-RAS as geometric information. An unsteady flow model was created with determined breach parameters. Finally, dam break analysis was carried out in HEC-RAS and results were mapped by means of GIS. Thus, the processed digital terrain and the resulting water surface profile made the preliminary study of flood risk available. The proper mapping of dam break flood scenarios was stated to facilitate the planning of land use and preparation of emergency plans to prevent loss of life and property.

Goodell & Wahlin (2009) compared the two drawdown methods with the help of HEC-RAS and HEC-HMS for dam breach analysis. Although providing accurate and precise data, the dynamic routing method was specified as a complex method that has disadvantages of requiring a bathymetric map of the reservoir and being more prone to instability problems. On the other hand, level pool drawdown was determined as a simple and practical method that requires only a stage-storage curve and has numeric stability under certain circumstances for many cases. Therefore, by using basic characteristic parameters of breach formation and reservoir, a practical method was presented with compiled results on an envelope curve to determine if level pool reservoir routing would be appropriate and adequate for the analysis.

Wahl (2010) noted that the determination of the outflow hydrograph of reservoir and routing of that hydrograph through the downstream region were essential steps of dam failure analysis. A general overview of both simple and more complex methods was provided to predict the probable outcomes of different flood scenarios according to the required level of estimation and decision-making process. These methods were classified as predicting peak outflow and breach development directly, modeling analytical hydraulics and erosion processes, determining breach development and resulting outflow hydrograph simultaneously with process-based models. In addition, further refining of the breach development was suggested in order to make accurate estimations that were integrated with flood routing in the analysis.

Xiong (2011) identified dam break analysis in terms of model and theory by combining case studies with mechanics. Predicting breach parameters and peak outflow were defined as important points for dam break phenomenon and estimation of potential damages. As a result of the analysis, downstream regions that were relatively close to the dam body were more affected by dam break. However, analyses showed that the changes of breach parameters had no great impact on the maximum water surface elevation which may be originated from initial and boundary conditions.

Muchard & Deo (2012) compared different methods and assumptions of dam breach analysis by using an unsteady flow model in HEC-RAS. In spite of having an ability to yield precise and accurate results for flood inundation, more detailed data may be required for unsteady models than steady models. In a similar manner, the dynamic routing method was considered to be more appropriate than a level pool method for flood inundation mapping; however, a bathymetric map of the reservoir was needed for dynamic routing. Therefore, an alternative level pool method was performed with the reservoir which was represented by a storage area. Determination of breach geometry, outflow hydrograph, and reservoir routing method were important since it was indicated that the change in these data might result in different outcomes according to the results of the analyses.

Nguyen & Weston (2013) discussed both hydrologic and hydraulic methods and assumptions for the dam break analysis. Analysis procedures were simplified since the model was created only to compare the probable outcomes of different scenarios. Therefore, only the main tributaries and storage areas were used in the model. Then, lateral structures were added by the digital terrain. A bathymetric map was provided from previous studies in HEC-RAS for the region. Additionally, cross-sections were interpolated to prevent numerical instabilities in the analysis. Evaluation of the results was performed with a GIS-based model in HEC-FIA in order to estimate flood effects. Finally, flood damages were computed by using socio-economical data, flood arrival time and the maximum depth of water values which were determined for the study area.

Derdous, Djemili, Bouchehed & Tachi (2015) used a GIS-integrated dam break model in HEC-RAS to investigate the potential risks of failure of Zardezas Dam. First of all, the digital terrain model was imported to HEC-RAS with GIS. Unsteady flow analysis for dam break was carried out in HEC-RAS. Then, maps of maximum depth of water and velocity of water were visualized by GIS environment. Finally, a flood risk map was created from generated maximum depth and velocity maps in order to examine the probable outcomes of dam break flood. Estimation of loss of life and property damages, improving flood risk management and planning of land use have become available with created risk maps. It was concluded that an integrated hydraulic model can reduce the time and effort which are required to estimate potential risks of dam break flood.

Gharbi, Soualmia, Dartus & Masbernat (2016) analysed 1D and 2D models in order to investigate the recurrent flood risk at the Medjerda basin. By taking into consideration that the floods were closely related to sediment transport, the one-dimensional model was used to determine the rate of sediment transport and examine the morphological changes in the river bed. Furthermore, the two-dimensional model was used to determine the materials which were transported by the river. Although one-dimensional simulation was preferred for being quick and easy to implement, it

was seen that the two-dimensional model provided more accurate and precise results in terms of flow changes, sediment transport rates, and morphological changes.

Haltas, Tayfur & Elci (2016) simulated a 2D model to compare the results with experimental data obtained from the physical model which was used to replicate Ürkmez Dam and its downstream region. 1D model in HEC-RAS was used to obtain the routing of flood hydrograph of the area where one-dimensional flow conditions apply. Then, the two-dimensional model in FLO-2D was used to investigate the flood inundation area. Finally, the results of the dam break analysis were shown in GIS environment. According to the data which was measured at different locations from resulting digital maps of depth and velocity, the results of the numerical and experimental model were in agreement.

Gogoş, Popovici, Savin & Armaş (2016) analysed a GIS-based dam break model of Bicaz Dam to investigate the flood inundation in the downstream region. Values of water depth, the velocity of water and travel time of flood were obtained by a numerical simulation model in HEC-RAS with digital terrain data. Analysis of flood wave characteristics with GIS was said to facilitate the determination of potentially affected areas. According to the results of the dam break simulation, emergency action plans, land use planning, and flood warning systems were prepared to prevent the probable loss of life and property. Although a real risk analysis requires detailed information, vulnerability maps were obtained with existing data by using a multicriteria analysis to perform a simplified quantitative risk analysis and determine the flood risk maps.

Şahin (2016) used a two-dimensional model in FLO-2D for Sungurlu Dam and Osmangazi Dam in order to obtain flood inundation maps for different scenarios. First of all, two digital elevation models that have different resolutions were created with the contour maps by using GIS tools. Then, Manning's roughness coefficient values were specified according to geologic features of the flood plain. In addition, area and width reduction factors were used for the effect of the buildings on the water volume.

Thus, the simulations were carried out with different mesh sizes and different digital elevation model resolutions. The results of the analyses were examined for both the flood plain and pre-determined control points. In this manner, the results were evaluated for different hydrographs and corresponding flood areas. Finally, the flood inundation maps were visualized in terms of maximum flow depth and maximum velocity.

Amini, Arya, Eghbalzadeh & Javan (2017) conducted the dam break analysis of Vahdat Dam by using Hec-GeoRAS and HEC-RAS for different failure modes. By utilizing the data which was obtained from field measurements and authorized institutions, Manning's roughness coefficient of the downstream region was estimated. Then, empirical expressions were used to determine breach characteristics in order to create a breach model in HEC-RAS. The results of the analysis of the dam break model and the empirical equations were compared according to the maximum discharge values. In this manner, it was observed that the type of failure had a significant effect on the hydraulic properties of the flood wave in the downstream region of the dam. To conclude, the methods which were used to calculate breach geometry have a significant effect on dam break analysis since different breach dimensions and breach formation times could be obtained for various conditions.

Basheer, Wayayok, Yusuf & Kamal (2017) used a dam break model of Mosul Dam in HEC-RAS in order to examine the effects of breach parameters on the flood hydrographs. It was noted that the breach geometry and the breach formation time were crucial in determining the flood hydrograph characteristics. Therefore, the analyses were performed by considering these parameters. Furthermore, different water surface elevation values at the reservoir were considered for each method with various dam break scenarios in order to cover both overtopping and piping failure modes. After completing the sensitivity analysis, it was concluded that the breach formation time had a greater effect on peak discharge values and peak discharge time than breach geometry.

Joshi & Shahapure (2017) simulated a two-dimensional dam break model of Ujjani dam in order to investigate potential risk areas for flood inundation with the help of an unsteady analysis in HEC-RAS. Prediction of breach parameters and routing of outflow hydrograph were determined as two main steps of dam break analysis. Firstly, topographic data, digital elevation model, land cover map were collected as geometric information for the terrain. Then, the storage area and two-dimensional flow area were connected in order to process the breach formation data into the HEC-RAS model. Finally, the created model was analysed and the results of the analysis were visualized as in the form of flood inundation maps. It was indicated that accurate prediction of dam break flows and evaluation of result maps are crucial points in the preparation of emergency action plans and flood disaster management.

Sharma (2017) accomplished a study of dam break analysis of Ajwa Dam by using ArcGIS and HEC-RAS in order to examine the flood inundation at the downstream area. In the study, the analyses were carried out for different modes of failure. Additionally, the outflow hydrograph was determined at different river stations by HEC-RAS. As a result of the analysis, maximum water surface elevation, velocity of water and flow rate values were determined for specific cross-sections. The inundation map was also generated for the downstream region with the help of the GIS environment. Thus, preparation of evacuation plans, construction of floodwalls, improvement or regulation for river channels and related measures for flood scenarios were recommended by means of dam break analysis.

There are numerous numerical and physical studies on dam breaking analysis. Some of the past studies, which are carried out to investigate the dam break phenomenon or used to facilitate the related applications, are also given in this context.

1.3. The Objective of the Study

The aim of this study is to investigate the process of dam break analysis with two-dimensional models by using HEC-RAS software. For this purpose, the dam break analyses of Berdan Dam were performed as a case study. Thus, flood inundation maps were obtained to examine the results of probable dam break scenarios in the study area.

1.4. Thesis Organization

This thesis is organized in five chapters. A brief introduction, literature review and purpose of the study are presented in Chapter 1. In Chapter 2, mathematical relationships which are used in hydraulic modeling and solution methods of HEC-RAS software are examined. After general information about the study area, the parameters which were used as input in the hydraulic model and the process of the two-dimensional analysis in HEC-RAS are mentioned in Chapter 3, the resulting flood inundation maps of the dam break analyses for the piping mode of failure are presented in Chapter 4. In Chapter 5, the results of the analyses which were carried out for overtopping mode of failure are represented. Finally, the conclusions of the study are given in the last chapter.

CHAPTER 2

HYDRAULIC MODEL

2.1. Hydraulic Model of HEC-RAS

In this study, the user's manual of HEC-RAS was used to follow the numerical solution procedure and the discretization of governing equations. In this section, the original symbols given in the manual were maintained.

2.1.1. Discretization of Two-Dimensional Unsteady Flow Equations

For two-dimensional unsteady flow, the continuity equation can be written by assuming the flow is incompressible;

$$\frac{\partial H}{\partial t} + \frac{\partial(hu)}{\partial x} + \frac{\partial(hv)}{\partial y} + q = 0 \quad (2.1)$$

where H is water surface elevation, t is time, h is the depth of water, q represents source/sink flux, u and v are the velocity components in x - and y -direction, respectively.

If Equation (2.1) is written in vector form:

$$\frac{\partial H}{\partial t} + \nabla \cdot hV + q = 0 \quad (2.2)$$

where $V=(u,v)$ and $\nabla = (\partial/\partial x, \partial/\partial y)$.

Equation (2.2) can be written in integral form as:

$$\frac{\partial}{\partial t} \int_{\forall} d\forall + \int_S V \cdot n dS + Q = 0 \quad (2.3)$$

where \forall is the control volume, S is the side boundary and Q is the source/sink flow term. The control volume \forall is written as a function of water surface elevation.

Then, the first term of Equation (2.3) can be discretized for time Δt as:

$$\frac{\partial}{\partial t} \int_{\forall} d\forall = \frac{\forall(H^{n+1}) - \forall(H^n)}{\Delta t} \quad (2.4)$$

The second term of the Equation (2.3) can be represented as a summation of the vertical faces:

$$\int_S V \cdot n dS = \sum_k V_k \cdot n_k A_k(H) \quad (2.5)$$

where V_k is the average velocity, n_k is unit normal vector at face k , and A_k is the face area.

2.1.2. Sub-grid Bathymetry Approach

A high-resolution map may be inappropriate to use as a grid considering the computation times of the simulations. When simulating hydraulic models, a coarser computational grid with fine topographic features can be used on high-resolution bathymetric information. In this case, the sub-grid bathymetry approach can be presented as a solution (Casulli, 2009).

By integrating the sub-grid technique, high-resolution bathymetric data can be used for calculations on relatively coarse grids which allow larger time intervals. The sub-grid data can be used with a coarser computational grid since the hydraulic data is calculated from fine bathymetry in accordance with the conservation of mass. Therefore, the sub-grid model can be used to simulate the flow on a wide terrain (Sehili, Lang, & Lippert, 2014).

An example of the computational grid with fine sub-grid bathymetry is shown in Figure 2.3.

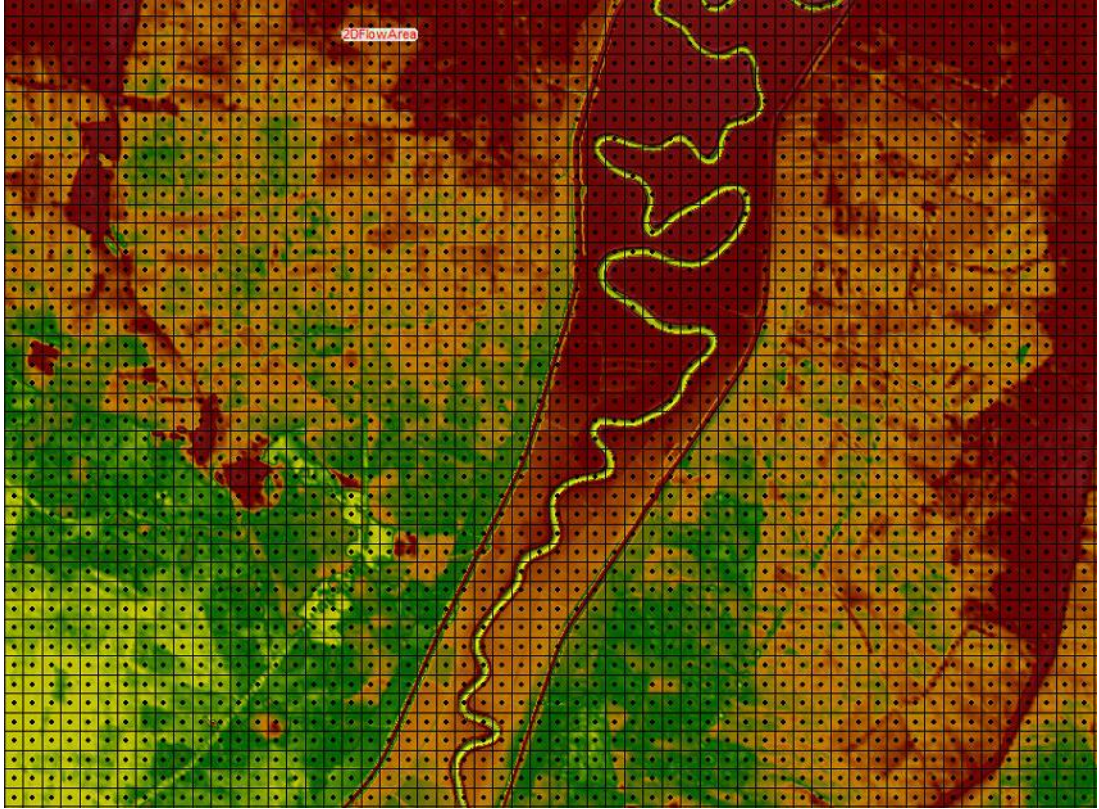


Figure 2.1. Representation of computational grid with sub-grid bathymetry data

2.1.3. Two-dimensional Shallow Water Equations

The vertical velocity component is considered to be small if the scale of horizontal length is much larger than the vertical length. In this manner, the vertical derivative terms can be neglected. The vertical momentum equation can be used with the assumption of hydrostatic pressure (Collier, Radwan, Dalcin, & Calo, 2013).

Thus, the two-dimensional shallow water equations are written as:

$$\frac{\partial u}{\partial t} + u \frac{\partial u}{\partial x} + v \frac{\partial u}{\partial y} = -g \frac{\partial H}{\partial x} + v_t \left(\frac{\partial^2 u}{\partial x^2} + \frac{\partial^2 u}{\partial y^2} \right) - c_f u + f v \quad (2.6)$$

$$\frac{\partial v}{\partial t} + u \frac{\partial v}{\partial x} + v \frac{\partial v}{\partial y} = -g \frac{\partial H}{\partial y} + v_t \left(\frac{\partial^2 v}{\partial x^2} + \frac{\partial^2 v}{\partial y^2} \right) - c_f v + f u \quad (2.7)$$

where u and v are the velocity terms in x- and y-direction, ν_t is the horizontal eddy viscosity coefficient, H is water surface elevation, g is gravitational acceleration, c_f is the bottom friction coefficient, and f is the Coriolis parameter.

If Equation (2.7) is written as a single differential vector form as;

$$\frac{\partial V}{\partial t} + V \cdot \nabla V = -g\nabla H + \nu_t \nabla^2 V - c_f V + f k \times V \quad (2.8)$$

where $\nabla = (\partial/\partial x, \partial/\partial y)$ and k is the unit vector in the vertical direction.

A simplified equation which is in the form of conservation of mass and momentum can be expressed by neglecting the diffusive effects due to viscosity, turbulence and the Coriolis term (Vreugdenhil, 1994).

Therefore, the momentum equation can be further simplified as:

$$\frac{n^2 |V| V}{(R(H))^{4/3}} = -\nabla H \quad (2.9)$$

By dividing both sides of the equation by the absolute value of their square roots, Equation (2.9) can be written as:

$$V = \frac{-(R(H))^{2/3}}{n} \frac{\nabla H}{|\nabla H|^{1/2}} \quad (2.10)$$

where V is the velocity vector, R is the hydraulic radius, ∇H is the gradient of water surface elevation and n is Manning's roughness coefficient.

2.1.4. Diffusion Wave Approximation

The two-dimensional form of diffusion wave approximation is obtained from the momentum equation by neglecting inertial terms in the horizontal momentum equation and substituting the bottom slope in Manning's formula. Then, the differential form of diffusive wave approximation of shallow water equations can be written by integrating into the conservation of mass (Alonso, Santillana, & Dawson, 2008).

$$\frac{\partial H}{\partial t} - \nabla \cdot \beta \nabla H + q = 0 \quad (2.11)$$

$$\text{where } \beta = \frac{(R(H))^{5/3}}{n|\nabla H|^{1/2}}$$

By substituting into the sub-grid bathymetry:

$$\frac{\forall(H^{n+1}) - \forall(H^n)}{\Delta t} - \sum_k \alpha \nabla H \cdot n + Q = 0 \quad (2.12)$$

$$\text{where } \alpha = \alpha(H) = \frac{(R(H))^{2/3} A_k(H)}{n|\nabla H|^{1/2}}$$

$A_k(H)$ is the area of face k and $\forall(H^n)$ is the cell volume at time n .

2.2. Application of Numerical Methods

2.2.1. Finite Difference Approximation

A finite difference approximation can be introduced by using a derivative of the difference of two quantities in consecutive time steps according to the definition of first order derivative in time (Hirsch, 2007).

Therefore, the derivative of the water volume in time is discretized with the difference of the volumes which are represented by functions of water surface elevation as:

$$\frac{\partial \forall}{\partial t} \approx \frac{\forall(H^{n+1}) - \forall(H^n)}{\Delta t} \quad (2.13)$$

Then, the directional derivative is written in the direction n' as:

$$\nabla H \cdot n' = \frac{\partial H}{\partial n'} \approx \frac{H_2 - H_1}{\Delta n'} \quad (2.14)$$

$\Delta n'$ is the distance between the centers of two adjacent cells.

2.2.2. Finite Volume Approximation

The finite volume technique is generally used for the conservation of mass and momentum. Therefore, this approach can be utilized for complex mesh systems. For discretization, the cells are considered as the control volumes. Therefore, the mean value of a variable in a control volume is termed as the cell-centered or the cell value. Likewise, the mean value on the faces is calculated as cell center value. In brief, it can be stated that the finite volume method produces cell center values (Mazumder, 2016).

Gauss' divergence theorem is applied to dual cells by approximating the average value of ∇H at a grid face as:

$$\nabla H \approx \frac{\oint_L H n dL}{A'} \quad (2.15)$$

Where L is the boundary of the dual cells and A' is the area of the dual cells shaded in Figure 2.4.

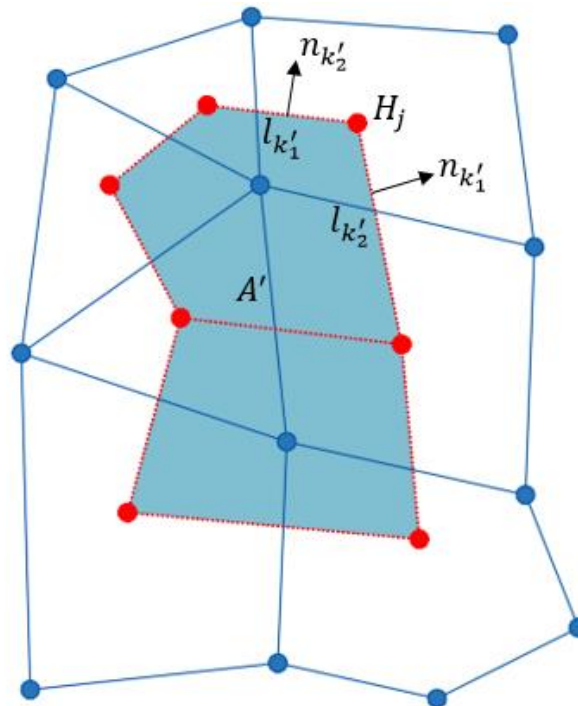


Figure 2.2. Representation of dual grid cell

It is possible to express the integral form as a sum over the faces of dual cells for polygonal the dual cells. By rearranging the terms by cell index j , the finite volume approximation of ∇H can be written as:

$$\nabla H \approx \sum_j c_j H_j \quad (2.16)$$

where

$$c_j = \frac{n_{k'_1} l_{k'_1} + n_{k'_2} l_{k'_2}}{2A'} \quad (2.17)$$

Then, the derivatives in a direction T' can be approximated as:

$$\frac{\partial H}{\partial T'} = \nabla H \cdot T' \approx \sum_j c'_j H_j \quad (2.18)$$

where

$$c'_j = (n_{k'_1} l_{k'_1} + n_{k'_2} l_{k'_2}) \cdot \frac{T'}{2A'} \quad (2.19)$$

2.2.3. Hybrid Discretization

The normal derivative is expressed as the sum of a finite difference and a finite volume approximation as a hybrid discretization for the non-orthogonal grid (Norris, 2000).

If k is the vertical unit vector and n is the direction which is normal to the cell face, $T = k \times n$ is orthogonal to n . In the same manner, if the direction of n' is specified by the face between the cells, $T' = k \times n'$ is said to be orthogonal to n' .

Then, the normal derivative can be written by using finite difference and finite volume approximation as;

$$\frac{\partial H}{\partial n} = (n \cdot n') \frac{\partial H}{\partial n'} + (n \cdot T') \frac{\partial H}{\partial T'} \quad (2.20)$$

By expressing in a summation form, Equation (2.20) becomes:

$$\nabla H \cdot n = \frac{\partial H}{\partial n} \approx \sum_j c'_j H_j \quad (2.21)$$

where c'_j represents the finite difference and finite volume terms.

2.2.4. Discrete Scheme of Numerical Solver

The combination of finite difference and finite volume approximation can be discretized by a weighting factor θ in order to take into account the distribution of these approximations (Versteeg & Malalasekera, 1995).

Then, a generalized form of Crank-Nicolson method can be introduced to solve shallow water equations in finite difference form as:

$$\nabla(H^{n+1}) + \sum_j a_j \left((1 - \theta)H_j^n + H_j^{n+1} \right) = \nabla(H^n) - \Delta t Q \quad (2.22)$$

By rearranging the terms:

$$\nabla(H^{n+1}) + \theta \sum_j a_j H_j^{n+1} = [\nabla(H^n) - \Delta t Q] - (1 - \theta) \sum_j a_j H_j^n \quad (2.23)$$

Equation (2.23) can be expressed in vector form as:

$$\nabla(H) + \Psi H = b \quad (2.24)$$

where ∇ is the vector of cell volumes and Ψ is the vector of water surface elevations.

Considering the bathymetric relationships of volume and derivative of volume with respect to H, an iterative formula is introduced as;

$$H^{m+1} = H^m - (P(H^m) + \Psi)^{-1} (\nabla(H^m) + \Psi H^m - b) \quad (2.25)$$

where m represents the iteration step.

For shallow water equations, continuity equation can be discretized with the Crank-Nicolson method by using finite volume approximation as:

$$\frac{\Omega(H^{n+1}) - \Omega(H^n)}{\Delta t} + \sum_k \pm A_k(H) ((1 - \theta)(U_N)_k^n + \theta(U_N)_k^{n+1}) + Q = 0 \quad (2.26)$$

Where the sign of the summation is dependent on the orientation of cell face k .

In HEC-RAS, velocity values are computed on the grid faces in this scheme. Therefore, momentum equations cannot be located on the cells. However, the velocity gradients can be computed by using Gauss' Divergence Theorem since the velocities at the nodes are known from the previous time step.

$$\nabla V \approx \sum_i c'_i V_i^n \quad (2.27)$$

For dual cells, a double summation form can be written for the cells around a node as:

$$\nabla^2 V \approx \sum_j d'_j \nabla V_j \approx \sum_j d'_j \sum_i c'_i V_i^n \quad (2.28)$$

Where c'_i and d'_j are vector coefficients.

In addition, velocity is obtained from the discretization of equations that contain only acceleration and Coriolis terms. A vector equation is defined in terms of velocities and water surface elevations at a location X as:

$$\begin{pmatrix} 1 & -\theta \Delta t f \\ \theta \Delta t f & 1 \end{pmatrix} \begin{pmatrix} u_*^{n+1} \\ v_*^{n+1} \end{pmatrix} = \begin{pmatrix} u_X^n + (1 - \theta) \Delta t f v_X^n \\ v_X^n + (1 - \theta) \Delta t f u_X^n \end{pmatrix} \quad (2.29)$$

Where f is the Coriolis parameter, u and v are the velocities.

Further, discretization can be written in the shape of an explicit formulation as:

$$V_*^{n+1} = \begin{pmatrix} u_*^{n+1} \\ v_*^{n+1} \end{pmatrix} = \begin{pmatrix} 1 & -\theta \Delta t f \\ \theta \Delta t f & 1 \end{pmatrix}^{-1} \begin{pmatrix} u_X^n + (1 - \theta) \Delta t f v_X^n \\ v_X^n + (1 - \theta) \Delta t f u_X^n \end{pmatrix} \quad (2.30)$$

2.3. Solution Algorithm of HEC-RAS

2.3.1. Calculation of Water Surface Elevation

Two-dimensional analysis in HEC-RAS is firstly started with the initial trial when computing the water surface elevation value in storage areas and two-dimensional flow areas. All computational cells and storage areas are controlled to determine whether the difference of the water surface elevation values at consecutive time steps is less than the predefined or computed tolerance. If the difference between the two steps is less than the numerical solution tolerance, the solver continues with the next time step. However, if it is greater than the tolerance, the time step is recomputed with a new estimation. In the same manner, if a solution emerges where the numerical error is less than the tolerance in all locations, it uses the iteration as the correct answer and saves it as the best solution and proceeds to the next time step (Brunner, 2016b).

2.3.2. Complete Solution Procedure

1. The geometry and sub-grid bathymetry data are pre-computed.
2. Solver starts the computational process with initial conditions at time step $n=0$
3. Boundary conditions are obtained for the next time step $n+1$.
4. Solver makes an initial guess for velocities and water surface elevations.
5. The θ -averaged water surface elevations, i.e, $H = (1 - \theta)H_j^n + \theta H_j^{n+1}$ and hydraulic properties of sub-grid bathymetry are computed.
6. The system of equations is solved iteratively to compute H^{n+1} .
7. Velocity values U_N^{n+1} are computed.
8. If the computed error is greater than the tolerance, the solver goes to step 5. If the error is smaller than the tolerance, it proceeds to the next step.
9. Solver continues to iterate until the last time step is reached and all computed values are accepted. If there are more time steps, the solver goes back to step 3, otherwise, unsteady flow simulation ends (Brunner, 2016b).

The complete solution algorithm of HEC-RAS is shown in Figure 2.5.

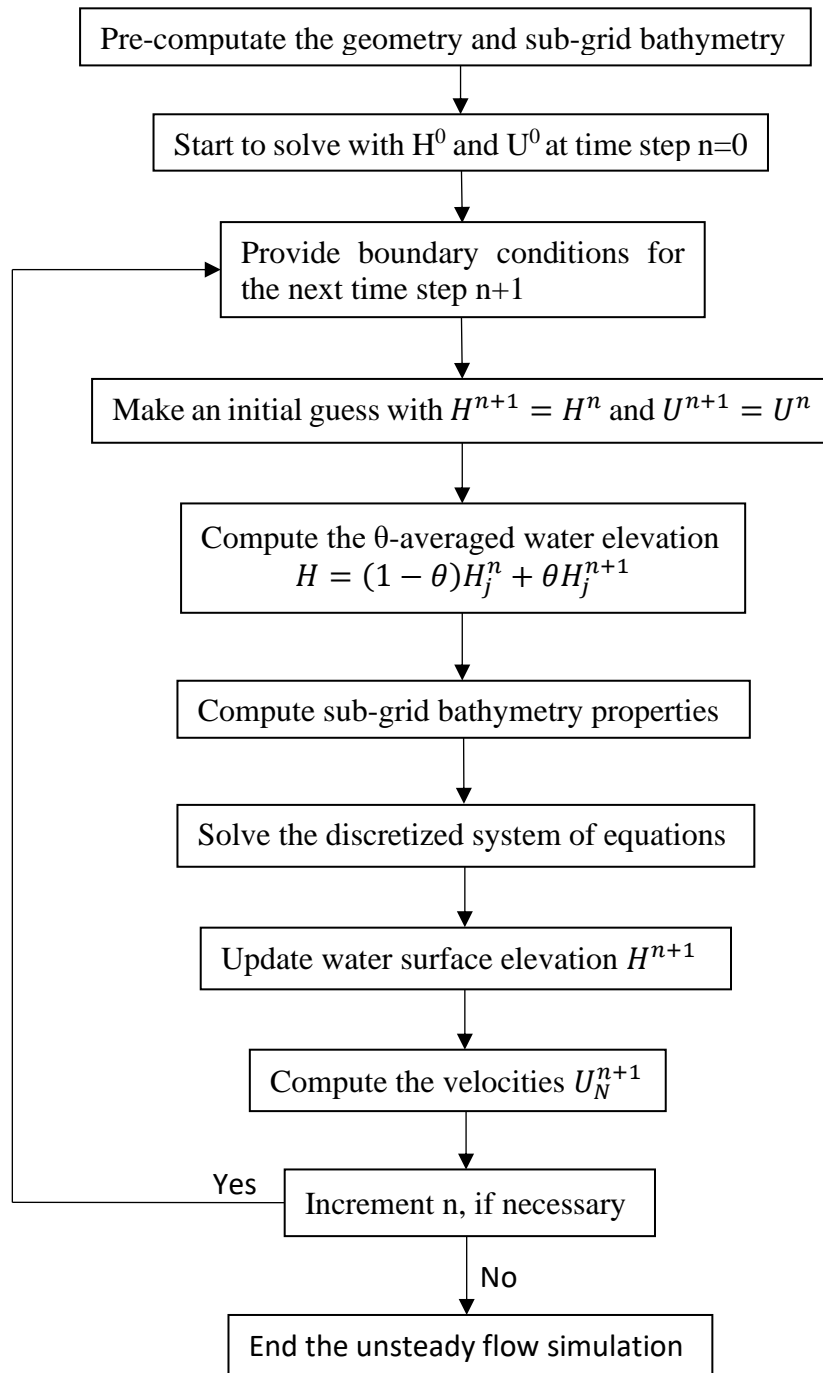


Figure 2.3. Solution algorithm of HEC-RAS

CHAPTER 3

TWO-DIMENSIONAL DAM BREAK MODEL OF BERDAN DAM

3.1. The Study Area

3.1.1. General Characteristics of the Study Area

The study area is located in the sub-basin of the Berdan River which is in the East Mediterranean Basin. The location of the study area is shown in Figure 3.1. The Berdan Dam is within the borders of Tarsus district of Mersin. The water which flows from the Berdan Dam merges with tributaries and then flows into the Mediterranean Sea from the Berdan River.

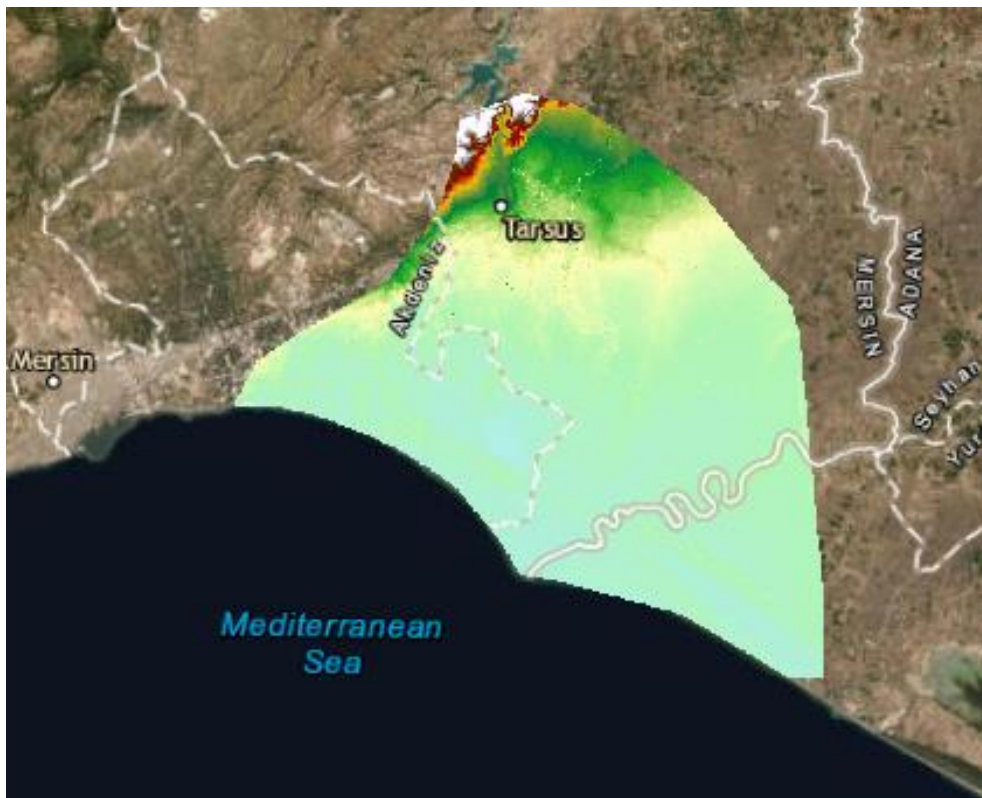


Figure 3.1. Location of the study area

The population of Tarsus district in Mersin is 339.676 for 2018, according to data which was obtained from TÜİK (“Türkiye İstatistik Kurumu,” 2018).

Berdan Dam and Tarsus settlement are shown in Figure 3.2.

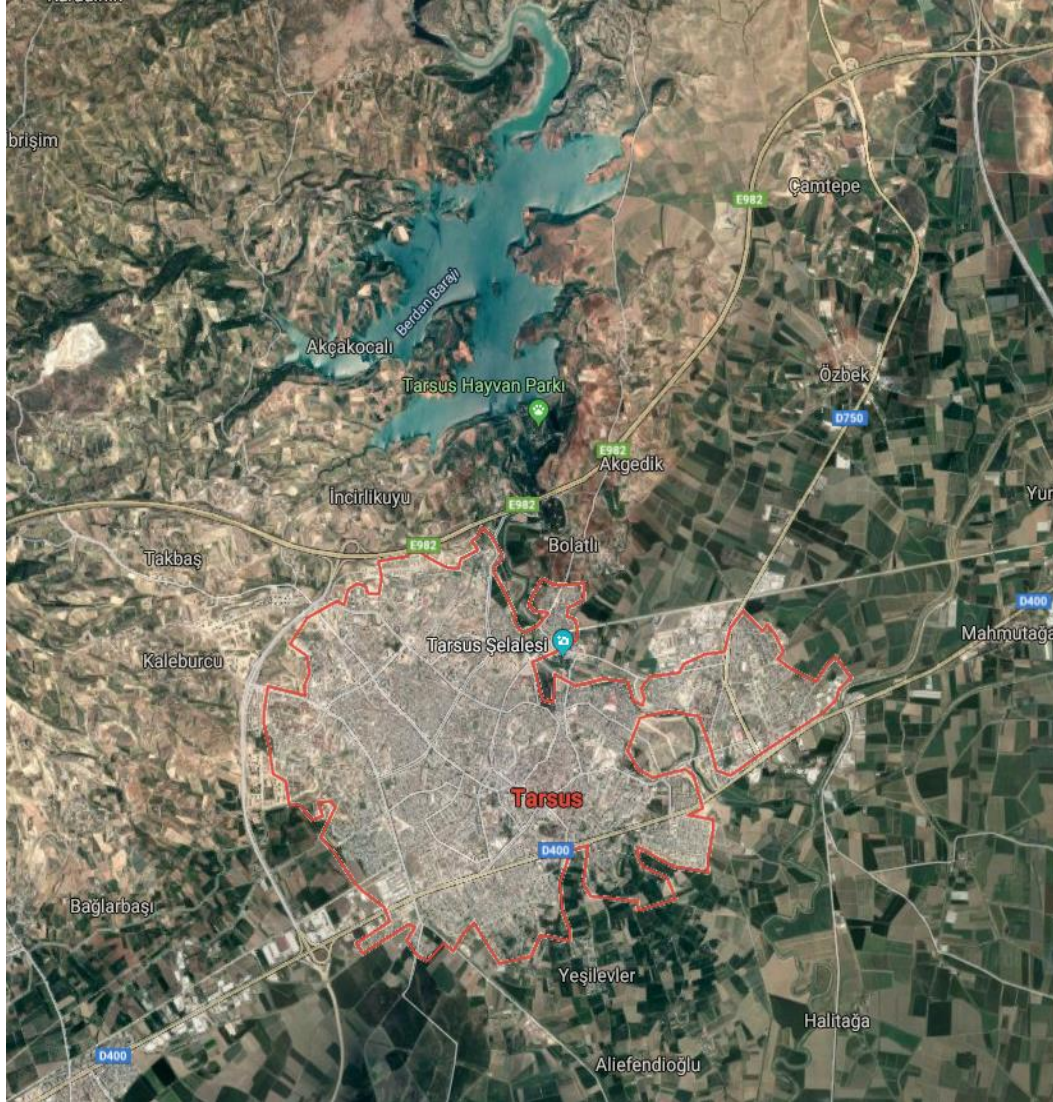


Figure 3.2. Tarsus district and Berdan Dam

The average distance from Berdan Dam to the settlement area is 5000 m. Furthermore, the nearest distance from the dam body to the settlement area is approximately 2500 m. The locations of the settlement area and Berdan Dam are shown in Figure 3.3.

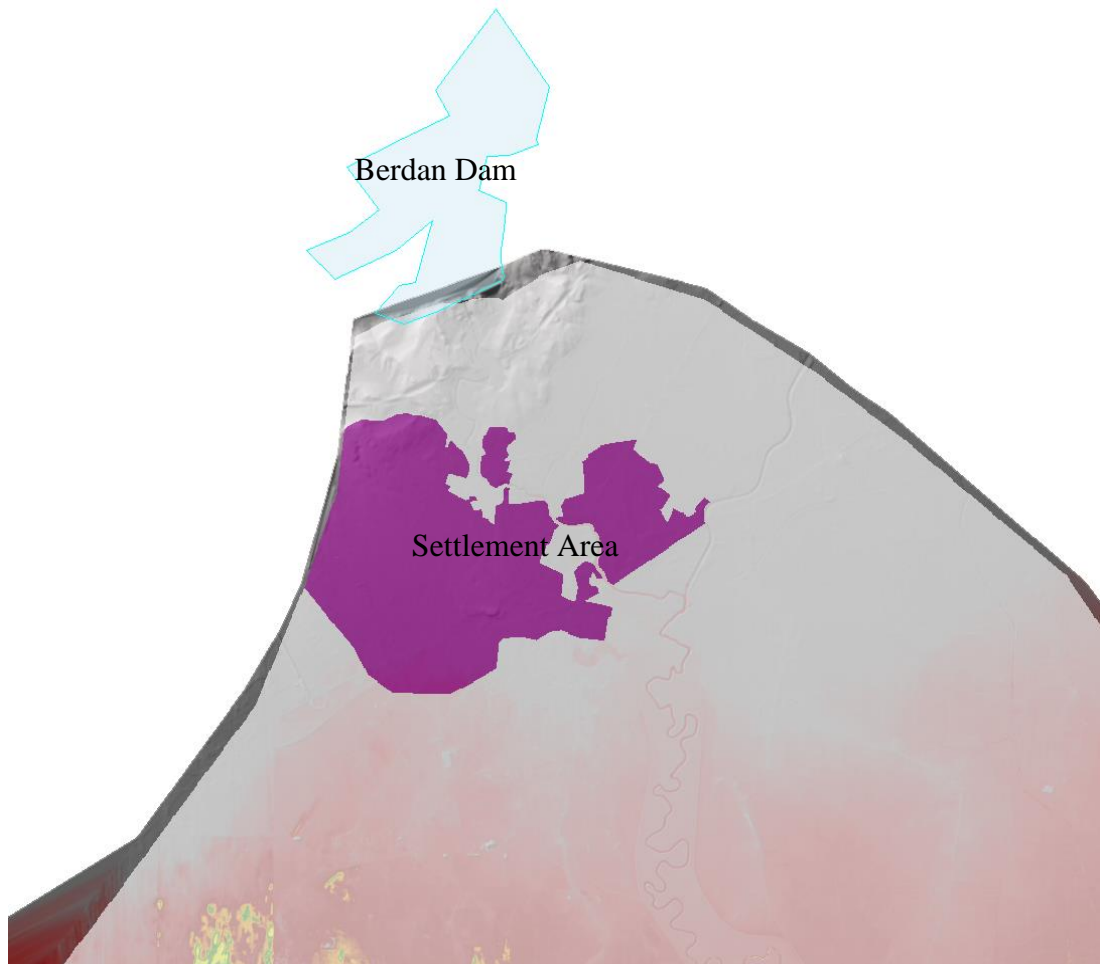


Figure 3.3. Settlement Area

The study area represents the general features of the East Mediterranean Basin. The climate of Tarsus is the typical Mediterranean climate with hot dry summers and mild-rainy winters. On the Southern border of Tarsus, there are Taurus Mountains which extend in the East-West direction.

The average annual temperature in Mersin is 18.9 °C, the hottest month is August and the coldest month is January. There are varying amounts of rainfall depending on the altitude of the foothills and plateaus of Taurus Mountains. According to Tarsus meteorological station data which was obtained from The General Directorate of State Hydraulic Works (DSİ) 6. Regional Directorate, the average rainfall in region (according to 57-year observations) is 628.6 mm.

3.1.2. Dam Characteristics

Berdan Dam, which was operationalized in 1984, was constructed for water supply, energy, irrigation, and flood control purposes. The technical specifications of Berdan Dam were introduced into the dam break model with the parameters that are used in unsteady flow analysis as in Table 3.1 and Table 3.2.

Table 3.1. Characteristics of dam body

| | |
|------------------------|---------------------------------|
| Type | Zoned earthfill |
| Embankment Volume | 2 160 000 m ³ |
| Crest Elevation | 71.60 m |
| Crest Length | 540.00 m |
| Crest Width | 10.00 m |
| Thalweg Elevation | 30.00 m |
| Height from Thalweg | 41.60 m |
| Height from Foundation | 66.60 m |
| Geological Formation | Claystone, sandstone, limestone |

Table 3.2. Characteristics of Berdan reservoir

| | |
|---|---|
| Maximum Water Level | 68.95 m |
| Normal Water Level | 56.00 m |
| Minimum Water Level | 41.80 m (Irrigation) - 44.00 m (Energy) |
| Flood control maximum water level | 67.41 m |
| Flood control minimum water level | 56.00 m |
| Reservoir volume at the maximum water level | 199.81 hm ³ |
| Reservoir volume at normal water level | 91.40 hm ³ |
| Reservoir volume at the minimum water level | 20.29 hm ³ (Irrigation) - 29.16 hm ³ (Energy) |
| Reservoir volume at flood control maximum water level | 185.52 hm ³ |
| Reservoir volume at flood control minimum water level | 91.40 hm ³ |
| Reservoir area at maximum water level | 10.75 km ² |
| Reservoir area at normal water level | 6.55 km ² |
| Reservoir area at minimum water level | 3.24 km ² (Irrigation) - 3.78 km ² (Energy) |

3.2. Two-Dimensional Dam Break Model in HEC-RAS

The two-dimensional dam break model of Berdan Dam was created with HEC-RAS and ArcGIS. The digital elevation model was integrated into geometric data for the 2D flow area. In addition, a reservoir outflow hydrograph was used to determine the flood wave which is caused by the dam break. For dam break analysis, the probable maximum flood was taken into consideration to investigate the inundation boundary under the catastrophic conditions. Moreover, Manning's roughness coefficient values of the different areas were defined on the digital map. Finally, dam breach parameters were introduced to the dam break model.

3.2.1. Integration of Geometric Data

The digital terrain of the study area was prepared by combining photogrammetric maps and measurements which were taken from the channel cross-sections. The aerial photographs were taken for the specified flood inundation boundary in order to create 1/1000 scale maps. Then, the terrain map, which was obtained from field studies and compiled from 1/1000 scale maps, was digitalized in the GIS environment. Finally, the digital elevation model was created in WGS 1984 UTM Zone 36 N with 1 m linear unit and 5 m grid size as in Figure 3.4.

Then, Digital Elevation Model (DEM) was converted to Triangulated Irregular Network (TIN) map in the GIS environment so that geometric information of terrain can be converted to a grid system in HEC-RAS. The TIN map of the study area is shown in Figure 3.5.

The TIN map was then imported to HEC-RAS so that it can be used as a GIS-based geometric data for 2D unsteady flow analysis.

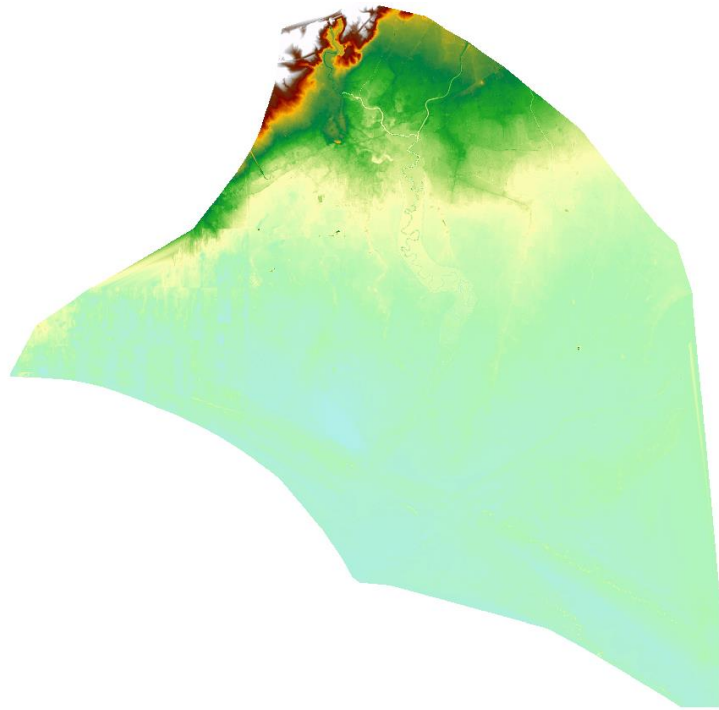


Figure 3.4. Digital Elevation Model (DEM)

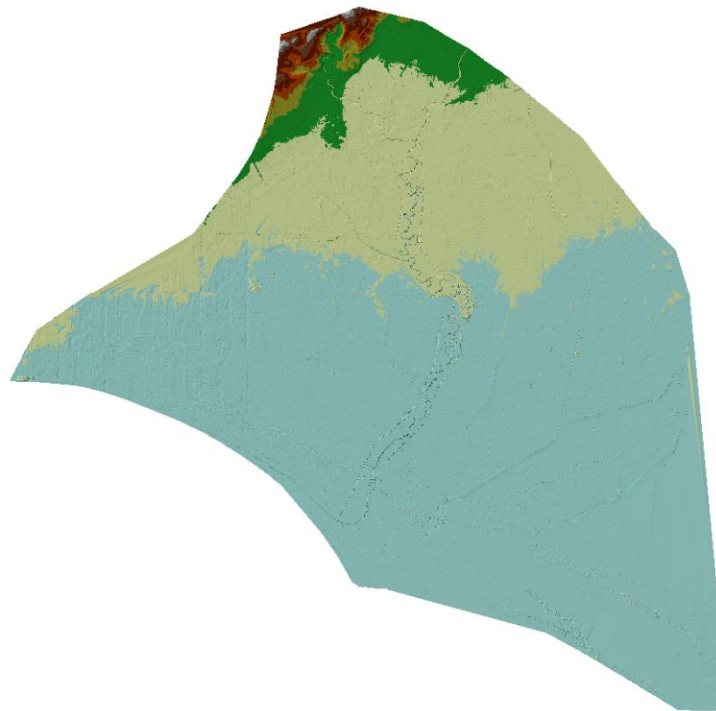


Figure 3.5. Triangulated Irregular Network (TIN)

3.2.2. Determination of Reservoir Storage Area and 2D Flow Area

The reservoir of the dam and 2D flow area were determined in order to integrate the model inputs which require to be processed so that a grid system can be created accordingly.

First of all, the reservoir and 2D flow area were created in HEC-RAS as in Figure 3.6.



Figure 3.6. Reservoir and 2D flow area

The elevation-area-volume relationship was introduced to define the characteristics of the storage area of Berdan Dam as in Figure 3.7.

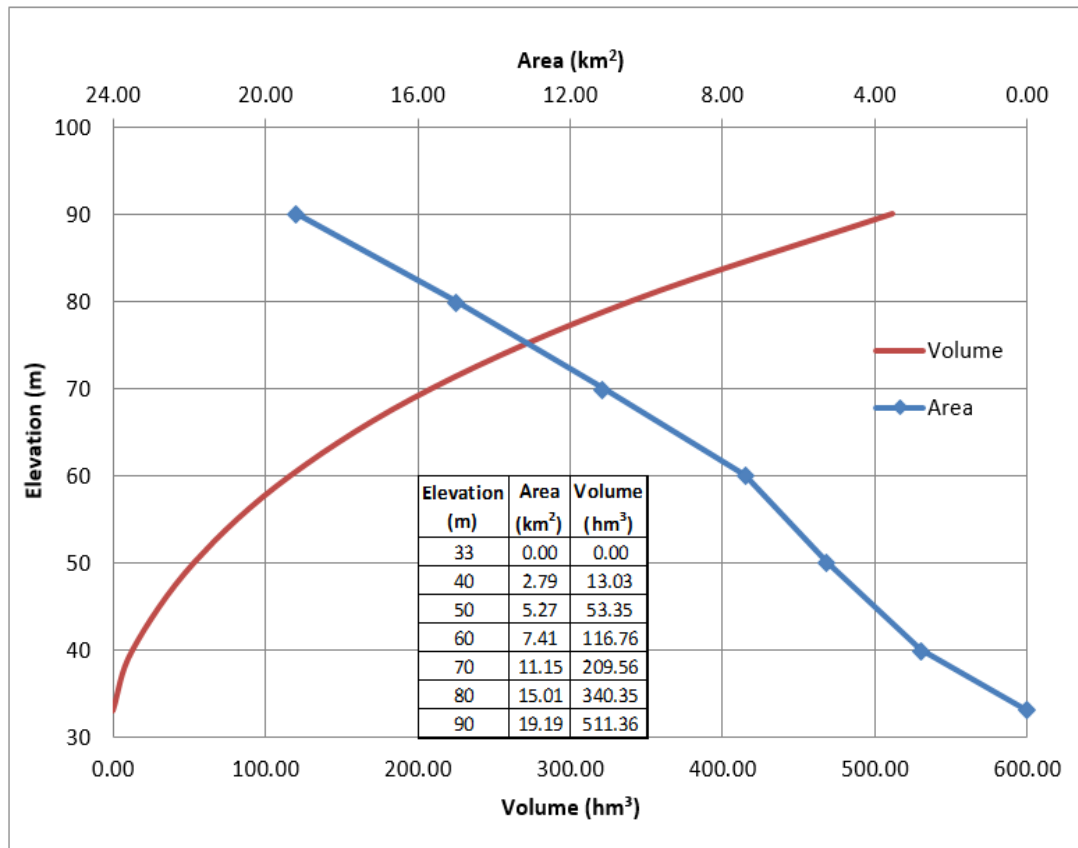


Figure 3.7. The elevation-area-volume relationship of the reservoir of Berdan Dam

The elevation-volume curve of the storage area was defined in HEC-RAS as in Figure 3.8 and Figure 3.9.

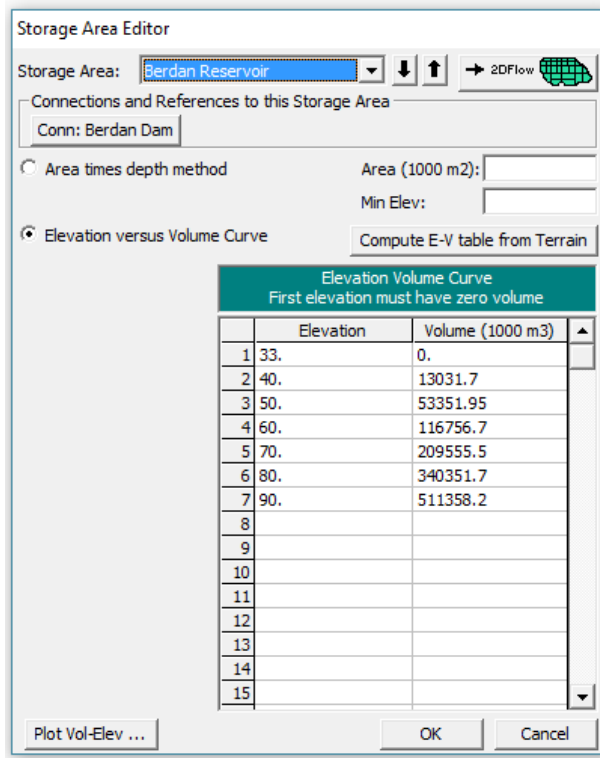


Figure 3.8. Integration of elevation-volume relationship into the model

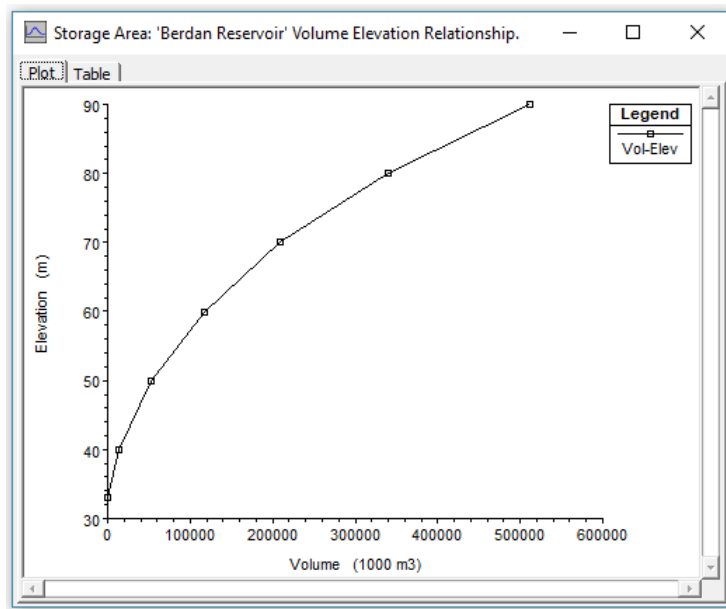


Figure 3.9. Volume - elevation curve of Berdan reservoir

3.2.3. Manning's Roughness Coefficient of 2D Flow Area

It is obvious that the roughness coefficient varies depending on such factors as the grain size distribution of bed material, geometric properties of riverbeds and floodplain areas, the amount of vegetation cover and change of flow rate. Hence, it is a crucial parameter to determine since it directly affects the water which spreads over the terrain and resulting flow conditions (Barnes, 1967; Chow, 1959).

Therefore, the land use map was classified in the GIS environment to identify the differences of the sub-regions as in Figure 3.10. Then, a land cover map was imported to HEC-RAS by taking into consideration Manning's roughness coefficient values as in Figure 3.11.

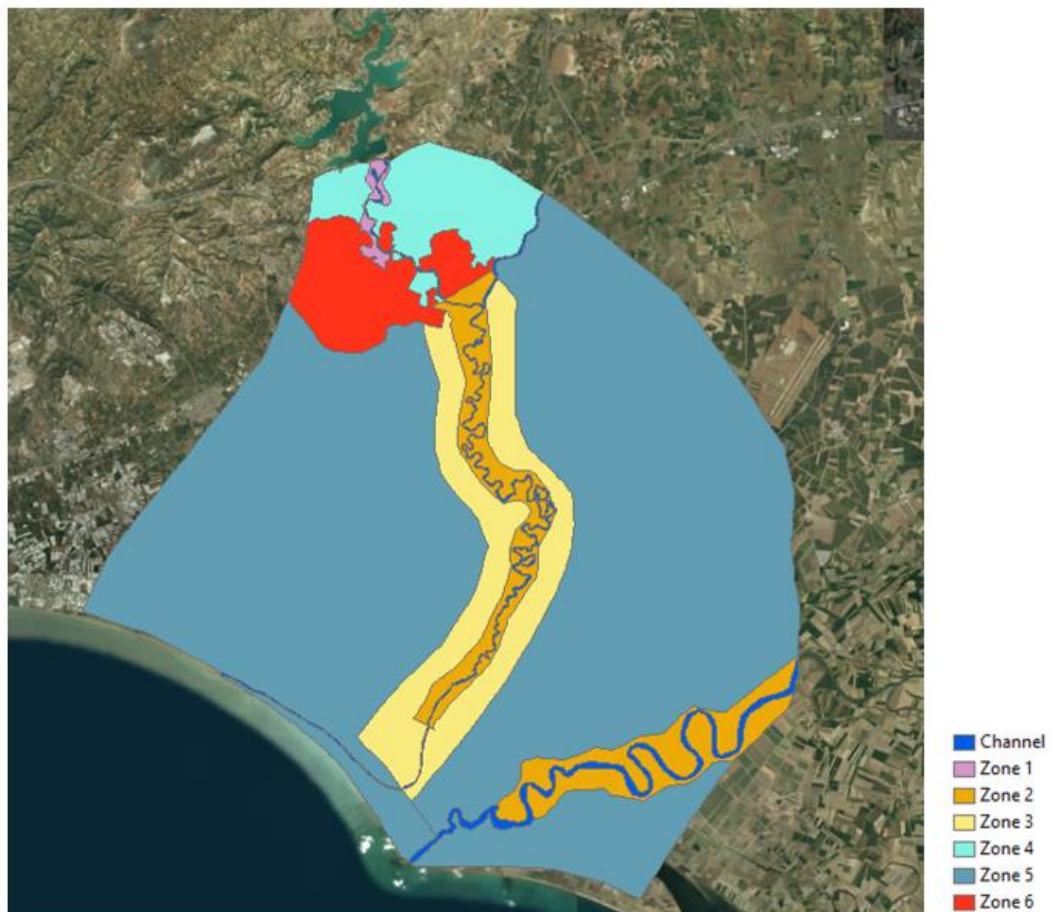


Figure 3.10. Sub-regions for different Manning's roughness coefficient in ArcGIS

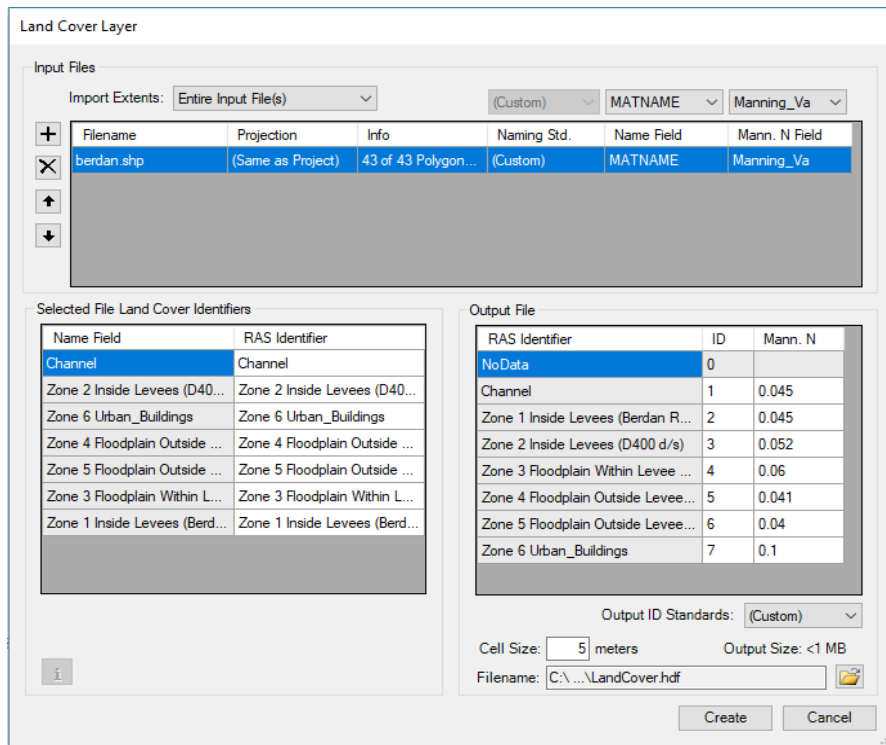


Figure 3.11. Classification of sub-regions in RAS-Mapper

The Manning's roughness values were determined from Chow (1959) and USGS tables which were compiled from the research conducted by Barnes (1967) for the classified zones as in Table 3.3.

Table 3.3. Sub-regions and corresponding roughness coefficient values

| Area | Description of Area | Manning's Roughness Coefficient |
|------|---|---------------------------------|
| 1 | Inside levees (between Berdan Dam and highway D400) | 0.045 |
| 2 | Inside levees (between the Mediterranean Sea and highway D400) | 0.052 |
| 3 | Floodplain within levee vicinity | 0.060 |
| 4 | Outside levee vicinity (between Berdan Dam and highway D400) | 0.041 |
| 5 | Outside levee vicinity (between the Mediterranean Sea and highway D400) | 0.040 |
| 6 | Residential Area | 0.010 |

As a result, the 2D flow area was studied in six sub-regions as shown in Figure 3.12.

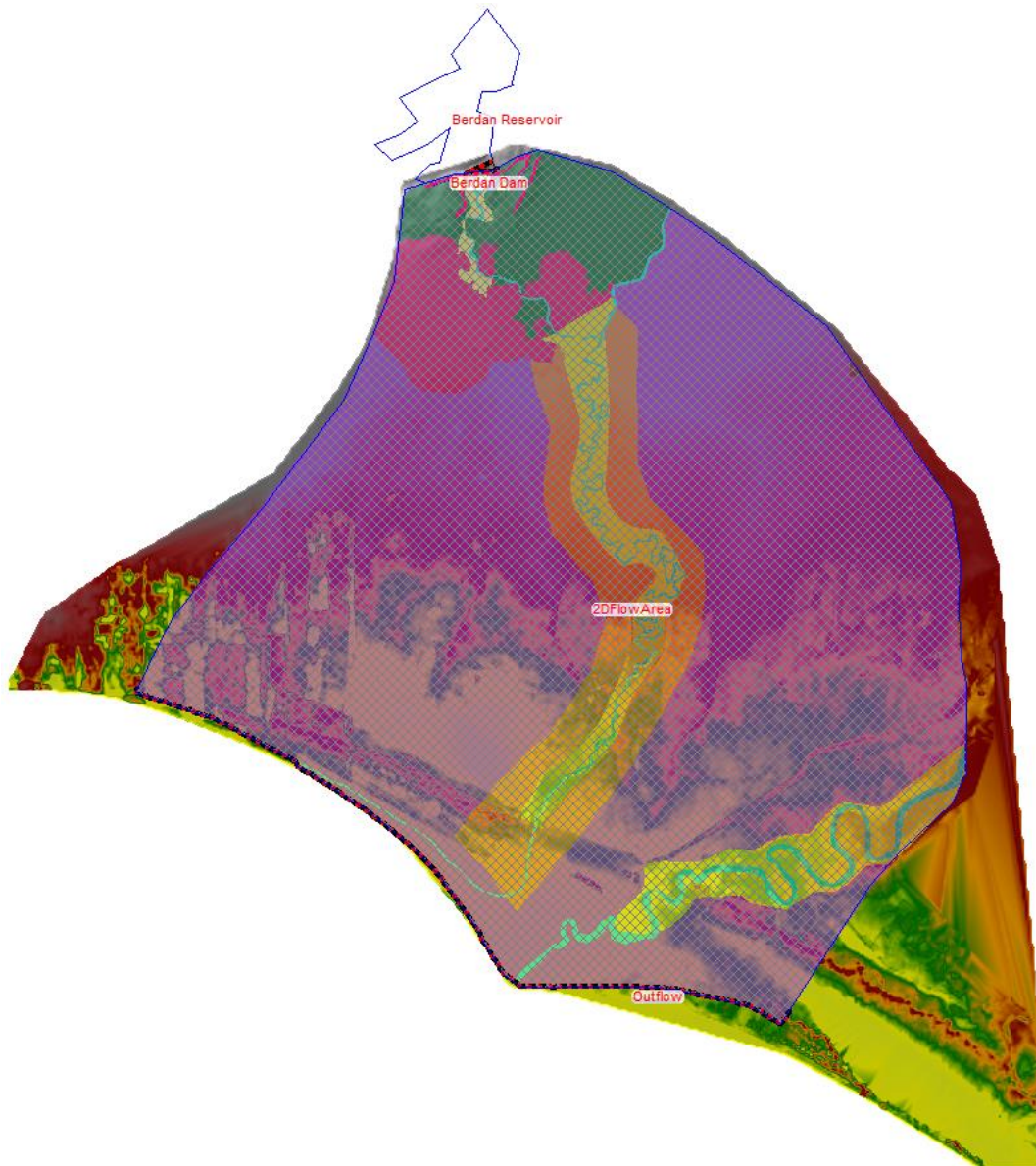


Figure 3.12. Sub-regions of the 2D flow area

However, evaluating the analysis for 0.060 as Manning's roughness coefficient value in the 2D flow area was also found useful to be able to investigate hydraulic conditions that may occur both in the river channel and flood inundation area during a catastrophic flood.

For this case study, the values which were read from tables, 20% interval of these data, and 0.060 were used in order to examine the effect of different Manning's roughness coefficient values on dam break analyses. The base Manning's roughness values of the 2D flow area and 20% interval of these values are shown in Table 3.4.

Table 3.4. Manning's roughness coefficient values used in analyses

| Area | 0.80 of Base Manning Roughness Coefficient (0.80*base n) | Manning's Roughness Coefficient of the Terrain (base n) | 1.20 of Base Manning Roughness Coefficient (1.20*base n) |
|------|---|--|---|
| 1 | 0.036 | 0.045 | 0.054 |
| 2 | 0.042 | 0.052 | 0.062 |
| 3 | 0.048 | 0.060 | 0.072 |
| 4 | 0.033 | 0.041 | 0.049 |
| 5 | 0.032 | 0.040 | 0.048 |
| 6 | 0.008 | 0.010 | 0.012 |

3.2.4. Determination of Mesh Size and Computational Time Interval

In the analyses, the mesh size of the 2D flow area can be selected as low as DEM file resolution, but this may cause some stability problems and extends the time of the analysis. In HEC-RAS, after the mesh size has been decided, the computational time interval is determined by Courant condition as:

$$C_r = V_w \frac{\Delta t}{\Delta x} \leq 1.0 \quad \text{for full momentum}$$

$$C_r = V_w \frac{\Delta t}{\Delta x} \leq 2.0 \quad \text{for diffusion wave}$$

where C_r is Courant Number, V_w is flood wave speed, Δx is the grid size, and Δt is the computational time step.

In this case study, the analyses were performed with the diffusion wave method. Therefore, the grid size and computational time step should be decided according to the condition that C_r is less than 2.0.

However, the analysis which is performed with the diffusion wave method may require C_r less than 1.0 in order to maintain stability and accuracy in rapidly varied flow. For flood inundation, 100 m grids are generally said to be sufficient considering the relatively flat and wide floodplains (Brunner, 2016a).

Grid sizes less than 100 meters required more detailed geometric information of the connection line representing the dam body in HEC-RAS for this case study. In addition, as the grid size becomes smaller, the computational time interval must be reduced according to the Courant condition. However, smaller computational time intervals increase the run time of the simulation and may cause stability problems. Therefore, the analyses were performed with different mesh sizes as 100 m, 150 m, 200 m, and 250 m in order to investigate the mesh dependency. It was determined that there is no significant difference in water surface elevation values at the cross-section which is 3500 m away from the dam. Moreover, a linear relationship could not be established between mesh size and water surface elevation according to the analyses

performed with different mesh sizes. Thus, it can be said that the results are independent of the mesh size.

Water surface elevations for mesh sizes 100 m and 200 m were found to be more reasonable when compared to other mesh sizes as shown in Figure 3.13. However, smaller mesh sizes should be used considering the sudden changes that may occur due to dam break. Therefore, it was found appropriate to use a mesh size of 100 m for this case study considering all these conditions.

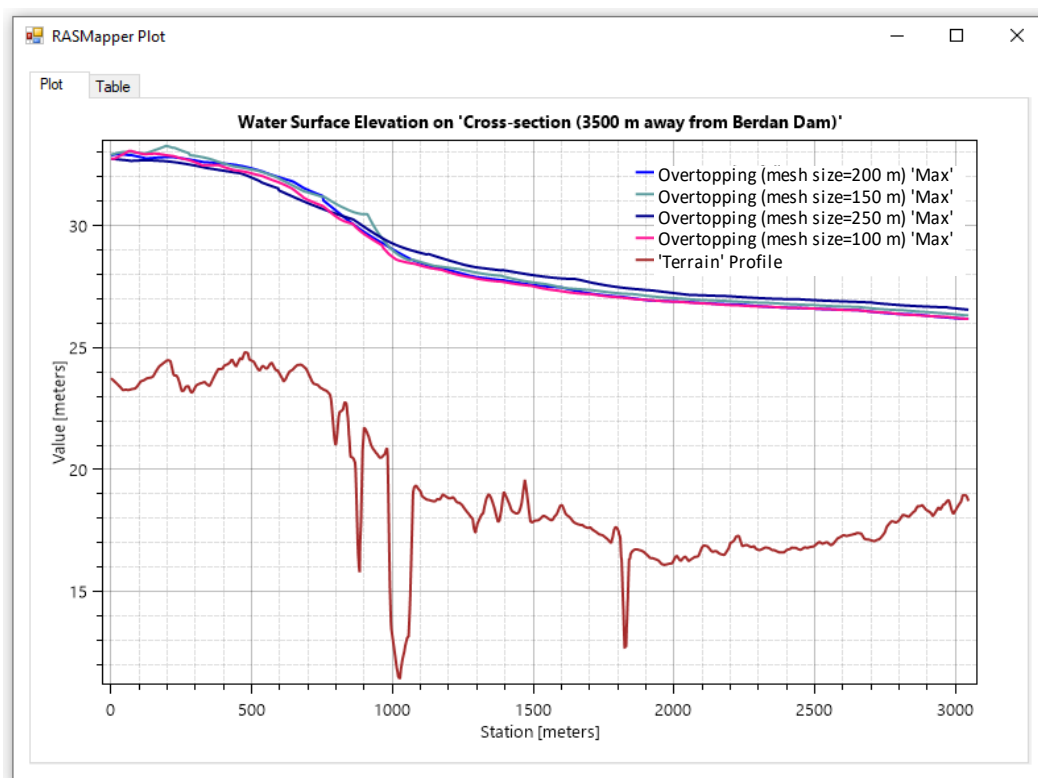


Figure 3.13. Water surface elevation values for different mesh sizes

In HEC-RAS, break lines should be added to generated mesh to control the flow direction and to consider the barriers such as mountains, highways, levees, hydraulic structures since break lines ensure that flow cannot pass through cell face until the water surface elevation is higher than the terrain elevation (Brunner, 2016a).

By taking into account the above-mentioned criteria, 100*100 m grid system was improved by using break lines and extra grid cells in the vicinity of the dam in which sudden flow changes occur. The mesh of 2D flow area generated with 47265 cells and mesh refinement are shown in Figure 3.14 and Figure 3.15, respectively.

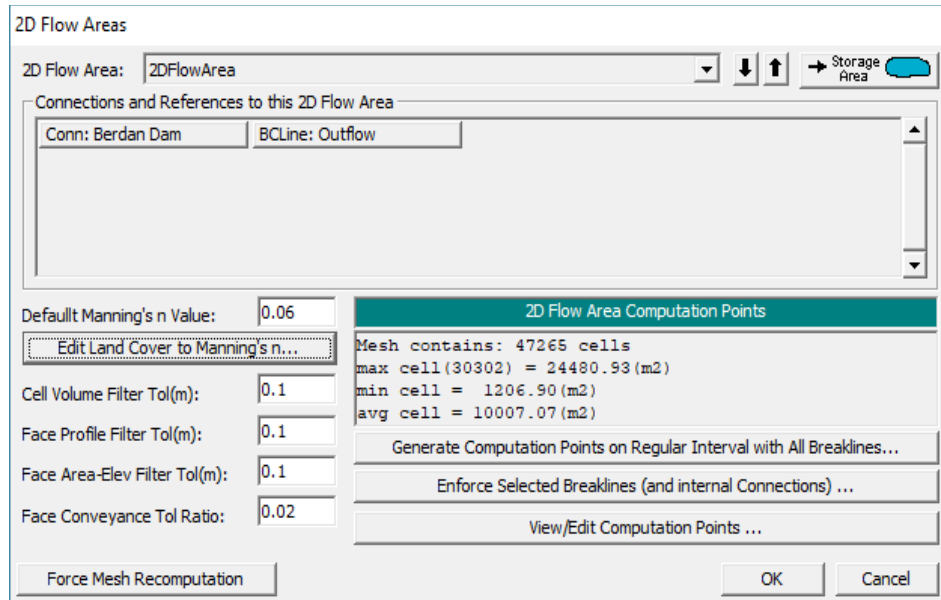


Figure 3.14. Mesh generation for 2D flow area

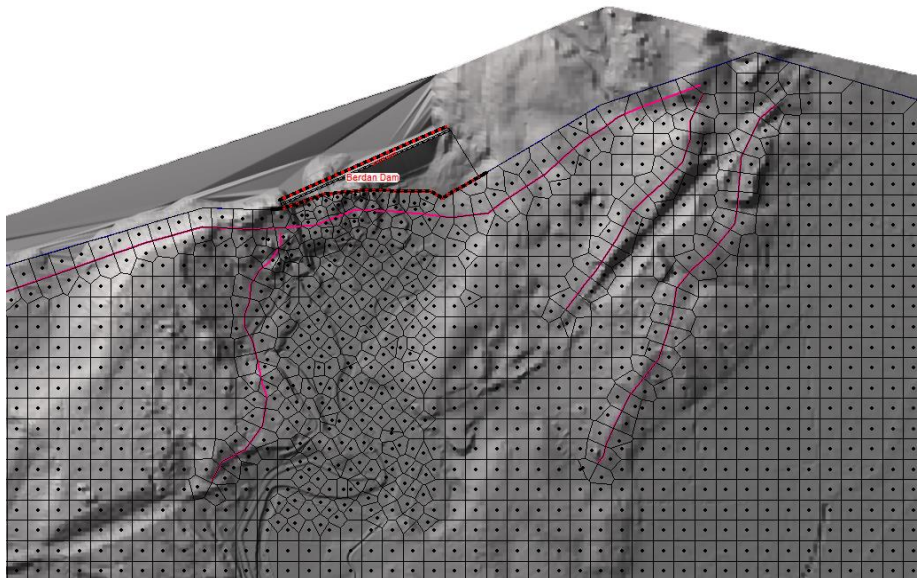


Figure 3.15. Mesh refinement in the vicinity of Berdan Dam

For dam break studies, it is generally appropriate to select the computational time step between 1 and 60 seconds. Besides, computational time steps greater than 1 second is not preferable considering the precision and accuracy of the results. For computational time step less than 1 second, the models may have some stability problems since smaller time steps may cause the leading edge of the flow wave to become steeper. Moreover, the run time of the simulation may increase dramatically (Brunner, 2016a).

Flood wave was determined for different analyses and the maximum velocity of water was found to be almost 69.31 m/s in the dam vicinity as shown in Figure 3.16. However, it was assumed to be almost 100 m/s to be on the safe side. Therefore, the computational time step was selected as 1 second to satisfy the Courant condition for the analyses in this case study.

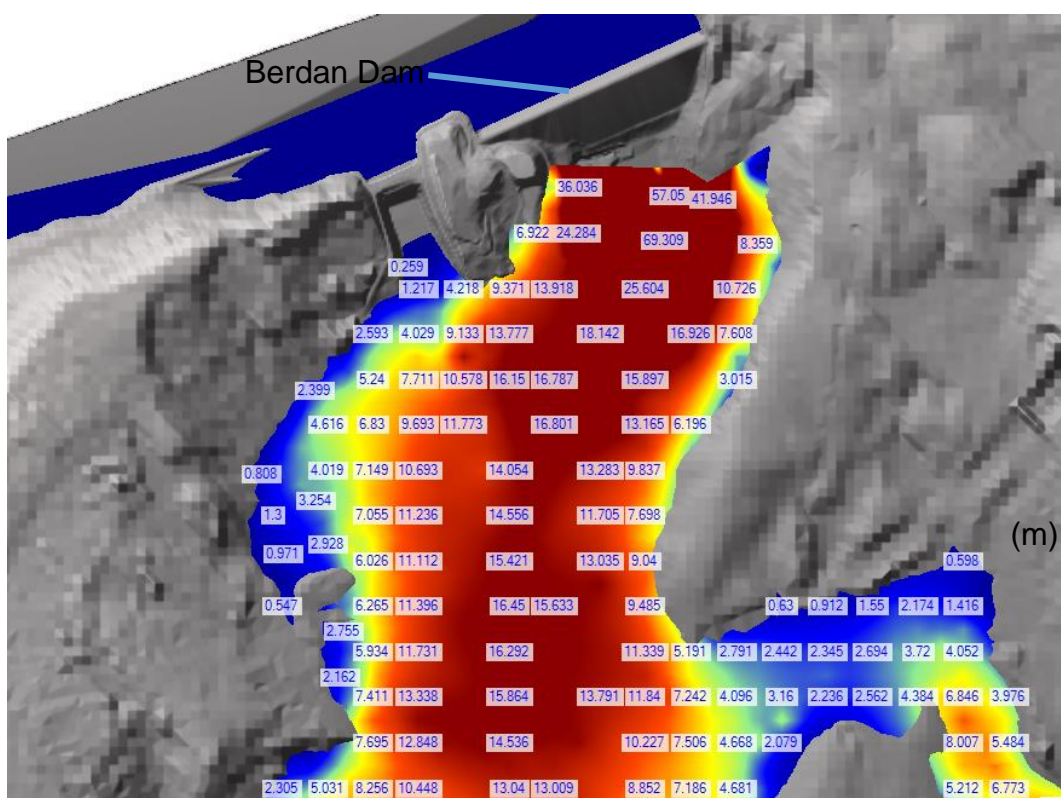


Figure 3.16. Map values of maximum velocity near Berdan Dam

3.2.5. Maximum Possible Discharge for Catastrophic Condition

In dam break analyses, catastrophic discharges are required rather than flood frequency studies in order to investigate the catastrophic flood conditions. Probable maximum flood values were taken from planning reports which were obtained from The General Directorate of State Hydraulic Works (DSİ) 6. Regional Directorate and the studies of “Determination of Flood Risk Areas of Mersin-Tarsus-Berdan River and Their Tributaries”.

For reservoir routing, average inflow and outflow rates should be considered with the change in storage. Therefore, the change in reservoir volume can be written as the difference between inflow and outflow hydrographs in a routing period (Chow, 1959).

In practical applications, the average of inflow and outflow rates are calculated with the values at the beginning and end of a routing period.

The reservoir routing equation can be introduced as:

$$\Delta S = (I_{avg} - O_{avg})\Delta t \quad (3.1)$$

where I_{avg} is the average rate of inflow, O_{avg} is the average outflow rate, Δt is the time interval of a routing period, ΔS is the change in reservoir volume during a period Δt .

The inflow hydrograph of the reservoir and the outflow hydrograph obtained from the routing operations are shown in Appendix A. (see Table A.1.)

After reservoir routing operations were accomplished, the outflow hydrograph of the reservoir can be used as a boundary condition at the connection of the reservoir and 2D flow area in HEC-RAS. Inflow and outflow hydrographs are shown in Figure 3.17.

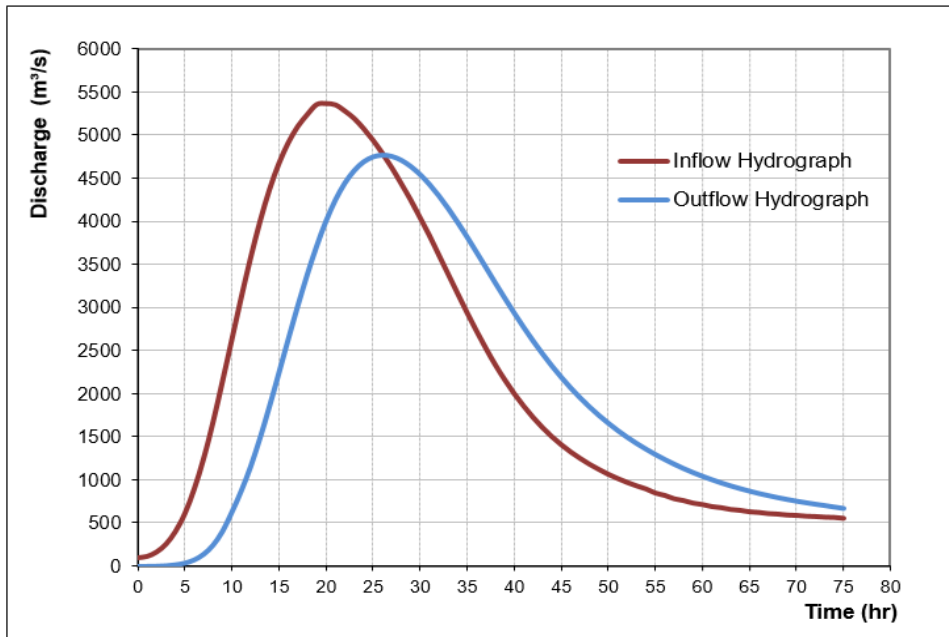


Figure 3.17. Inflow and outflow hydrographs

3.2.6. Dam Breach Parameters

In dam break analysis, breach mechanisms are determined as well as the unsteady flow conditions. Dam break mechanisms are based on the regression relationship between the breach parameters and characteristics of the dam. The mathematical relationships were developed with the data which was collected from the historical dam failures and physical models in order to investigate the dam break phenomenon. These techniques are based on reservoir volume, depth of water, the geometry of breach formation and height of dam or joint evaluation of some of these parameters (Froehlich, 2008; MacDonald & Langridge-Monopolis, 1984; Von Thun & Gillette, 1990; Wahl, 1998, 2004; Xu & Zhang, 2009).

Breach formation generally grows in trapezoidal shape for the earthfill and rockfill dams (Bozkuş & Bağ, 2011).

The geometry of a trapezoidal dam breach is represented with the side slope of the breach (z), bottom width of the breach (W_b), the height of the final breach (h_b), the height of the breach base at an instant during the breach formation (h_0), and water surface elevation (h) as shown in Figure 3.16.

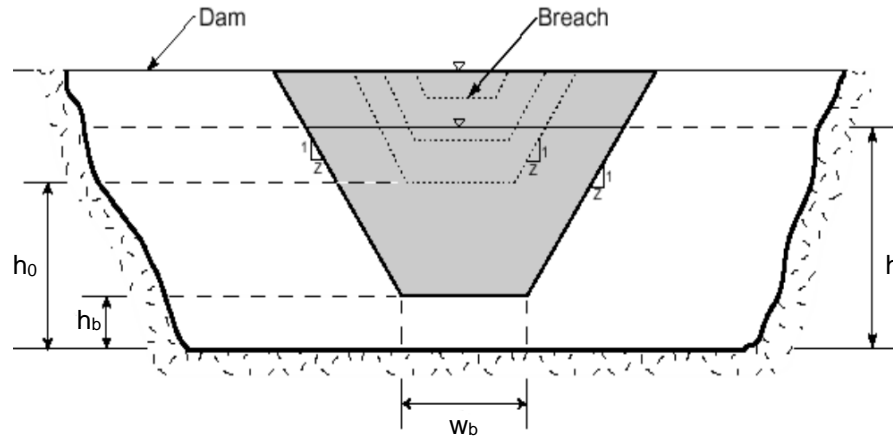


Figure 3.18. Parameters of a trapezoidal breach (Bozkuş & Bağ, 2011)

Prediction of breach parameters may vary from the dam to dam and may also vary for the same dam under different circumstances considering the different dam break scenarios. In literature, some of the physical and numerical models have been examined to determine critical parameters of the dam breach and to compare the results.

Breach formation time and geometry of the final breach are vital for risk assessments. Determining the breach formation time not only use to determine the period of the beginning of the breach formation to the moment of dam failure but also it allows to investigate the time required for evacuation of the downstream settlement from the risk area (Wahl, 1998).

The regression equations, which were verified by several dam break studies, are used in HEC-RAS. Wahl (2004) carried out an uncertainty analysis for various dam breach formulations. Mathematical relations of available dam breach mechanisms and their uncertainty analysis are summarized in Table 3.5.

Table 3.5. Dam breach mechanisms in HEC-RAS

| Method | Equation | Number of Cases | Average Error of Estimation (log cycles) | Uncertainty Interval (log cycles) |
|---|--|-----------------|--|-----------------------------------|
| <i>Average Width of Final Breach</i> | | | | |
| Bureau of Reclamation (1988) | $B_{avg}=3h_w$ | 70 | -0.09 | ±0.43 |
| MacDonald and Langridge-Monopolis (1984) | $B_{avg}=V_{er}/(h_b*W_b)$ | 58 | -0.01 | ±0.82 |
| Von Thun and Gillette (1990) | $B_{avg}=2.5h_w+C_b$ | 70 | +0.09 | ±0.35 |
| Froehlich (1995a) | $B_{avg}=0.1803K_oV^{0.32}h^{0.19}$ | 75 | +0.01 | ±0.39 |
| <i>Breach Formation Time</i> | | | | |
| MacDonald and Langridge-Monopolis (1984) | $t_f=0.0179 V_{er}^{0.364}$ | 35 | -0.21 | ±0.83 |
| Von Thun and Gillette (1990) | $t_f=0.015h_w$ (highly erodible) | 34 | -0.64 | ±0.95 |
| | $t_f=0.020h_w+0.25$ (erosion resistant) | | | |
| Von Thun and Gillette (1990) | $t_f=B_{avg}/(4h_w+61)$ (highly erodible) | 35 | -0.38 | ±0.84 |
| | $t_f=B_{avg}/(4h_w)$ (erosion resistant) | | | |
| Froehlich (1995a) | $t_f=0.00254(V_w)^{0.53}h^{-0.9}$ | 33 | -0.22 | ±0.64 |
| Bureau of Reclamation (1988) | $t_f=0.011(B_{avg})$ | 39 | -0.40 | ±1.02 |

According to the uncertainty analysis, the formulations of MacDonald & Langridge-Monopolis (1984) and Froehlich (2008) yielded better results in terms of final breach width and breach formation time. In addition, Froehlich (2008) examined more earthfill dams in case studies than others. Whatsmore, the dams which were used in the case studies that form the basis of the Froehlich (2008) formulation reflects the characteristics of the Berdan Dam. Therefore, the dam breach mechanism of Froehlich (2008) was found more appropriate for Berdan Dam.

Breach formulations which are under the unsteady flow analysis options are used in order to define the dam break phenomenon in a model in HEC-RAS. The dam body was defined as a connection between the storage area and 2D flow area so that connection can state a boundary condition line on which the outflow hydrograph of Berdan Reservoir is introduced. Thus, breaching of connection means breaching of the dam body in the dam break model.

Trapezoidal breach geometry of Berdan Dam, breach progression and calculated parameters with different dam breach mechanisms are shown in Figure 3.19, Figure 3.20, and Figure 3.21, respectively.

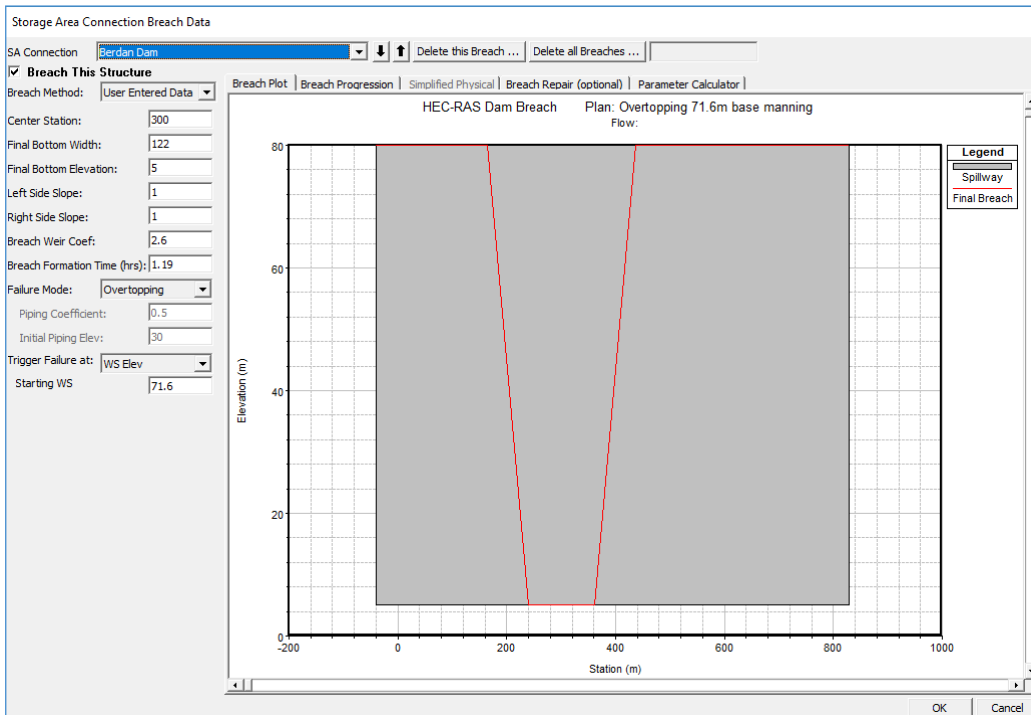


Figure 3.19. Breach geometry at the connection

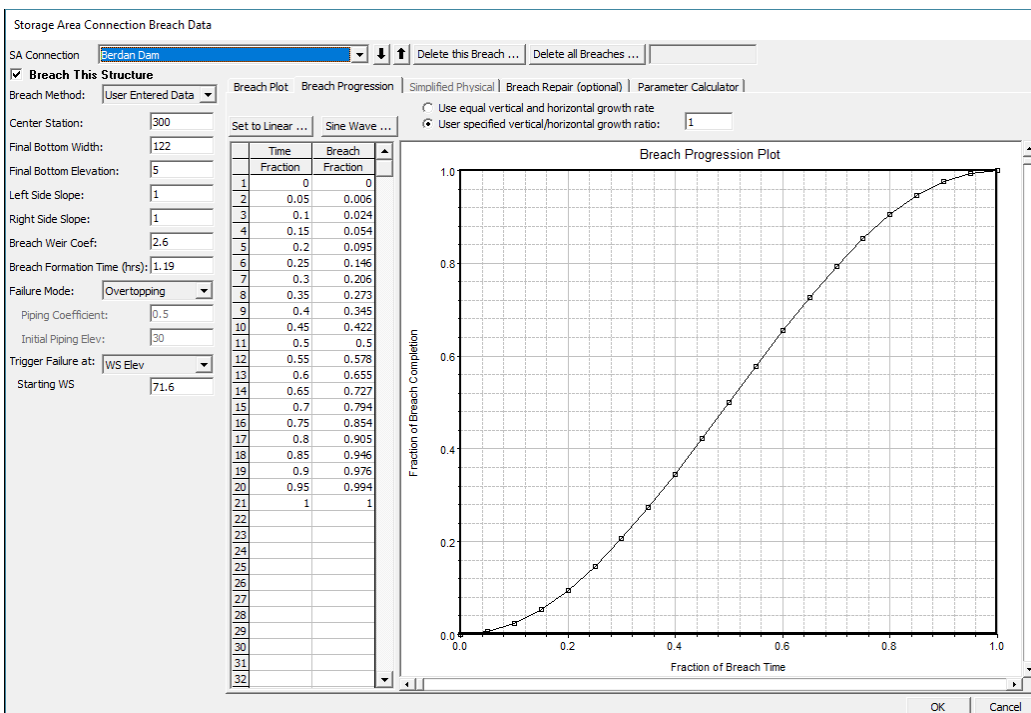


Figure 3.20. Breach progression curve

Storage Area Connection Breach Data

SA Connection: Berdan Dam

Breach This Structure

Breach Method: User Entered Data

Center Station: 300

Final Bottom Width: 122

Final Bottom Elevation: 5

Left Side Slope: 1

Right Side Slope: 1

Breach Weir Coef: 2.6

Breach Formation Time (hrs): 1.19

Failure Mode: Overtopping

Piping Coefficient: 0.5

Initial Piping Elev: 30

Trigger Failure at: WS Elev

Starting WS: 71.6

Breach Plot | Breach Progression | Simplified Physical | Breach Repair (optional) | Parameter Calculator

Input Data

Top of Dam Elevation (m): 71.6

Breach Bottom Elevation (m): 5

Pool Elevation at Failure (m): 71.6

Pool Volume at Failure (1000 m³): 1998.10

Failure mode: Overtopping

MacDonald

Dam Crest Width (m): 3

Slope of US Dam Face Z1 (H:V): 3

Earth Fill Type: Non-homogeneous or Rockfill

Slope of DS Dam Face Z2 (H:V): 3

Xu Zhang (and Von Thun)

Dam Type: Dam with corewall

Dam Erodibility: Medium

| Method | Breach Bottom Width (m) | Side Slopes (H:V) | Breach Development Time (hrs) | |
|--------------------|-------------------------|-------------------|-------------------------------|--------|
| MacDonald et al | 86 | 0.5 | 3.15 | Select |
| Froehlich (1995) | 161 | 1.4 | 1.46 | Select |
| Froehlich (2008) | 122 | 1 | 1.19 | Select |
| Von Thun & Gillete | 188 | 0.5 | 1.58 | Select |
| Xu & Zhang | 210 | 0.68 | 2.89 * | Select |

* Note: the breach development time from the Xu Zhang equation includes more of the initial erosion period and post erosion than what is used in the HEC-RAS breach formation time.

OK Cancel

Figure 3.21. Calculated breach parameters for different mechanisms

3.3. Complete Procedure of 2D Dam Break Analyses with HEC-RAS

First of all, the bathymetric map is created with aerial photographs and measurements obtained from field studies for both river bed and flood plain. DEM is generated from the bathymetric map, and then it is converted to a TIN map with HEC-geoRAS tool in ArcGIS.

The terrain is classified by the land characteristics in order to determine Manning's roughness coefficient values of different land uses. Different roughness values are assigned according to the characteristic features of these regions and processed into the geometric data in an attribute table. Then, land cover can be imported to HEC-RAS from land use of the terrain created in GIS environment.

A probable maximum flood hydrograph is determined from the hydrological studies for catastrophic conditions. After reservoir routing operations, the outflow hydrograph of the reservoir can be used as an input for unsteady flow simulation in HEC-RAS.

The general process of the dam break analyses in HEC-RAS is summarized below.

- A new project is created in HEC-RAS and a projection is set.
- The TIN map is imported to HEC-RAS as a terrain. Geometric data should be created on this terrain in HEC-RAS. Reservoir and 2D flow area are created in the geometric data editor.
 - A volume-elevation or area-elevation relationship is introduced to define the reservoir characteristics.
 - The mesh size and Manning's roughness coefficient values of sub-regions were determined for the 2D flow area. Refinements can be done by defining break lines or adding/deleting grid cells if required.
- For dam break analyses, either an inline structure or a connection should be introduced to represent the dam body. Then, a breach geometry is defined at the dam body by using terrain coordinates.
- Initial and boundary conditions were determined for unsteady flow simulation. Boundary condition lines can be drawn in the geometric data editor.
- Before starting to run the simulations, hydraulic properties of the 2D flow area should be computed. In addition, land cover and geometric data should be associated with the terrain in RAS-Mapper.
- The computational time interval is determined according to the conditions which were mentioned in Chapter 3.
- After analyses were performed, the results of the analyses can be viewed in RAS-Mapper. Map layers can be managed and related associations can be done for the HEC-RAS project.
- Flood inundation maps are displayed in terms of depth, velocity and water surface elevation as stored maps by default. In addition, maps of other results like flood arrival time, inundation boundary, flood duration can be generated by the post-processing option in RAS-Mapper.

A general scheme of dam break analyses is shown in Figure 3.22.

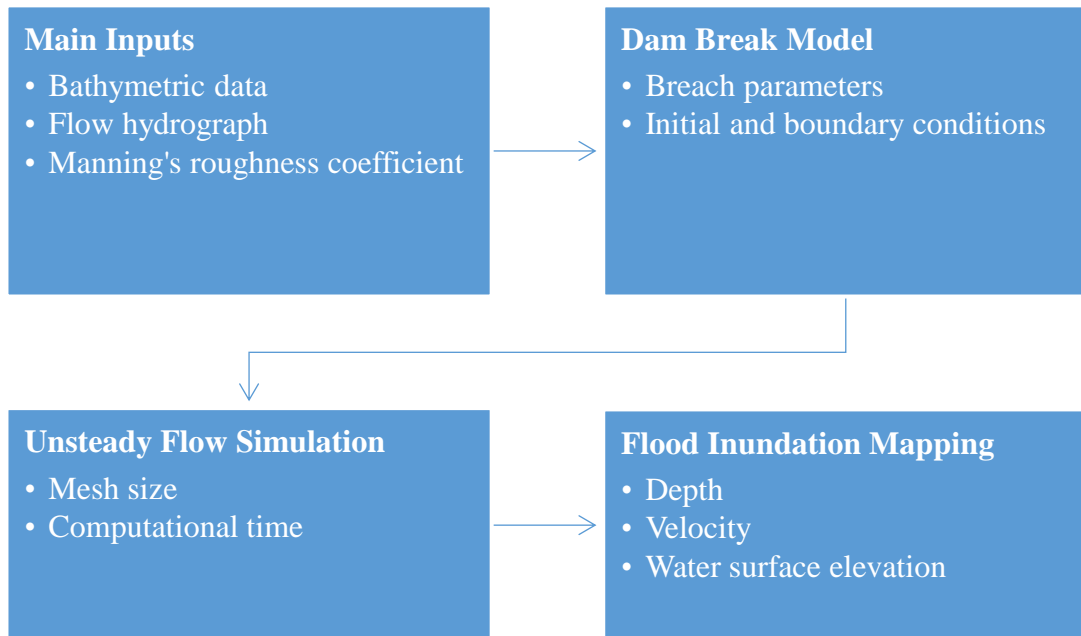


Figure 3.22. Process chart of dam break analyses

CHAPTER 4

TWO-DIMENSIONAL DAM BREAK ANALYSES

4.1. Dam Break Analyses

For this case study, 23 different models were analysed and the total computational run time of these analyses was approximately 100 hours. Post-processing of the generated map layers is not included in the computational run time. The results displayed on the terrain include the flood arrival time and maximum values of depth, velocity, and water surface elevation. For all models, a 75-hour long flow hydrograph was used for unsteady flow simulation. The specifications of the computer used in the simulations are Intel ® Core™ i7 CPU and 8.00 GB RAM with 64-BIT Operating System.

4.2. Results of the Analyses with Piping Mode of Failure

Two-dimensional dam break analysis was carried out for varying Manning's roughness coefficient values as base n , $0.80 \cdot \text{base } n$ and $1.20 \cdot \text{base } n$, and 0.060 for the piping mode of failure.

RAS-Mapper allows taking profile lines or cross-sections at required length and direction in order to examine map layers of water surface elevation, depth and velocity of the water at every point on the terrain. This property facilitates the comparison of different analyses and users have a chance to see the values at any location. Therefore, different cross-sections were taken at 2500 m, 3500 m, and 5000 m away from the dam body as in Figure 4.1, Figure 4.2, and Figure 4.3.

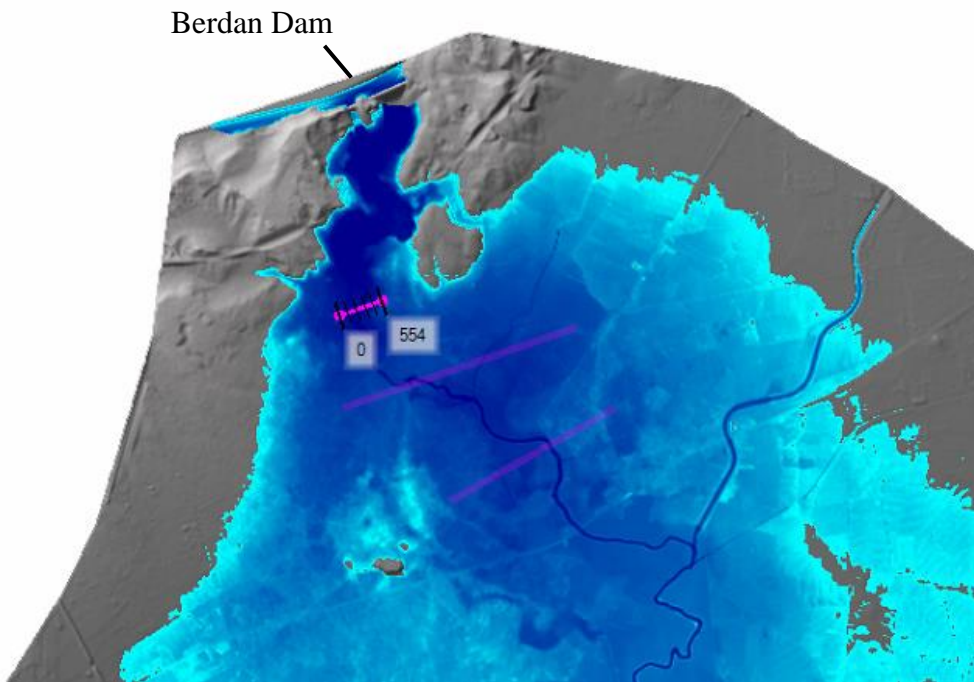


Figure 4.1. A cross-section which is 2500 m away from the dam body

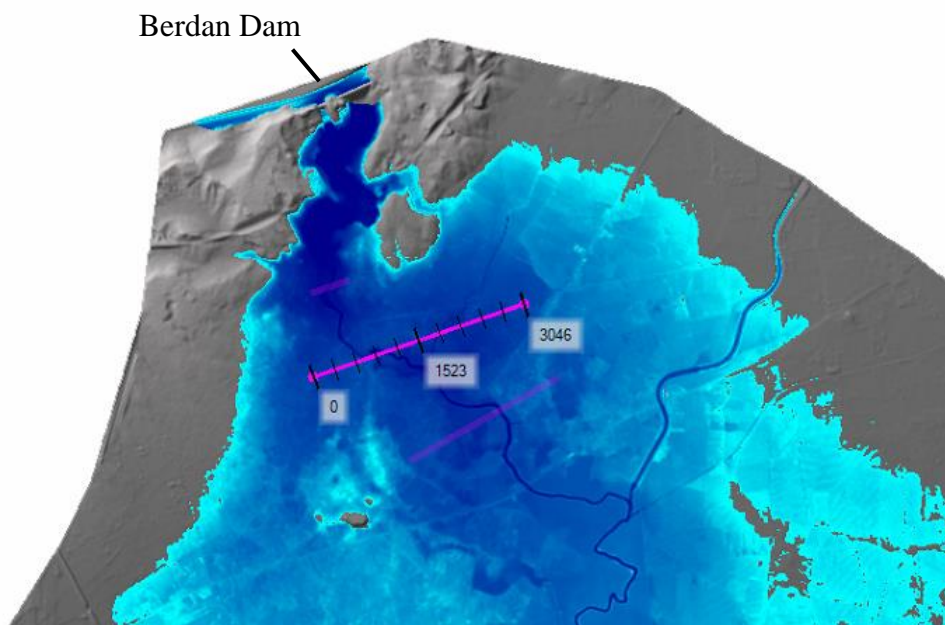


Figure 4.2. A cross-section which is 3500 m away from the dam body

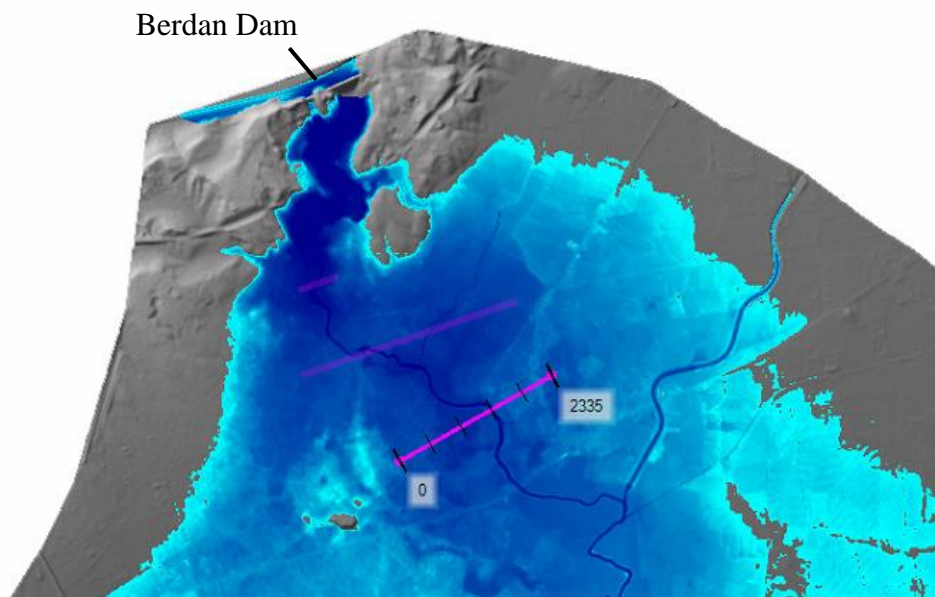


Figure 4.3. A cross-section which is 5000 m away from the dam body

Crest elevation of Berdan Dam is 71.6 meters. Therefore, the analyses were carried out with base Manning's roughness coefficient values for 10 m, 20 m, 30 m, 40 m, 50 m, and 60 m of piping elevations in order to determine the critical piping elevation.

The maximum water surface elevation values for different piping elevations were shown in Figure 4.4. The analyses for different piping elevations with base Manning's roughness coefficient values were compared. It was found that piping elevation of 30 m results in greater water surface elevation values than other piping elevations (See Figure 4.4 (continued)). In addition, the comparison of the maximum velocity values for different piping elevations was shown in Figure 4.5.

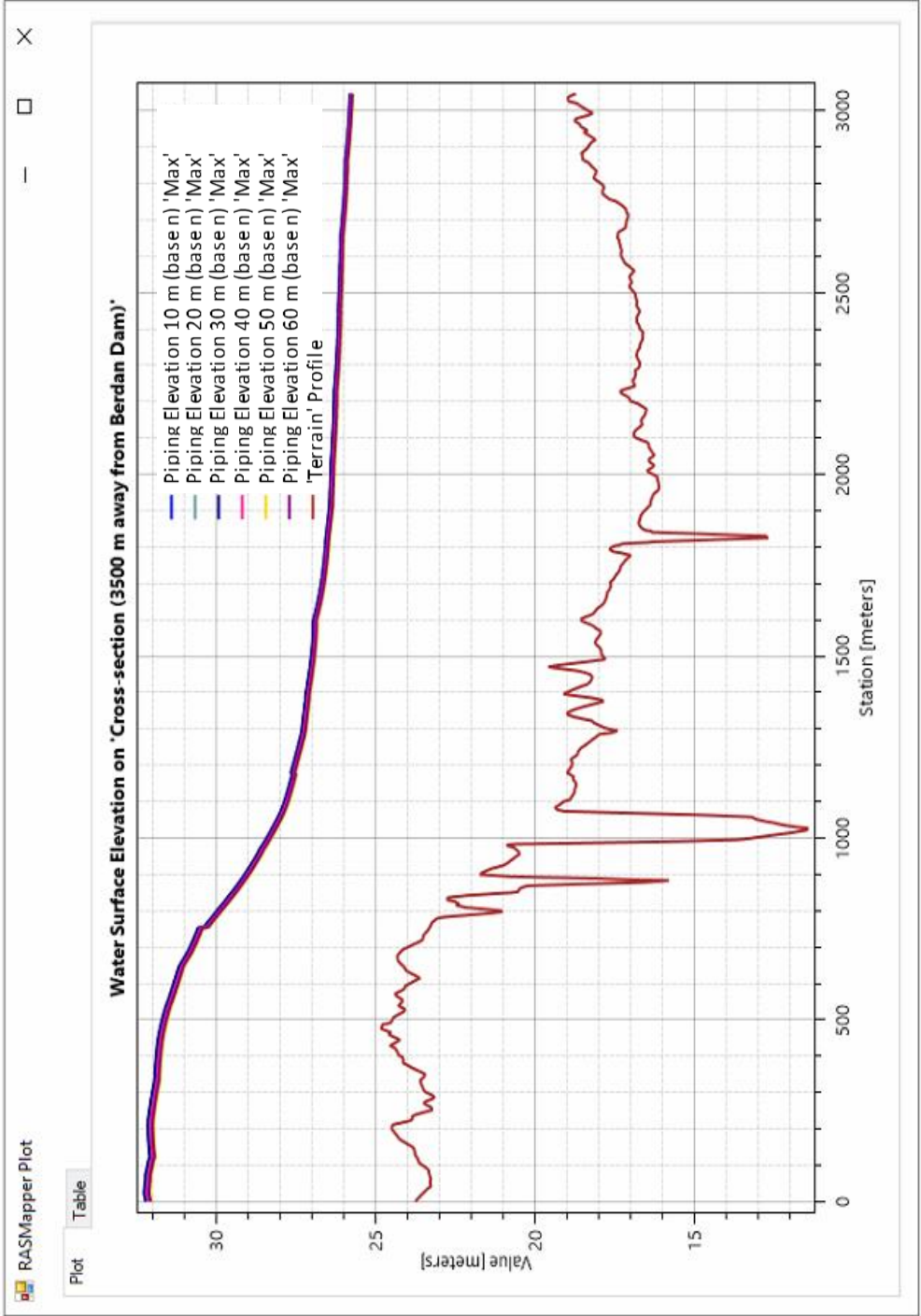


Figure 4.4. Maximum WSE values for different piping elevations with base n

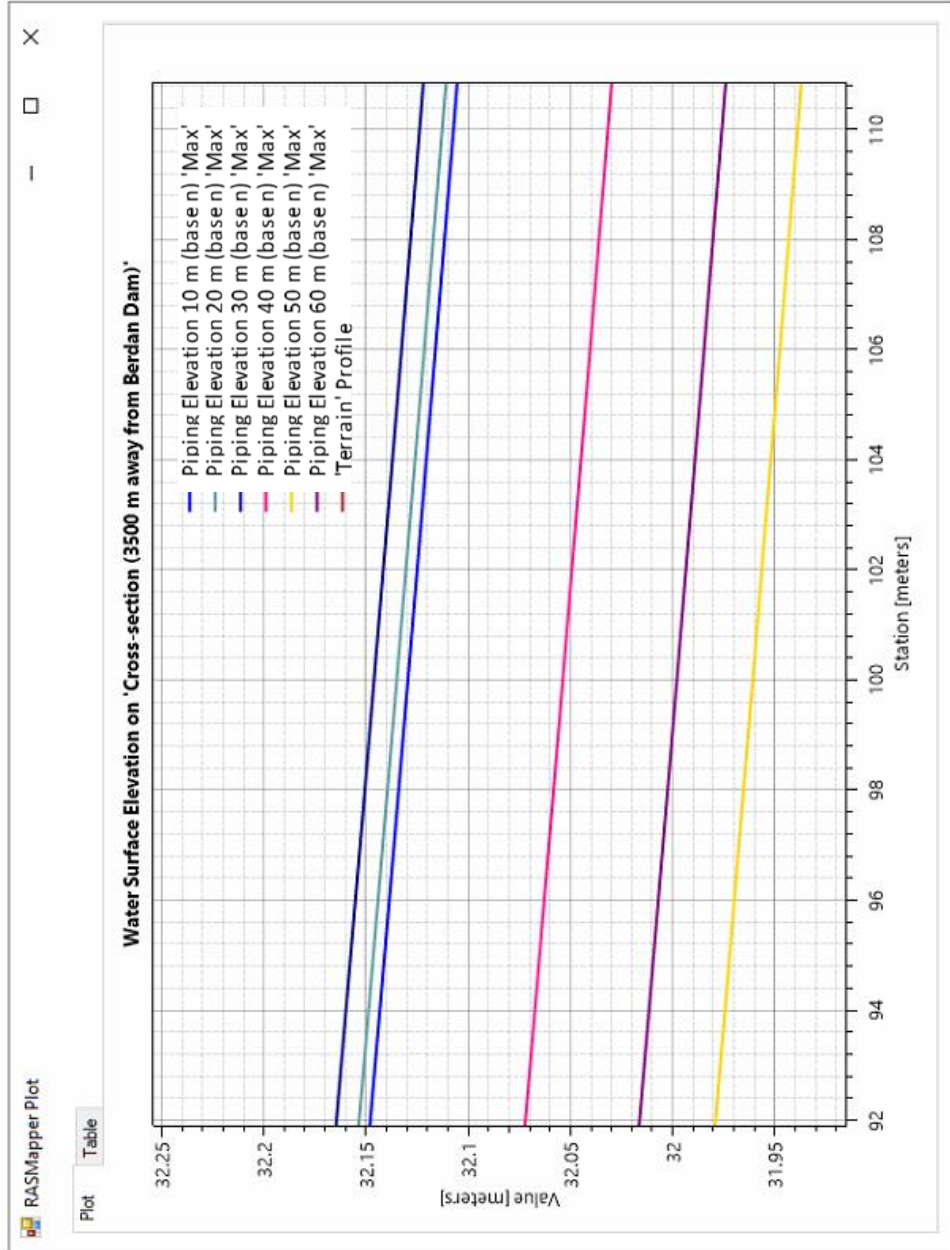


Figure 4.4 . Maximum WSE values for different piping elevations with base n (continued)

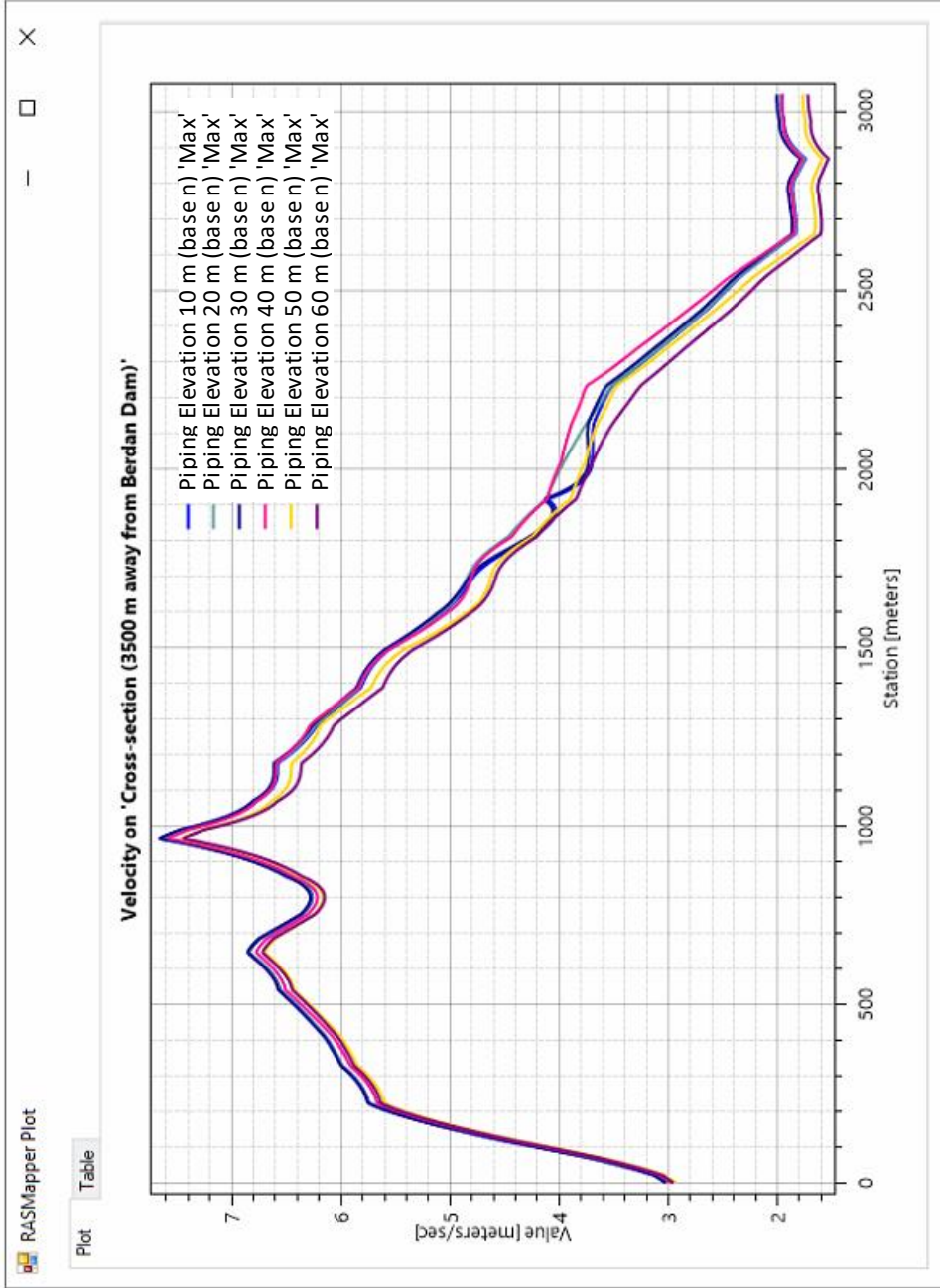


Figure 4.5. Maximum velocities for different piping elevations with base n

4.2.1. Flood Inundation for the Piping Elevation of 30 m with $0.80 \cdot \text{base } n$

Piping elevation of 30 m was found critical for the piping mode of failure. Thus, the results of the analyses for this elevation with varying Manning's roughness coefficient values were visualized by the flood inundation maps.

Distributions of maximum depth, maximum water surface elevation, maximum velocity, and flood arrival time for the piping elevation of 30 m with $0.80 \cdot \text{base } n$ were given in Figures 4.6 through 4.9.

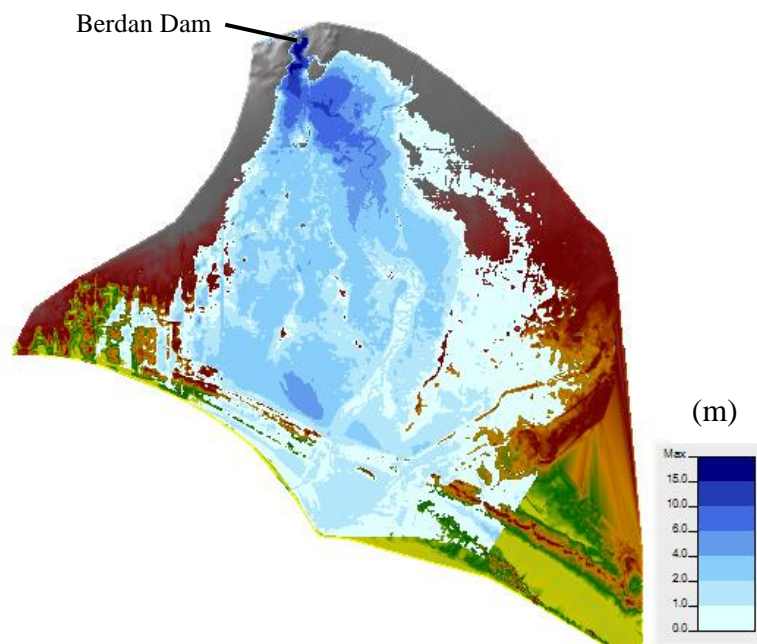


Figure 4.6. Distribution of maximum depth for the piping elevation of 30 m with $0.80 \cdot \text{base } n$

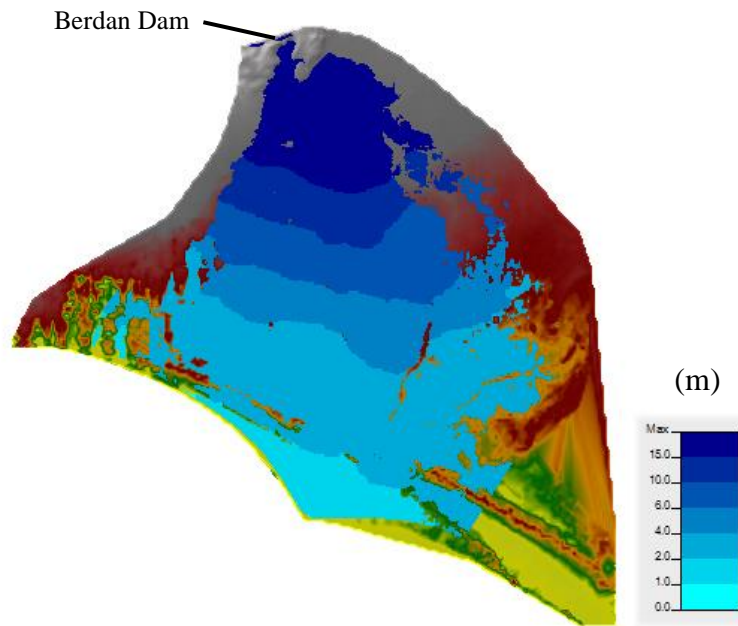


Figure 4.7. Distribution of maximum WSE for the piping elevation of 30 m with 0.80*base n

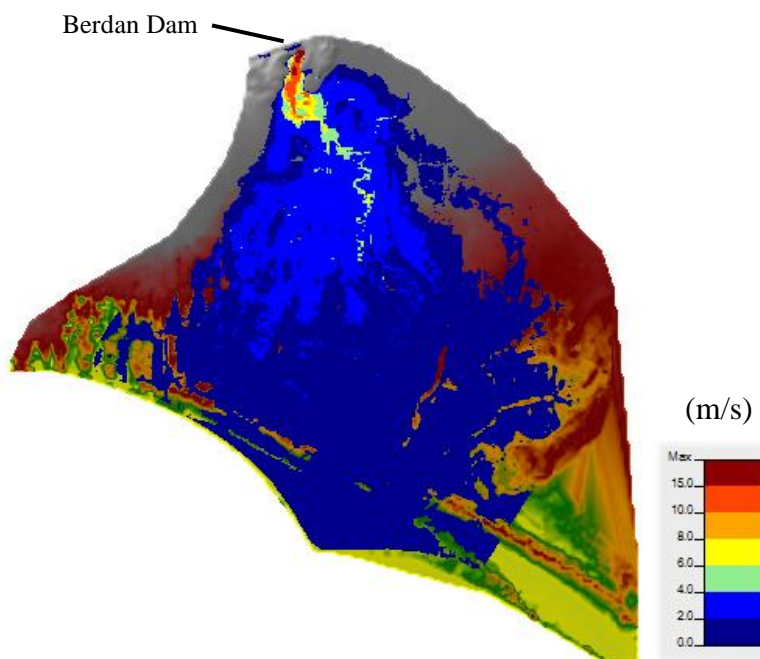


Figure 4.8. Distribution of maximum velocity for the piping elevation of 30 m with 0.80*base n

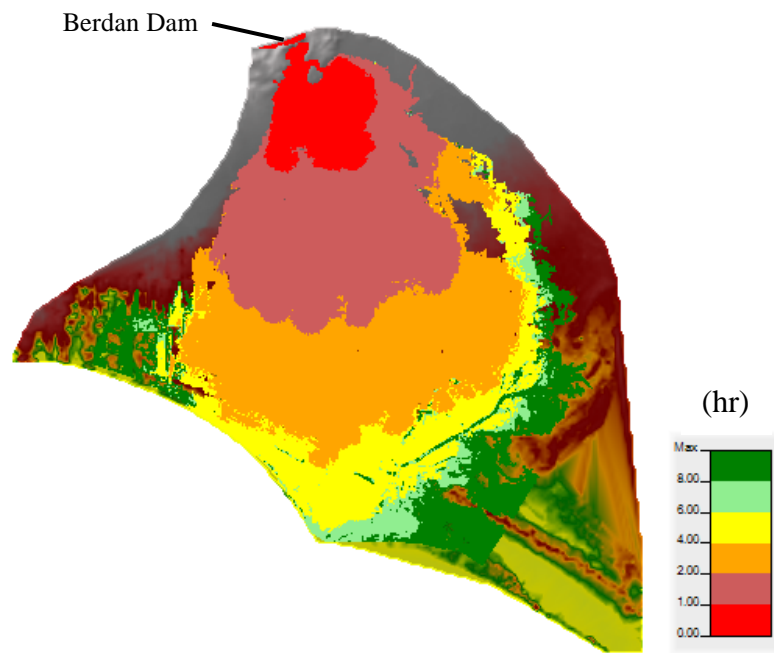


Figure 4.9. Distribution of flood arrival time for the piping elevation of 30 m with $0.80 \cdot \text{base } n$

4.2.2. Flood Inundation for the Piping Elevation of 30 m with base n

Distributions of maximum depth, maximum water surface elevation, maximum velocity, and flood arrival time for the piping elevation of 30 m with base n were given in Figures 4.10 through 4.13.

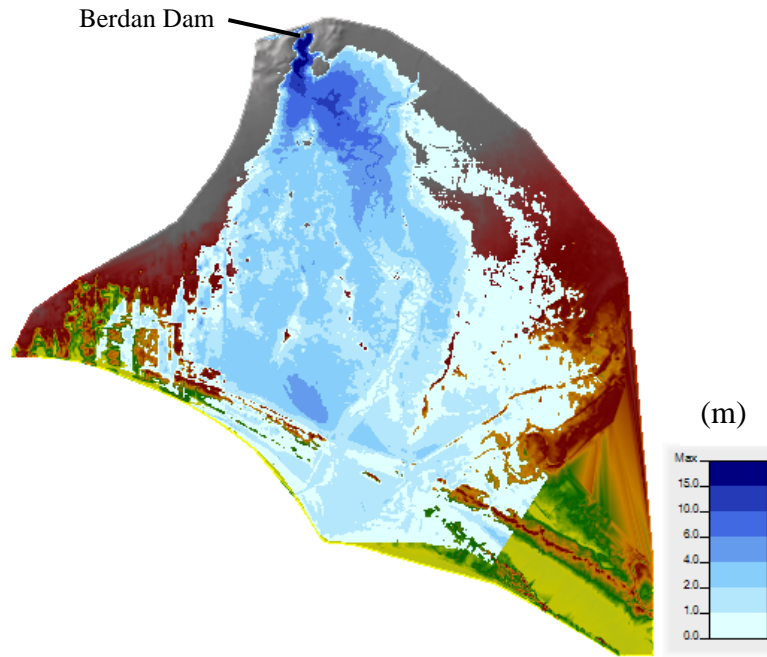


Figure 4.10. Distribution of maximum depth for the piping elevation of 30 m with base n

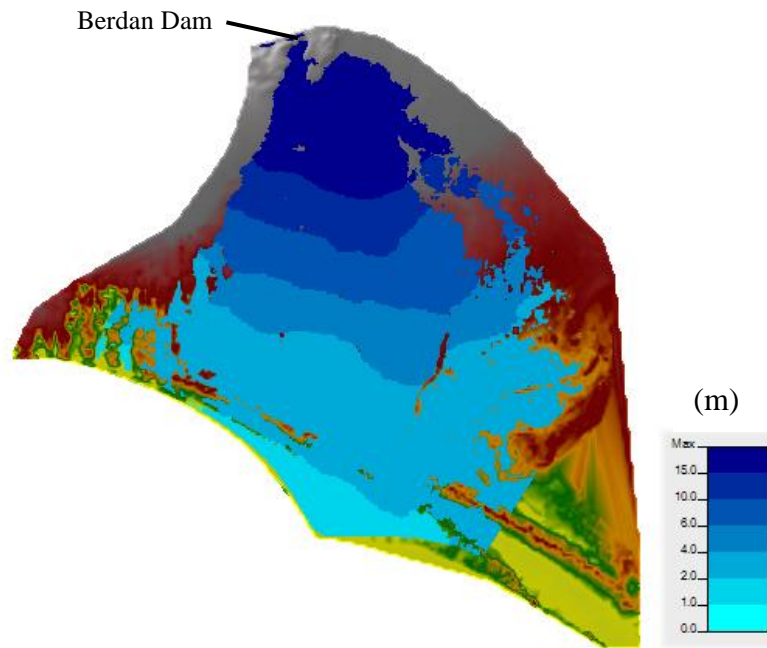


Figure 4.11. Distribution of maximum water surface elevation for the piping elevation of 30 m with base n

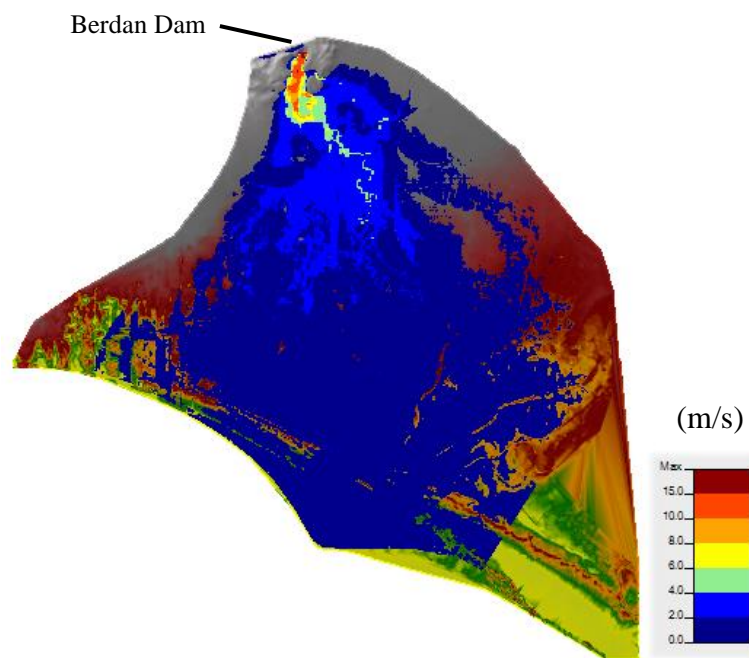


Figure 4.12. Distribution of maximum velocity for the piping elevation of 30 m with base n

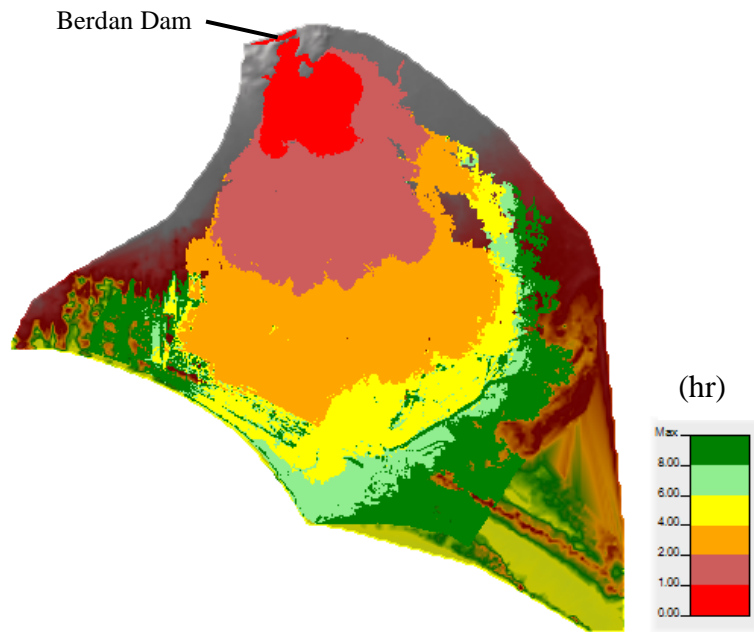


Figure 4.13. Distribution of flood arrival time for the piping elevation of 30 m with base n

4.2.3. Flood Inundation for the Piping Elevation of 30 m with $1.20 \cdot \text{base } n$

Distributions of maximum depth, maximum water surface elevation, maximum velocity, and flood arrival time for the piping elevation of 30 m with $1.20 \cdot \text{base } n$ were given in Figures 4.14 through 4.17.

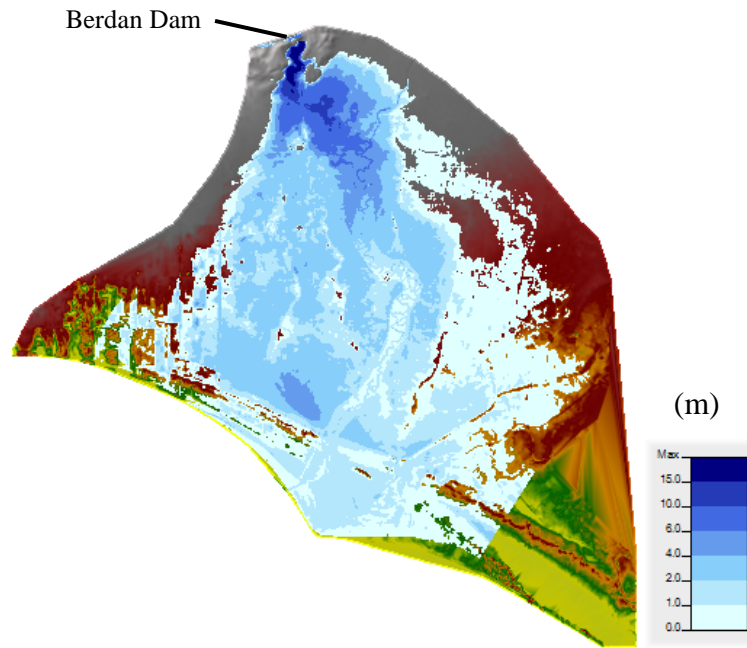


Figure 4.14. Distribution of maximum depth for the piping elevation of 30 m with $1.20 \cdot \text{base } n$

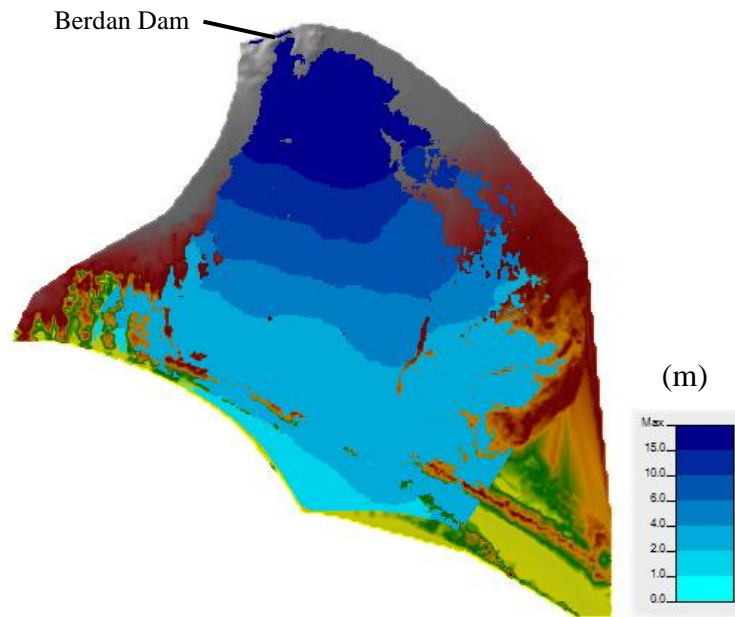


Figure 4.15. Distribution of maximum water surface elevation for the piping elevation of 30 m with 1.20*base n

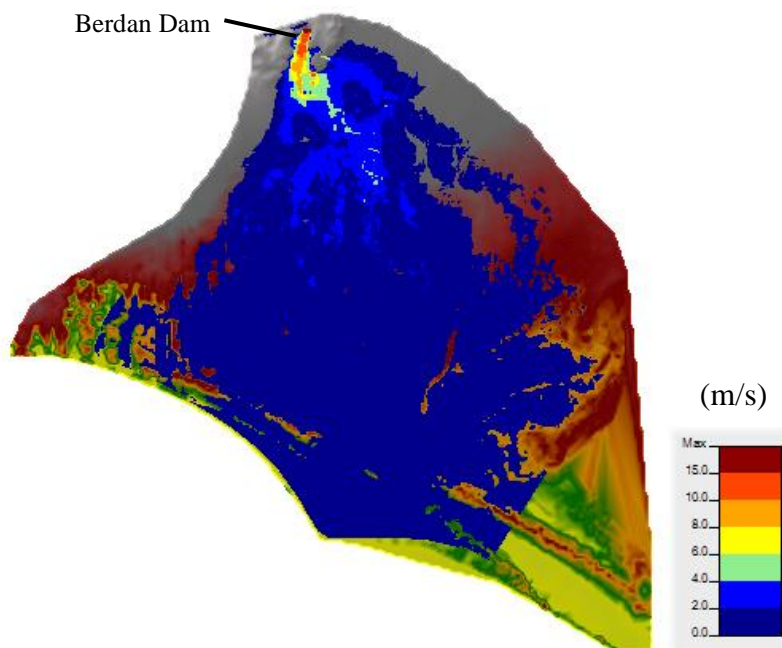


Figure 4.16. Distribution of maximum velocity for the piping elevation of 30 m with 1.20*base n

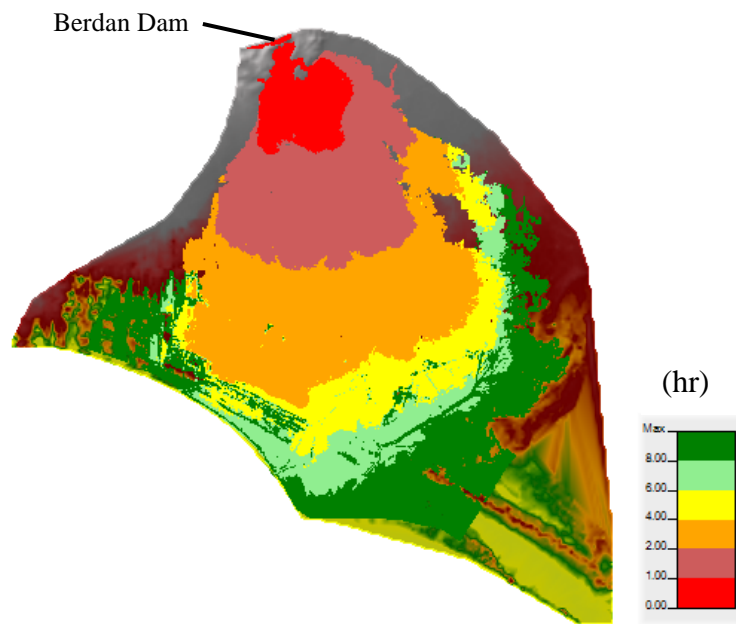


Figure 4.17. Distribution of flood arrival time for the piping elevation of 30 m with $1.20 \cdot \text{base } n$

4.2.4. Flood Inundation for the Piping Elevation of 30 m with $n=0.060$

Distributions of maximum depth, maximum water surface elevation, maximum velocity, and flood arrival time for the piping elevation of 30 m with $n=0.060$ were given in Figures 4.18 through 4.21.

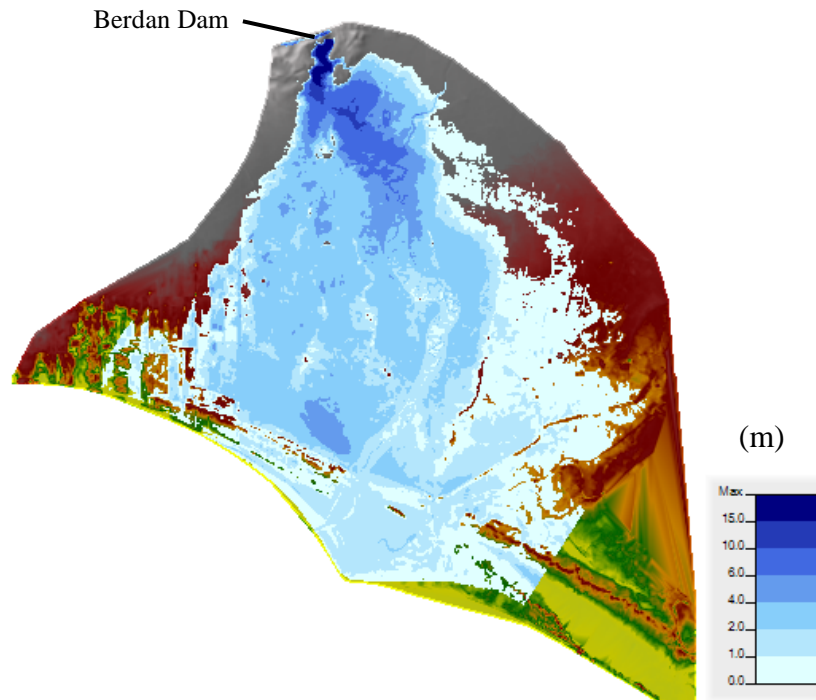


Figure 4.18. Distribution of maximum depth for the piping elevation of 30 m with $n=0.060$

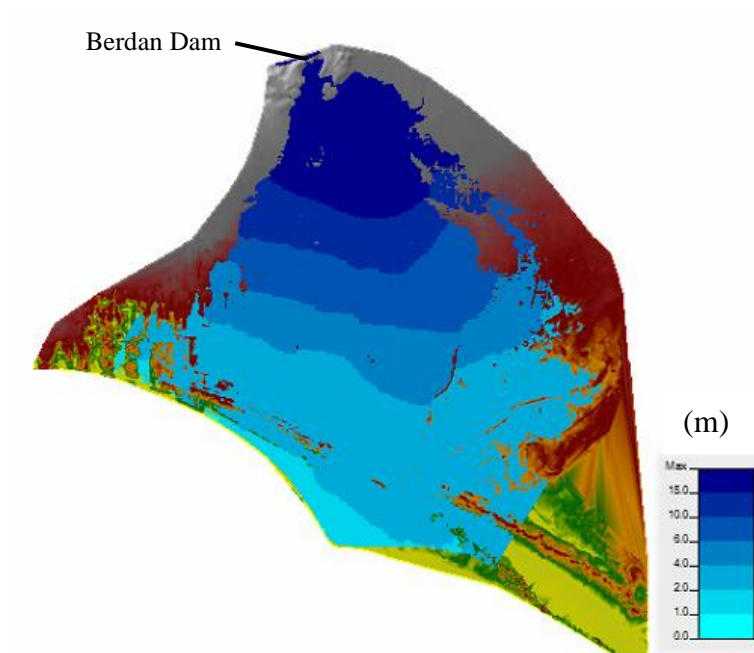


Figure 4.19. Distribution of maximum water surface elevation for the piping elevation of 30 m with $n=0.060$

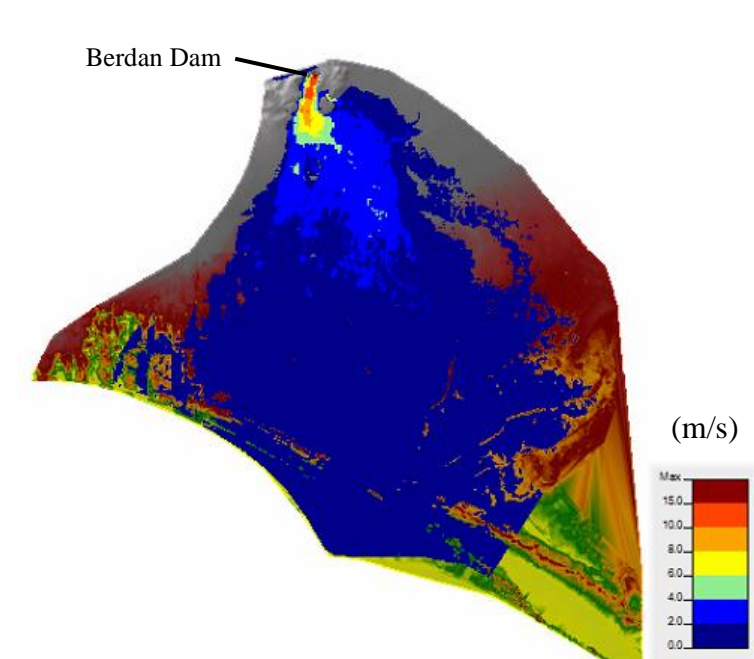


Figure 4.20. Distribution of maximum velocity for the piping elevation of 30 m with $n=0.060$

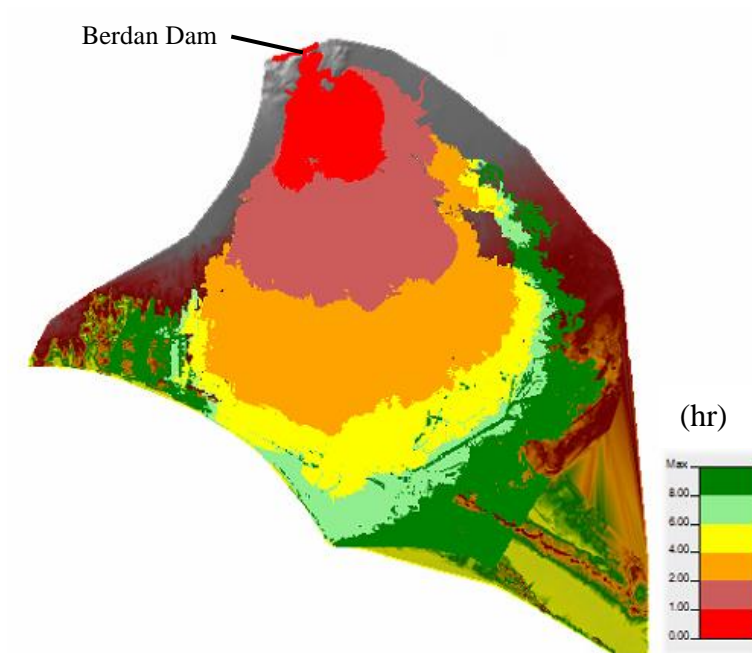


Figure 4.21. Distribution of flood arrival time for the piping elevation of 30 m with $n=0.060$

Maximum values of depth, velocity, and water surface elevation at cross-sections which are 2500 m, 3500 m, and 5000 m away from the dam body are given in Table 4.1 through 4.3.

Table 4.1. Maximum values for different piping elevations with base n at 2500 m away from the dam

| Piping elevation (m) | Maximum depth (m) | Maximum velocity (m/s) | Maximum WSE (m) |
|----------------------|-------------------|------------------------|-----------------|
| 10 | 20.29 | 9.72 | 39.25 |
| 20 | 20.30 | 9.74 | 39.26 |
| 30 | 20.31 | 9.73 | 39.28 |
| 40 | 20.17 | 9.61 | 39.14 |
| 50 | 20.05 | 9.60 | 39.01 |
| 60 | 20.11 | 9.68 | 39.07 |

Table 4.2. Maximum values for different piping elevations with base n at 3500 m away from the dam

| Piping elevation (m) | Maximum depth (m) | Maximum velocity (m/s) | Maximum WSE (m) |
|----------------------|-------------------|------------------------|-----------------|
| 10 | 16.80 | 7.66 | 32.24 |
| 20 | 16.81 | 7.66 | 32.24 |
| 30 | 16.82 | 7.68 | 32.25 |
| 40 | 16.74 | 7.60 | 32.16 |
| 50 | 16.66 | 7.47 | 32.06 |
| 60 | 16.70 | 7.46 | 32.10 |

Table 4.3. Maximum values for different piping elevations with base n at 5000 m away from the dam

| Piping elevation (m) | Maximum depth (m) | Maximum velocity (m/s) | Maximum WSE (m) |
|----------------------|-------------------|------------------------|-----------------|
| 10 | 15.15 | 4.51 | 24.22 |
| 20 | 15.16 | 4.52 | 24.22 |
| 30 | 15.16 | 4.56 | 24.23 |
| 40 | 15.13 | 4.58 | 24.19 |
| 50 | 15.09 | 4.46 | 24.14 |
| 60 | 15.11 | 4.41 | 24.16 |

For piping elevation of 30 m, the results of the analyses with varying Manning's roughness values are given in Table 4.4 through 4.6 at cross-sections which are 2500 m, 3500 m, and 5000 m away from the dam body.

Table 4.4. Comparison of maximum depths for piping

| n values | Maximum depth at 2500 m away | Maximum depth at 3500 m away | Maximum depth at 5000 m away |
|--------------|------------------------------|------------------------------|------------------------------|
| 0.80* base n | 19.22 | 16.03 | 14.87 |
| base n | 20.31 | 16.82 | 15.16 |
| 1.20*base n | 20.87 | 17.06 | 15.43 |
| n=0.060 | 19.87 | 17.04 | 15.23 |

Table 4.5. Comparison of maximum WSE values for piping

| n values | Maximum WSE at 2500 m away | Maximum WSE at 3500 m away | Maximum WSE at 5000 m away |
|--------------|----------------------------|----------------------------|----------------------------|
| 0.80* base n | 38.35 | 31.79 | 23.81 |
| base n | 39.28 | 32.25 | 24.23 |
| 1.20*base n | 40.02 | 32.93 | 24.43 |
| n=0.060 | 39.05 | 31.23 | 24.18 |

Table 4.6. Comparison of maximum velocities for piping

| n values | Maximum velocity at 2500 m away | Maximum velocity at 3500 m away | Maximum velocity at 5000 m away |
|--------------|---------------------------------|---------------------------------|---------------------------------|
| 0.80* base n | 11.29 | 10.36 | 5.12 |
| base n | 9.73 | 7.68 | 4.56 |
| 1.20*base n | 8.53 | 7.53 | 4.20 |
| n=0.060 | 8.45 | 5.97 | 3.91 |

The maximum values were mostly observed for the piping elevation of 30 m. Therefore, the analyses with different Manning's roughness coefficient values were performed with this elevation.

According to the results of analyses for the piping mode of failure, it was determined that the water depth and water surface elevation increases, while the velocity of water and flood arrival time decreases with increasing Manning's roughness coefficient values.

4.3. Results of the Analyses with Overtopping Mode of Failure

For the analyses with overtopping mode of failure, it is obvious that the resulting maximum water surface elevation increases as initial water surface elevation increases. Comparison of maximum water surface elevation and velocity values for different initial reservoir water levels of 71.6 m, 71.8 m, 72 m, 72.2 m, 72.4 m, 72.6 m with base Manning's roughness values are given in Figure 4.22 and Figure 4.23, respectively.

The water surface may rise to a certain level which is above the crest elevation for dam break analysis of earthfill dams. Therefore, it can be said that the water level cannot rise any more if the breach formation started. Thus, in addition to base Manning's roughness values, analyses that were carried out with $n=0.060$ for different initial water surface elevation values were compared. Maximum water surface elevation and maximum velocity values for different initial reservoir water levels with $n=0.060$ are shown in Figure 4.24 and Figure 4.25. It was found that the initial water level of 72 m results in the maximum velocity values. (See Figure 4.25.)

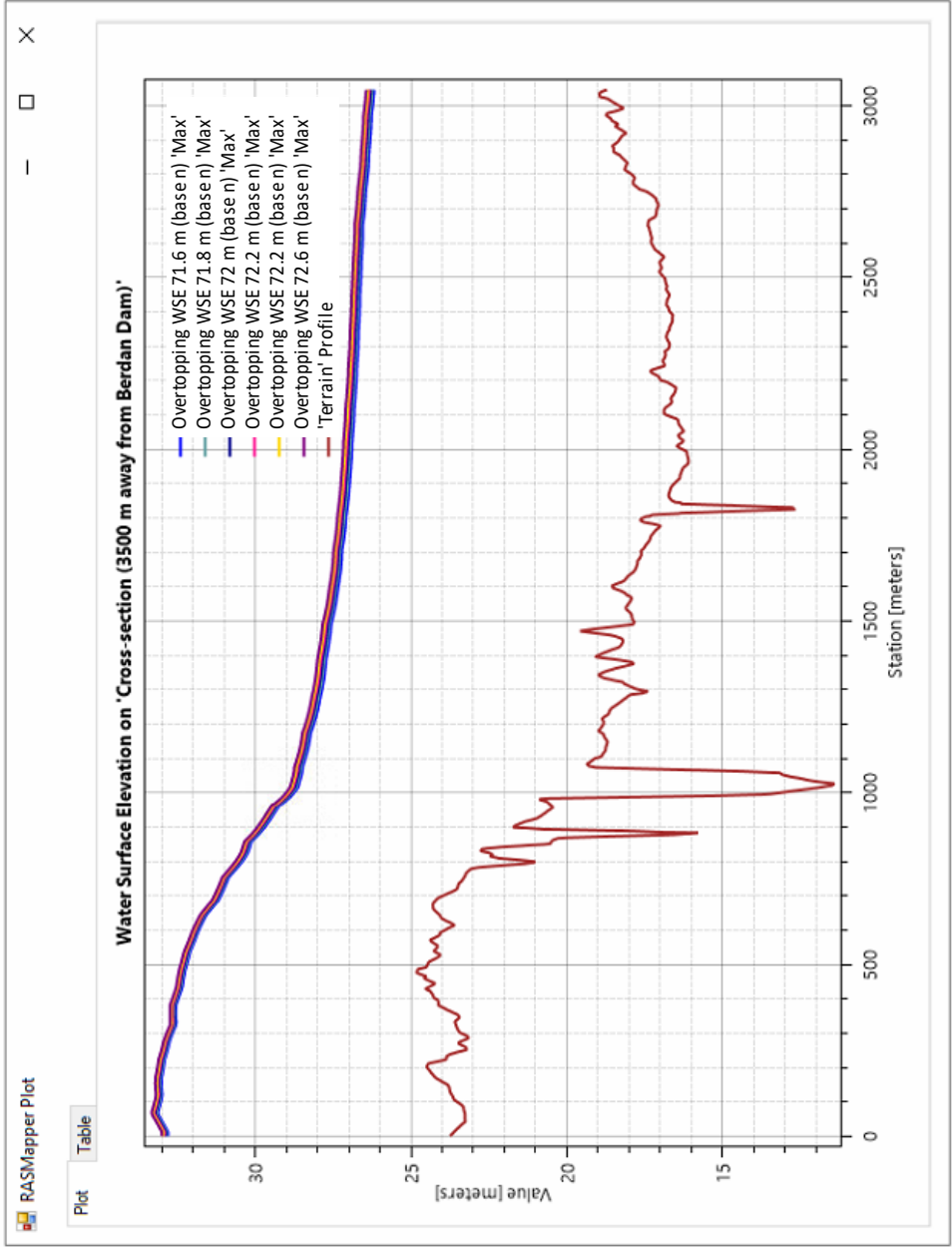


Figure 4.22. Maximum WSE values for different initial water levels with base n

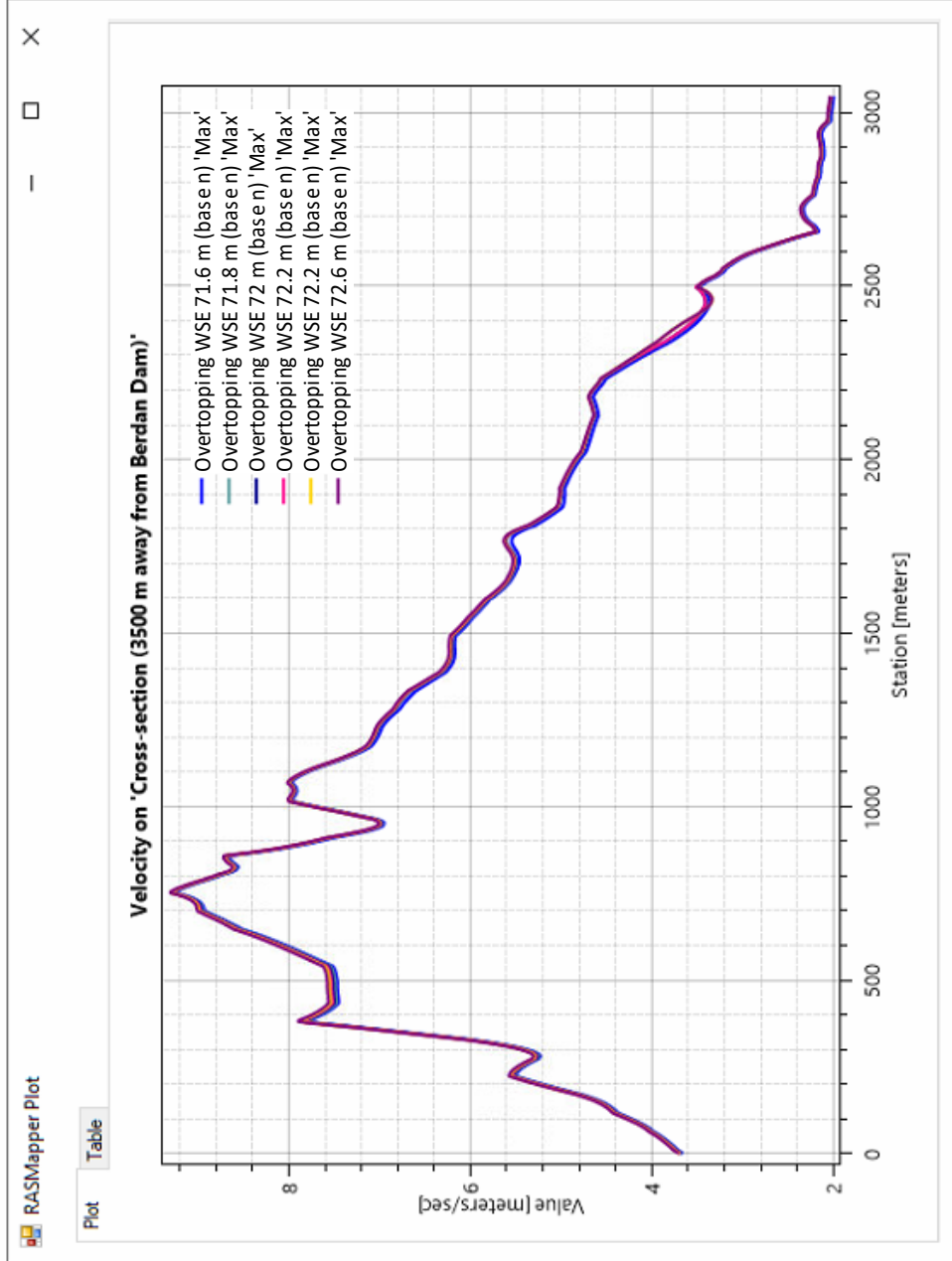


Figure 4.23. Maximum velocities for different initial water levels with base n

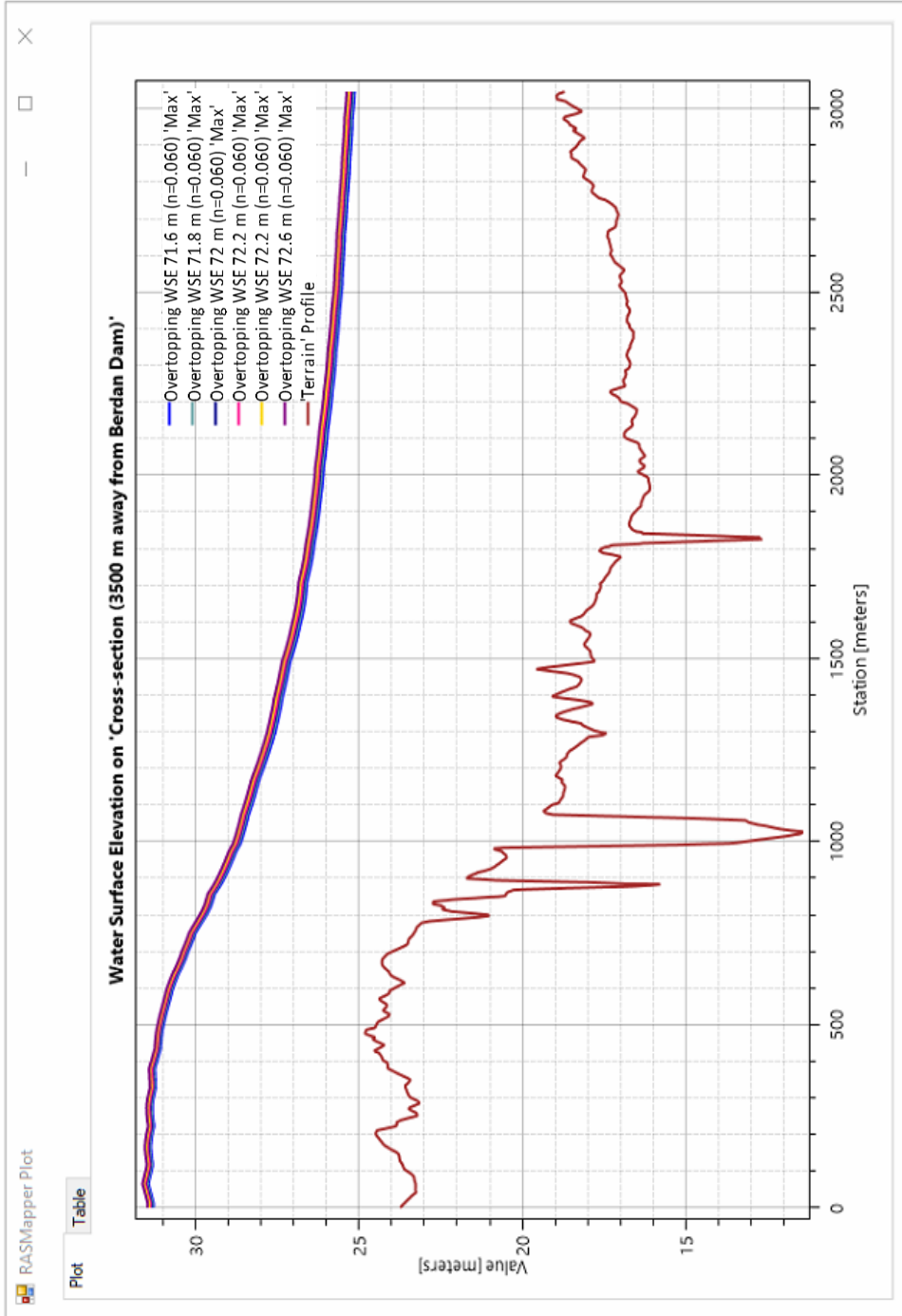


Figure 4.24. Maximum WSE values for different initial water levels with $n=0.060$

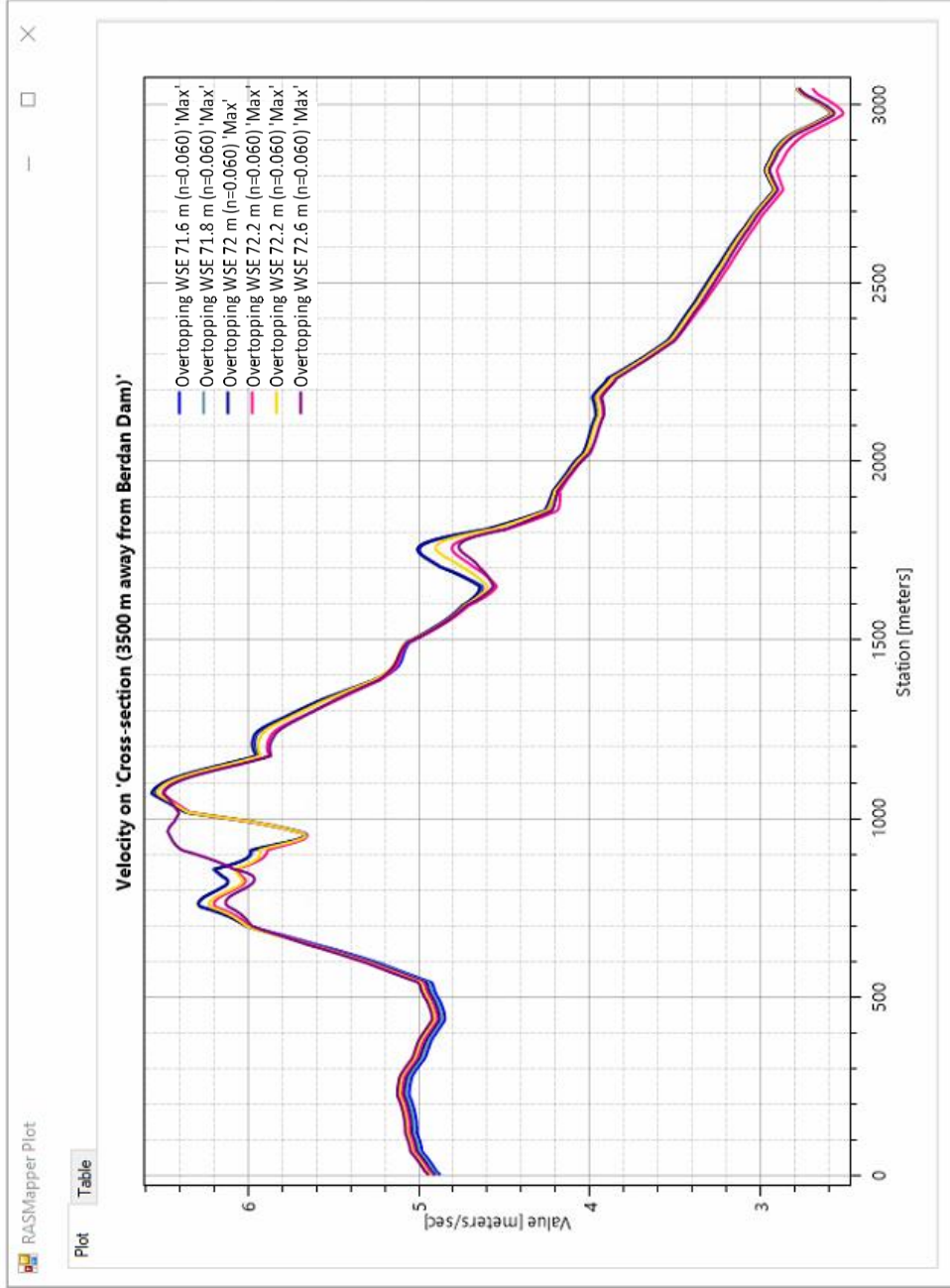


Figure 4.25. Maximum velocities for different initial water levels with $n=0.060$

4.3.1. Flood Inundation for Initial Water Level of 72 m with $0.80 \times \text{base } n$

The initial reservoir water level of 72 m was found critical for the overtopping mode of failure than the other initial water levels. Thus, the results of analyses were examined for 72 m with varying Manning's roughness coefficient values.

Distributions of maximum depth, maximum water surface elevation, maximum velocity and flood arrival time for the initial reservoir water level of 72 m with $0.80 \times \text{base } n$ were given in Figures 4.26 through 4.29.

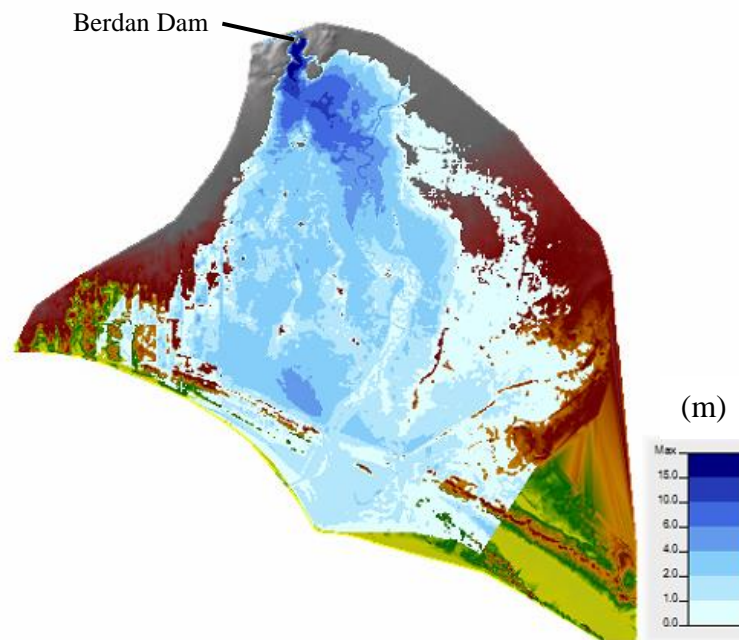


Figure 4.26. Distribution of maximum depth for initial water elevation of 72 m with $0.80 \times \text{base } n$

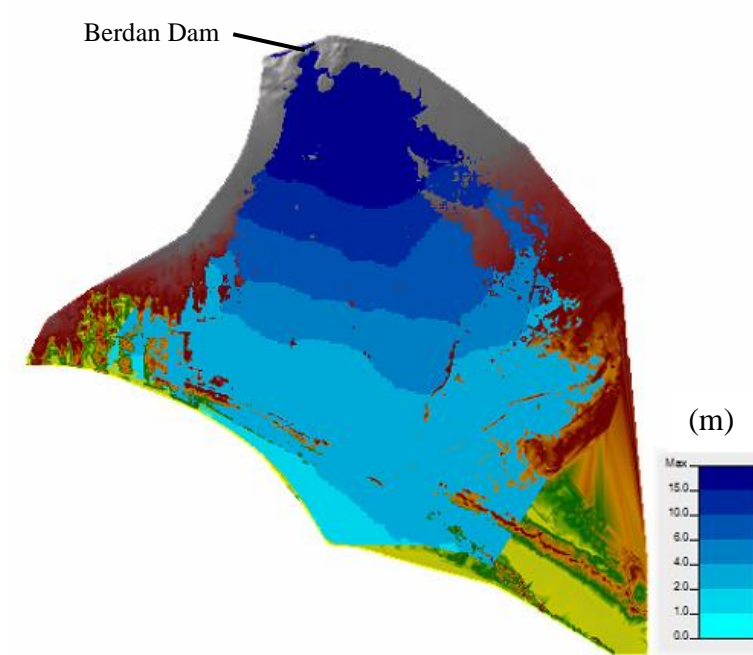


Figure 4.27. Distribution of maximum water surface elevation for initial water elevation of 72 m with $0.80 \cdot \text{base } n$

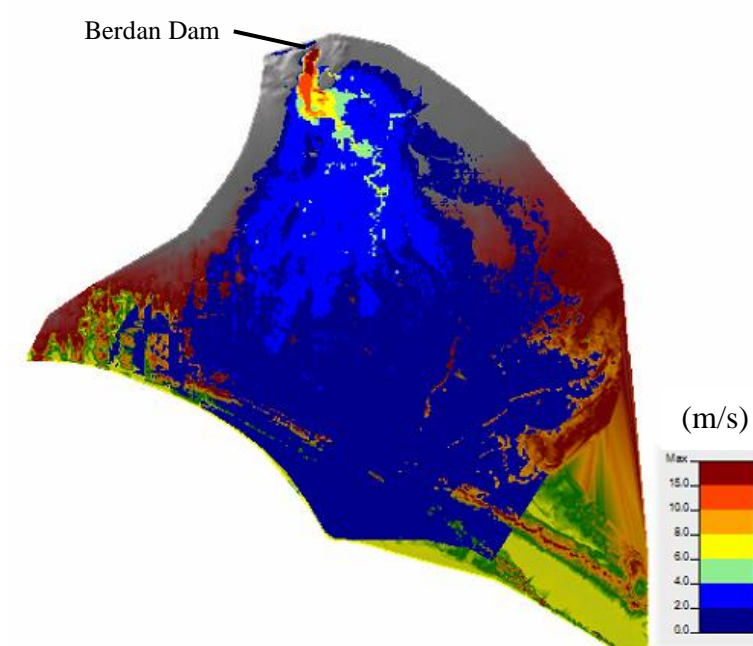


Figure 4.28. Distribution of maximum velocity for initial water elevation of 72 m with $0.80 \cdot \text{base } n$

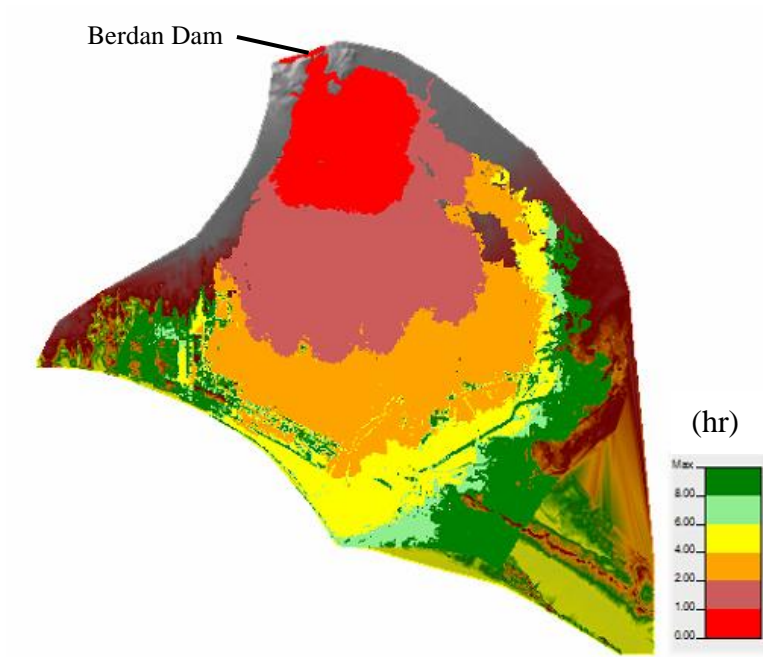


Figure 4.29. Distribution of flood arrival time for initial water elevation of 72 m with $0.80 \cdot \text{base } n$

4.3.2. Flood Inundation for Initial Water Level of 72 m with base n

Distributions of maximum depth, maximum water surface elevation, maximum velocity and flood arrival time for the initial reservoir water level of 72 m with base n were given in Figures 4.30 through 4.33.

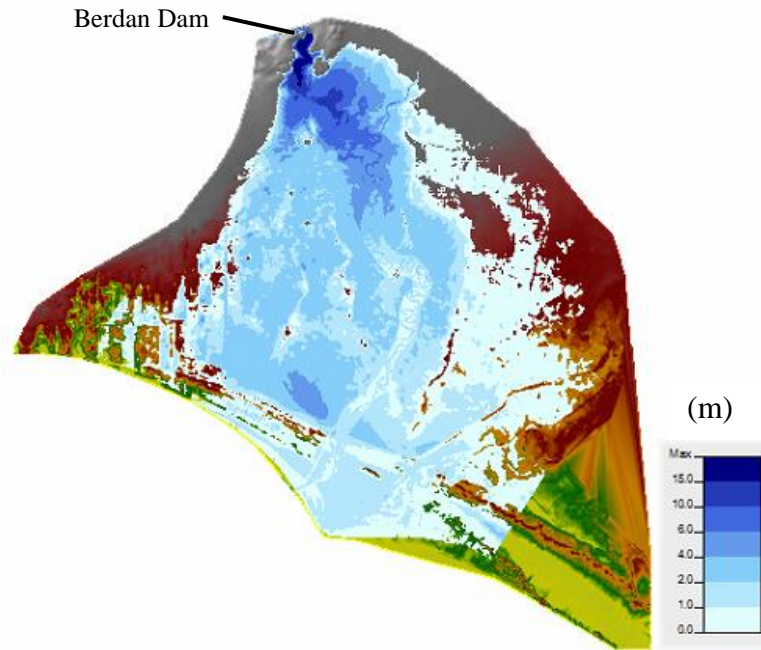


Figure 4.30. Distribution of maximum depth for initial water elevation of 72 m with base n

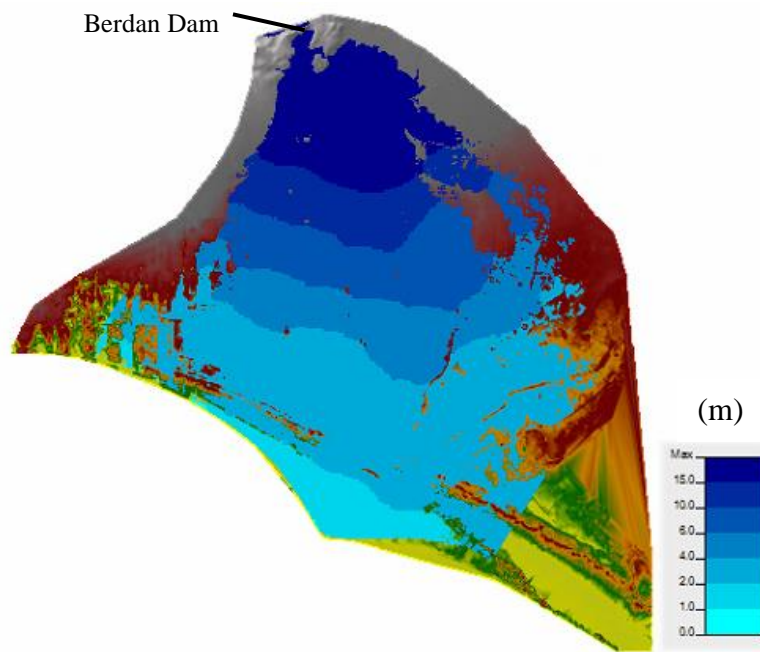


Figure 4.31. Distribution of maximum water surface elevation for initial water elevation of 72 m with base n

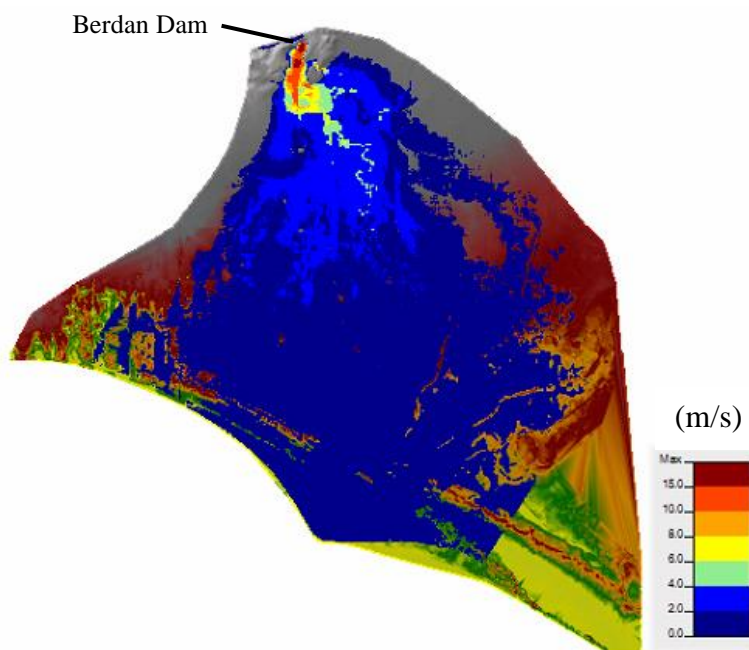


Figure 4.32. Distribution of maximum velocity for initial water elevation of 72 m with base n

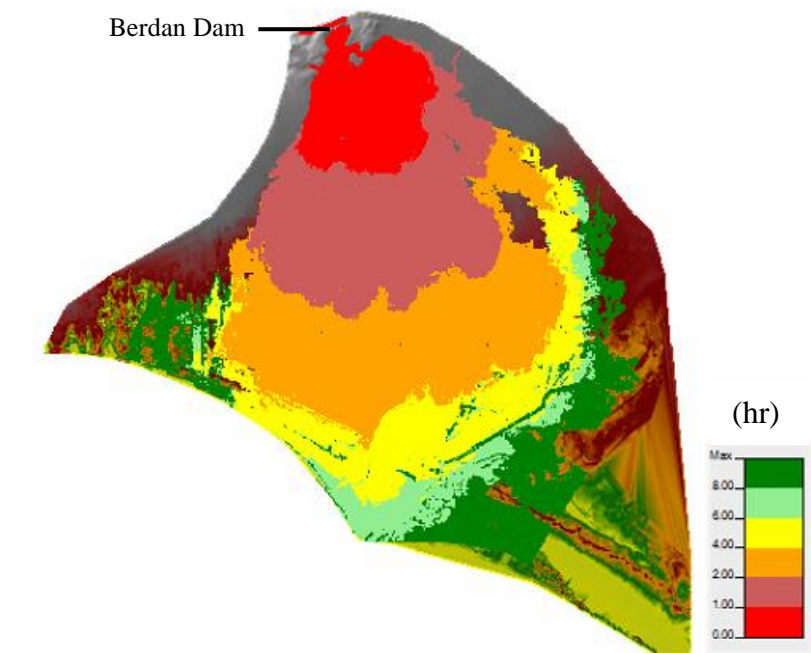


Figure 4.33. Distribution of flood arrival time for initial water elevation of 72 m with base n

4.3.3. Flood Inundation for Initial Water Level of 72 m with $1.20 \times \text{base } n$

Distributions of maximum depth, maximum water surface elevation, maximum velocity and flood arrival time for the initial reservoir water level of 72 m with $1.20 \times \text{base } n$ were given in Figures 4.34 through 4.37.

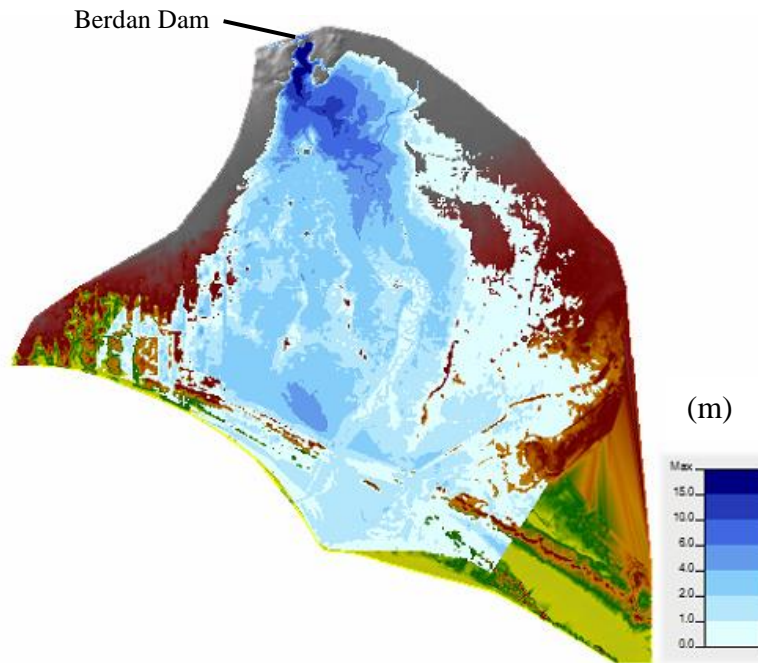


Figure 4.34. Distribution of maximum depth for initial water elevation of 72 m with $1.20 \times \text{base } n$

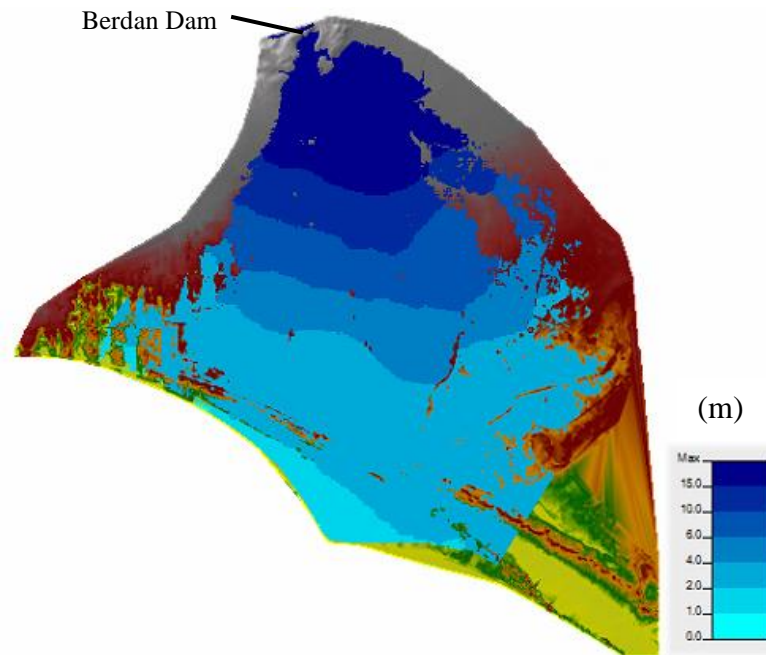


Figure 4.35. Distribution of maximum water surface elevation for initial water elevation of 72 m with 1.20*base n

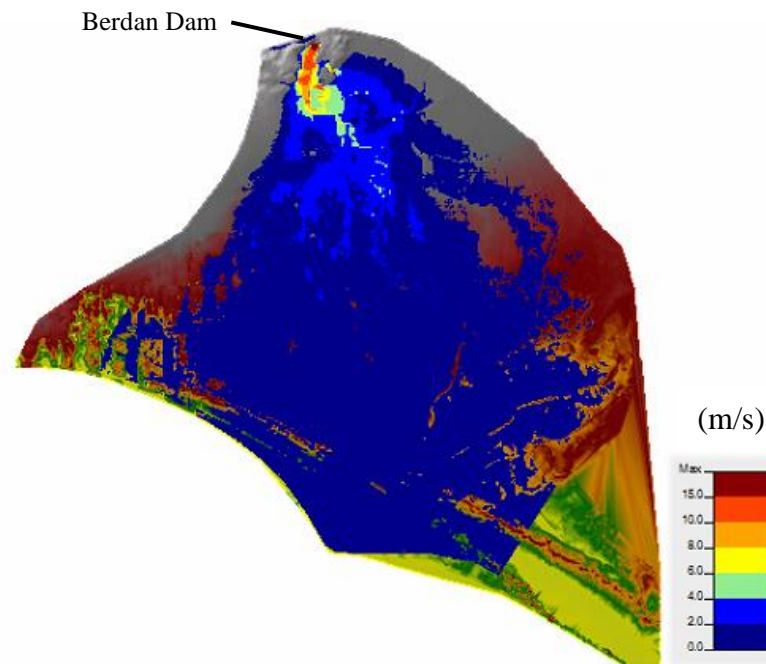


Figure 4.36. Distribution of maximum velocity for initial water elevation of 72 m with 1.20*base n

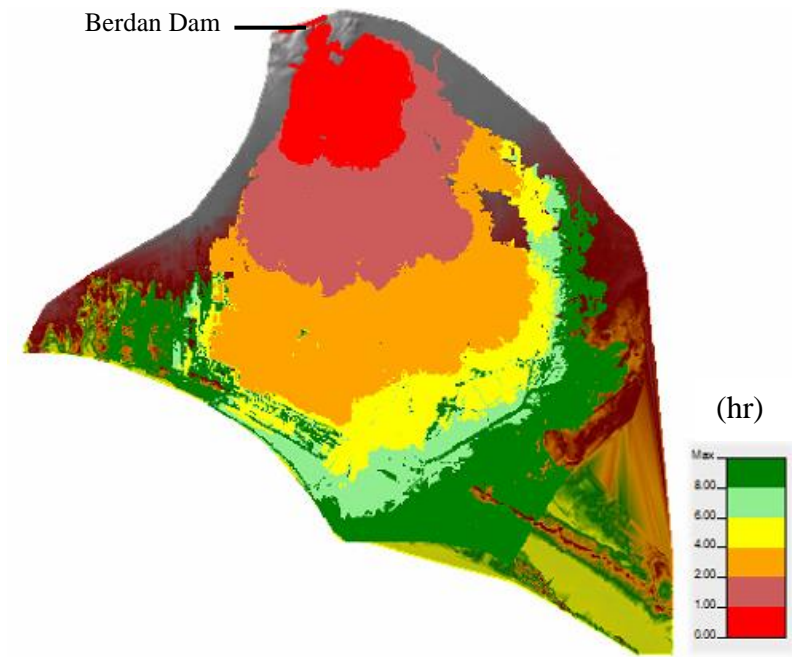


Figure 4.37. Distribution of flood arrival time for initial water elevation of 72 m with 1.20*base n

4.3.4. Flood Inundation for Initial Water Level of 72 m with $n=0.060$

Distributions of maximum depth, maximum water surface elevation, maximum velocity and flood arrival time for the initial reservoir water level of 72 m with $n=0.060$ were given in Figures 4.38 through 4.41.

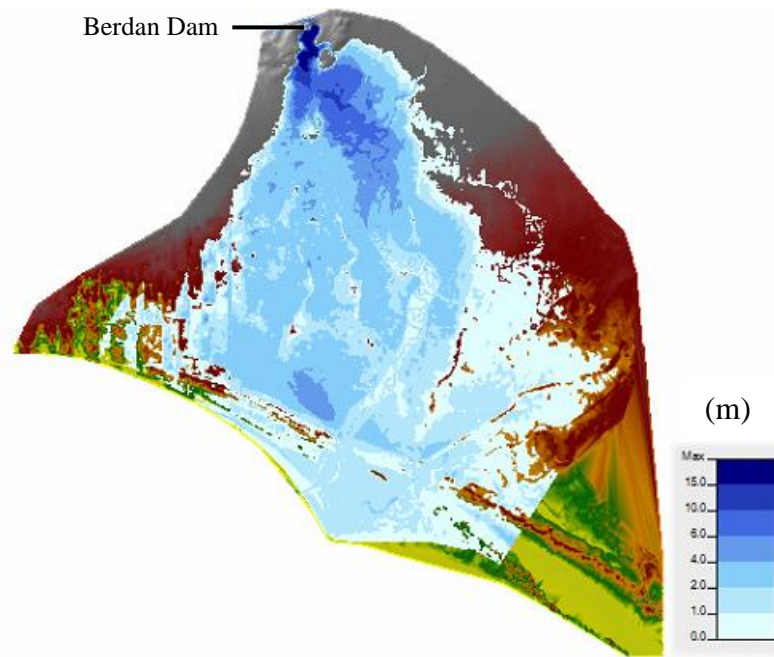


Figure 4.38. Distribution of maximum depth for initial water elevation of 72 m with $n=0.060$

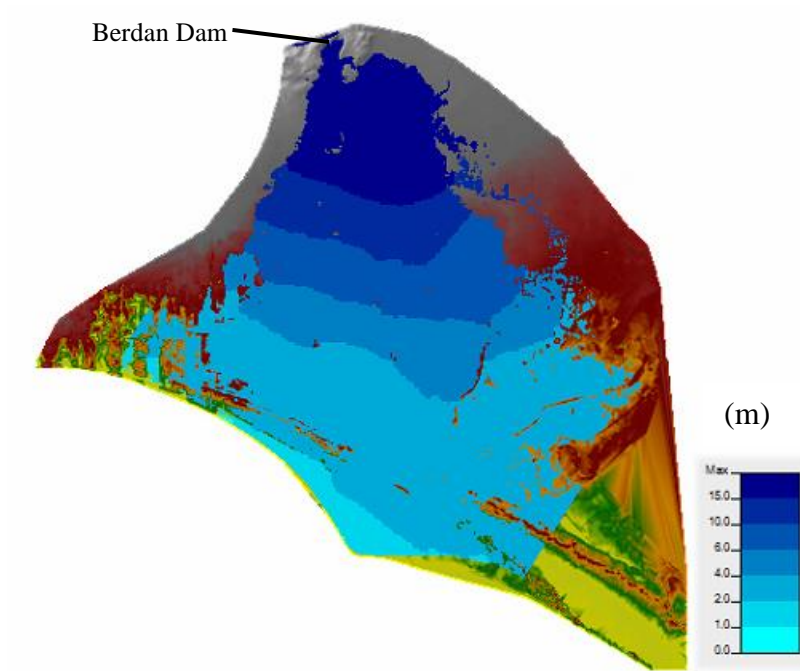


Figure 4.39. Distribution of maximum water surface elevation for initial water elevation of 72 m with $n=0.060$

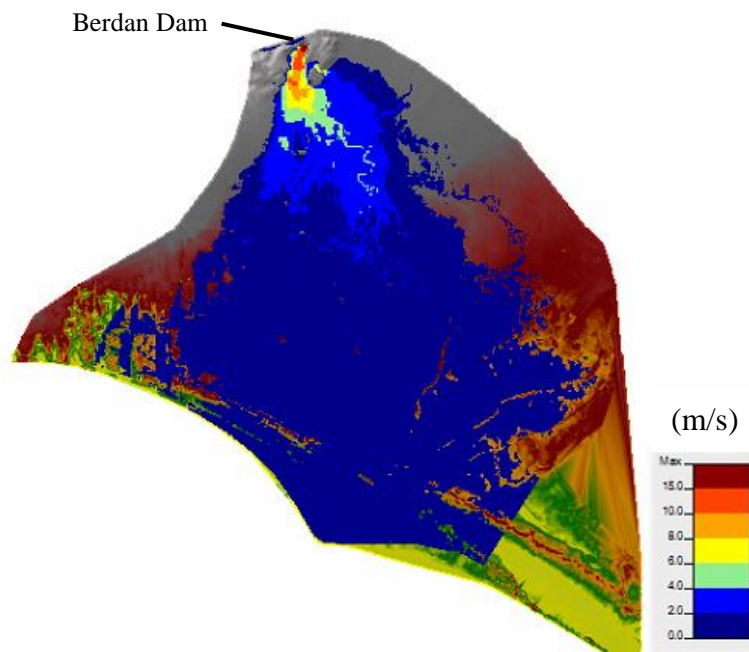


Figure 4.40. Distribution of maximum velocity for initial water elevation of 72 m with $n=0.060$

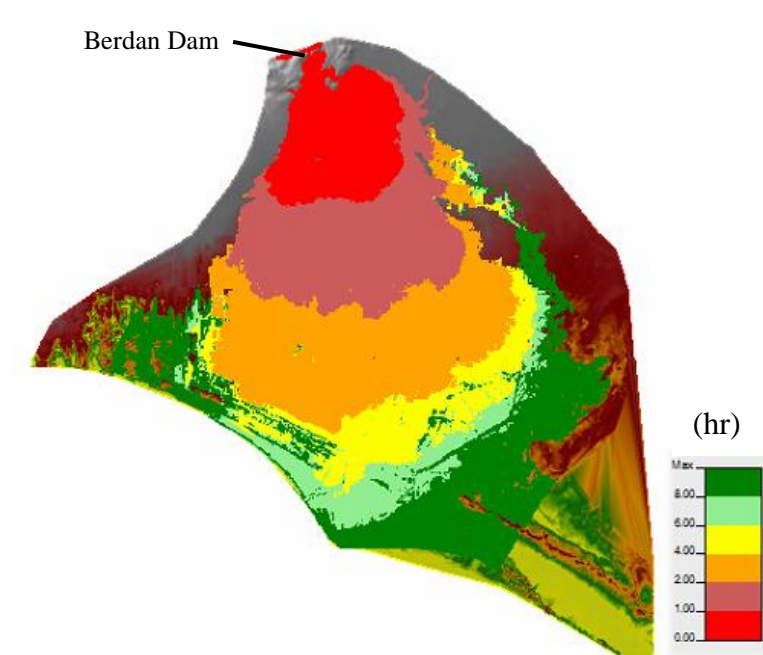


Figure 4.41. Distribution of maximum velocity for initial water elevation of 72 m with $n=0.060$

Maximum values of depth, velocity, and water surface elevation at cross-section 2500 m away from the dam body with $n=0.060$ and base n are given in Table 4.7 and Table 4.8, respectively.

Table 4.7. Maximum values for different initial water levels with $n=0.060$ at 2500 m away from the dam

| Initial water level (m) | Maximum depth (m) | Maximum velocity (m/s) | Maximum WSE (m) |
|-------------------------|-------------------|------------------------|-----------------|
| 71.6 | 20.36 | 8.98 | 39.55 |
| 71.8 | 20.40 | 9.00 | 39.60 |
| 72.0 | 20.45 | 9.02 | 39.65 |
| 72.2 | 20.49 | 9.02 | 39.68 |
| 72.4 | 20.54 | 8.96 | 39.73 |
| 72.6 | 20.58 | 8.98 | 39.77 |

Table 4.8. Maximum values for different initial water levels with base n at 2500 m away from the dam

| Initial water level (m) | Maximum depth (m) | Maximum velocity (m/s) | Maximum WSE (m) |
|-------------------------|-------------------|------------------------|-----------------|
| 71.6 | 21.28 | 10.67 | 40.45 |
| 71.8 | 21.33 | 10.70 | 40.50 |
| 72.0 | 21.38 | 10.73 | 40.54 |
| 72.2 | 21.42 | 10.76 | 40.59 |
| 72.4 | 21.47 | 10.79 | 40.64 |
| 72.6 | 21.51 | 10.82 | 40.68 |

Maximum values of depth, velocity, and water surface elevation at cross-section 3500 m away from the dam body with $n=0.060$ and base n are given in Table 4.9 and Table 4.10, respectively.

Table 4.9. Maximum values for different initial water levels with $n=0.060$ at 3500 m away from the dam

| Initial water level (m) | Maximum depth (m) | Maximum velocity (m/s) | Maximum WSE (m) |
|-------------------------|-------------------|------------------------|-----------------|
| 71.6 | 17.10 | 6.55 | 31.45 |
| 71.8 | 17.15 | 6.56 | 31.48 |
| 72.0 | 17.19 | 6.57 | 31.52 |
| 72.2 | 17.22 | 6.50 | 31.55 |
| 72.4 | 17.28 | 6.53 | 31.59 |
| 72.6 | 17.33 | 6.50 | 31.63 |

Table 4.10. Maximum values for different initial water levels with base n at 3500 m away from the dam

| Initial water level (m) | Maximum depth (m) | Maximum velocity (m/s) | Maximum WSE (m) |
|-------------------------|-------------------|------------------------|-----------------|
| 71.6 | 17.18 | 9.26 | 33.13 |
| 71.8 | 17.24 | 9.27 | 33.17 |
| 72.0 | 17.29 | 9.29 | 33.21 |
| 72.2 | 17.34 | 9.30 | 33.25 |
| 72.4 | 17.38 | 9.31 | 33.28 |
| 72.6 | 17.43 | 9.32 | 33.32 |

Maximum values of depth, velocity, and water surface elevation at cross-section 5000 m away from the dam body with $n=0.060$ and base n are given in Table 4.11 and Table 4.12, respectively.

Table 4.11. Maximum values for different initial water levels with $n=0.060$ at 5000 m away from the dam

| Initial water level (m) | Maximum depth (m) | Maximum velocity (m/s) | Maximum WSE (m) |
|-------------------------|-------------------|------------------------|-----------------|
| 71.6 | 14.96 | 4.63 | 23.93 |
| 71.8 | 15.01 | 4.65 | 23.98 |
| 72.0 | 15.05 | 4.65 | 24.03 |
| 72.2 | 15.08 | 4.60 | 24.06 |
| 72.4 | 15.14 | 4.63 | 24.12 |
| 72.6 | 15.19 | 4.58 | 24.17 |

Table 4.12. Maximum values for different initial water levels with base n at 5000 m away from the dam

| Initial water level (m) | Maximum depth (m) | Maximum velocity (m/s) | Maximum WSE (m) |
|-------------------------|-------------------|------------------------|-----------------|
| 71.6 | 15.45 | 5.26 | 24.45 |
| 71.8 | 15.51 | 5.29 | 24.51 |
| 72.0 | 15.55 | 5.30 | 24.56 |
| 72.2 | 15.60 | 5.31 | 24.61 |
| 72.4 | 15.65 | 5.32 | 24.65 |
| 72.6 | 15.70 | 5.32 | 24.70 |

For the initial reservoir water level of 72 m, the results of the analyses are given in Table 4.13 through 4.15 with varying Manning's roughness values at cross-sections which are 2500 m, 3500 m, and 5000 m away from the dam body.

Table 4.13. Comparison of maximum depths for overtopping

| n values | Maximum depth at 2500 m away | Maximum depth at 3500 m away | Maximum depth at 5000 m away |
|--------------|------------------------------|------------------------------|------------------------------|
| 0.80* base n | 20.28 | 16.68 | 15.26 |
| base n | 21.38 | 17.29 | 15.55 |
| 1.20*base n | 21.99 | 17.64 | 15.73 |
| n=0.060 | 20.45 | 17.19 | 15.05 |

Table 4.14. Comparison of maximum WSE values for overtopping

| n values | Maximum WSE at 2500 m away | Maximum WSE at 3500 m away | Maximum WSE at 5000 m away |
|--------------|----------------------------|----------------------------|----------------------------|
| 0.80* base n | 39.43 | 32.51 | 24.23 |
| base n | 40.54 | 33.21 | 24.56 |
| 1.20*base n | 41.17 | 33.61 | 24.75 |
| n=0.060 | 39.65 | 31.52 | 24.03 |

Table 4.15. Comparison of maximum velocities for overtopping

| n values | Maximum velocity at 2500 m away | Maximum velocity at 3500 m away | Maximum velocity at 5000 m away |
|--------------|---------------------------------|---------------------------------|---------------------------------|
| 0.80* base n | 12.36 | 11.02 | 5.90 |
| base n | 10.73 | 9.29 | 5.30 |
| 1.20*base n | 9.36 | 7.98 | 4.85 |
| n=0.060 | 9.02 | 6.57 | 4.65 |

The maximum values were mostly observed for the initial reservoir water level of 72 m. Therefore, the analyses with different Manning's roughness coefficient values were performed with this level.

According to the results of analyses for overtopping mode of failure, it was determined that the water depth and water surface elevation increases, while the velocity of water and flood arrival time decreases with increasing Manning's roughness coefficient values as in the case of piping failure.

4.4. Comparison of the Results for Settlement Area

In addition to Chapter 4.2. and Chapter 4.3., the results of the analyses were examined further at the cross-section which is 3500 m away from dam considering the average distance of the settlement area to the dam body since it is required to determine the maximum depth of water at the regions where the buildings are located for a dam break scenario.

However, the maximum values of water depth were observed at the station of 1026 m, where the bottom of the main river channel is located, on the cross-section 3500 m away from the dam. Therefore, the maximum water depth in the residential area was reevaluated according to the location of settlement by using terrain elevation and maximum water surface elevation.

The location of the residential area on the cross-section 3500 m away from the dam is shown in Figure 4.42.

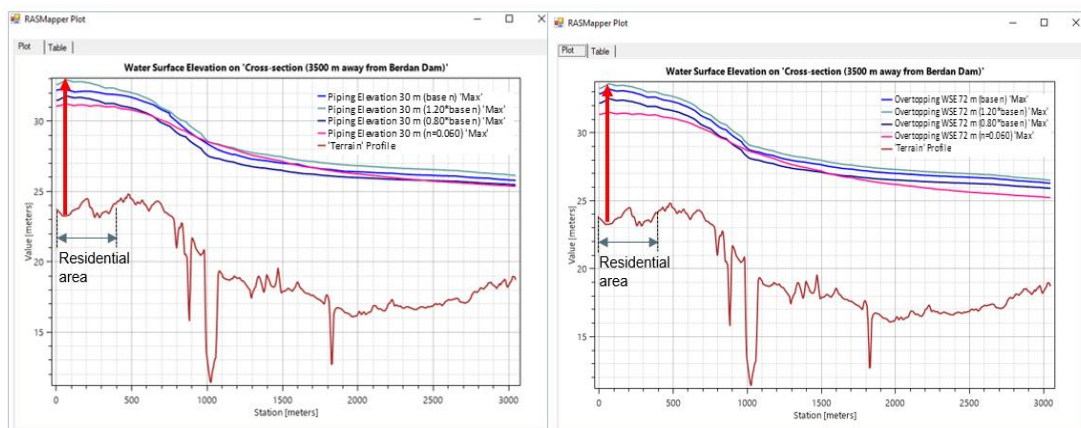


Figure 4.42. Distributions of maximum water surface elevation for piping and overtopping modes of failure

The terrain elevation corresponding to the maximum water surface elevation was determined to be 23.27 m. For the residential area, the comparison of maximum depths of water at this terrain elevation for piping and overtopping is shown in Table 4.16.

Table 4.16. Comparison of maximum depths for piping and overtopping in the residential area

| n values | Maximum depth for piping at 3500 m away from the dam (m) | Maximum depth for overtopping at 3500 m away from the dam (m) |
|--------------|--|---|
| 0.80* base n | 8.51 | 9.23 |
| base n | 8.94 | 9.94 |
| 1.20*base n | 9.66 | 10.34 |
| n=0.060 | 7.97 | 8.25 |

Maximum depth values were found to be slightly greater for the overtopping mode of failure than the piping mode of failure in the residential area on the cross-section 3500 m away from the dam.

In addition, greater values of maximum depth and velocity were observed to be spread over a wider area for overtopping mode of failure than the piping mode of failure according to the flood inundation maps. Therefore, it can be said that the effect of dam break was more pronounced for the overtopping mode of failure.

Moreover, in this study analyses were completed with the assumption of clear water. In real situations, transported materials due to dam break should be considered. If sediment transportation was taken into account, water surface elevation values would be higher.

CHAPTER 5

CONCLUSIONS

5.1. Results of the Analyses

After all geometric, hydrologic and hydraulic inputs were entered in HEC-RAS, property tables were computed on the 2D flow area in RAS-Mapper to associate 2D flow area to the terrain. Finally, the dam break analyses were carried out by using hydrodynamic models in HEC-RAS. The results of the analyses were viewed from the output maps which were visualized on the digital elevation model with the help of RAS-Mapper in terms of water surface elevation, velocity, and depth of water, and flood arrival time.

The settlement area of Tarsus is located approximately 5000 m away from Berdan Dam. The nearest distance from the dam body to the settlement area is approximately 2500 m. Hence, it is expected that the settlement area is affected by the maximum possible flood severely since it is close to the dam body.

The maximum velocity of water was found to be 12.36 m/s in 2500 m away from the dam body. In addition, the average maximum velocity was found to be greater than 1.5 m/s in the settlement area. Thus, the flood wave may cause severe damages in this region since it is beyond the tolerable limit when considered together with the maximum depth of water and transported material in the flow area. The average value of velocity values was observed to be decreasing from upstream to downstream of the terrain which means that there will be less risk in the far downstream of floodplain due to the factors that are caused by velocity like drag, accumulation, and erosion of materials.

The maximum depth of water was observed to be 21.99 m at approximately 2500 m away from the dam body. The depth of water was found to be decreasing from

upstream to downstream of the flow area as expected, yet the water depth value remains over 2 meters on a very wide area in the terrain. Furthermore, prolonged exposure to high depths of water may lead to even worse damages during catastrophic floods.

The maximum water surface elevation was found as 72.6 m at the dam body since it was determined as the initial condition at reservoir volume. The maximum water surface elevation was found to be 41.17 m in 2500 m away from the dam body.

Froehlich (2008) formulation identified the breach formation time as 1.19 hours. Therefore, the breach formation time of Berdan Dam is 1.19 hours. However, it is crucial to determine the arrival time of the flood. In addition, the distribution of maximum flood arrival time in terrain was displayed for each scenario. It was determined that the maximum flood reached the settlement center of Tarsus in between half an hour to forty minutes.

Probable damages should be determined according to these values which were obtained from dam break analyses. When dam break analysis is evaluated by considering only the loss of human life, the determination of population in settlement centers and preparation of evacuation plans for that population should be the first step in establishing emergency action plans. According to the 2018 data which was obtained from TÜİK, the population of Tarsus settlement is 339.676. This is the minimum number of potentially affected people under the risk of a probable dam break. However, this number is thought to be even much higher considering the recent migration the region has received.

All in all, Tarsus settlement, which is close to Berdan Dam, has a high risk of inundation. Measures should be taken according to the flood arrival time, maximum depth and maximum velocity of water in terrain. With the preparation of emergency action plans by the authorities in charge of public safety, the loss of life can be prevented in the event of a probable flood on this scale.

5.2. Recommendations for Future Works

Performing the risk analyses of the region may be helpful for insurance companies in establishing more concrete risk balance sheets and preparing more realistic emergency action plans. In addition, similar dam break analyses should be performed for other regions that are under flood risk due to probable dam break.

REFERENCES

- Ackerman, C. T., & Brunner, G. W. (2008). Dam Failure Analysis Using HEC-RAS and HEC-GeoRAS. *World Environmental and Water Resources Congress 2008: Ahupua'a*, 8.
- Alonso, R., Santillana, M., & Dawson, C. (2008). On the diffusive wave approximation of the shallow water equations. *European Journal of Applied Mathematics*, 19(5), 575–606. <https://doi.org/10.1017/s0956792508007675>
- Altınakar, M. S., Mcgrath, M. Z., Ramalingam, V. P., & Omari, H. (2010). 2D Modeling of Big Bay Dam Failure in Mississippi: Comparison with Field Data and 1D Model Results. In A. Dittrich, K. Koll, J. Aberle, & P. Geisenhainer (Eds.), *International Conference on Fluvial Hydraulics - Riverflow 2010* (pp. 547–554). Retrieved from <https://hdl.handle.net/20.500.11970/105454>
- Amini, A., Arya, A., Eghbalzadeh, A., & Javan, M. (2017). Peak flood estimation under overtopping and piping conditions at Vahdat Dam, Kurdistan Iran. *Arabian Journal of Geosciences*, 10(6), 1–11. <https://doi.org/10.1007/s12517-017-2854-y>
- Barnes, H. H. (1967). *Roughness Characteristics of Natural Channels*. <https://doi.org/10.1007/s132-002-8284-1>
- Basheer, T. A., Wayayok, A., Yusuf, B., & Kamal, M. D. R. (2017). Dam breach parameters and their influence on flood hydrographs for Mosul Dam. *Journal of Engineering Science and Technology*, 12(11), 2896–2908.
- Bates, P. D., Anderson, M. G., Baird, L., Walling, D. E., & Simm, D. (1992). Modelling Floodplain Flows Using a Two-Dimensional Finite Element Model. *Earth Surface Processes and Landforms*, 17(6), 575–588. <https://doi.org/10.1002/esp.3290170604>
- Bozkuş, Z. (2003). Pre-Event Failure Analyses of Kestel Dam for Disaster Management. *Journal of Physical and Engineering Science*, 53, 58–64.
- Bozkuş, Z., & Bağ, F. (2011). Virtual Failure Analysis of the Çınarcık Dam. *Teknik Dergi/Technical Journal of Turkish Chamber of Civil Engineers*, 22, 5675–5688.
- Bozkuş, Z., & Güner, A. İ. (2001). Pre-Event Dam Failure Analyses for Emergency Management Pre-Event Dam Failure Analyses for Emergency Management. *Turkish Journal of Engineering and Environmental Science*, 25, 627–641.
- Bozkuş, Z., & Kasap, A. (1998). Comparison of Physical and Numerical Dam-Break Simulations. *Turkish Journal of Engineering and Environmental Science*, 429–443.

- Brunner, G. W. (2016a). *HEC-RAS River Analysis System 2D Modeling User's Manual* (Vol. 5). Davis, CA.
- Brunner, G. W. (2016b). *Hydraulic Reference Manual Version 5.0*. Davis, CA.
- Brunner, G. W., Piper, S. S., Jensen, M. R., & Chacon, B. (2015). Combined 1D and 2D Hydraulic Modeling within HEC-RAS. *World Environmental and Water Resources Congress 2015*, 1432–1443. <https://doi.org/10.1061/9780784479162.141>
- Casulli, V. (2009). A high-resolution wetting and drying algorithm for free-surface hydrodynamics. *International Journal for Numerical Methods in Fluids*, 60(4), 391–408. <https://doi.org/10.1002/flid.1896>
- Chow, V. T. (1959). *Open Channel Hydraulics* (H. E. Davis, ed.). New York: McGraw-Hill Book Company.
- Collier, N., Radwan, H., Dalcin, L., & Calo, V. M. (2013). Time adaptivity in the diffusive wave approximation to the shallow water equations. *Journal of Computational Science*, 4(3), 152–156. <https://doi.org/10.1016/j.jocs.2011.07.004>
- Derdous, O., Djemili, L., Bouchehed, H., & Tachi, S. E. (2015). *A GIS based approach for the prediction of the dam break flood hazard – A case study of Zardezas reservoir “ Skikda , Algeria .”* <https://doi.org/10.1515/jwld-2015-0020>
- Froehlich, D. C. (2008). Embankment Dam Breach Parameters and Their Uncertainties. *Journal of Hydraulic Engineering*. [https://doi.org/10.1061/\(asce\)0733-9429\(2008\)134:12\(1708\)](https://doi.org/10.1061/(asce)0733-9429(2008)134:12(1708))
- Gharbi, M., Soualmia, A., Dartus, D., & Masbernat, L. (2016). Floods effects on rivers morphological changes application to the Medjerda River in Tunisia. *Journal of Hydrology and Hydromechanics*. <https://doi.org/10.1515/johh-2016-0004>
- Gogoaşe, D. E., Popovici, D. A. G., Savin, B. A. C., & Armaş, I. (2016). *GIS for Dam-Break Flooding . Study Area : 253–280*. <https://doi.org/10.1007/978-3-319-24942-1>
- Goodell, C., & Wahlin, B. (2009). *Dynamic and Level Pool Reservoir Drawdown-A Practical Comparison for Dam Breach Modeling*.
- Haltas, I., Tayfur, G., & Elci, S. (2016). Two-dimensional numerical modeling of flood wave propagation in an urban area due to Ürkmez dam-break, İzmir, Turkey. *Natural Hazards*. <https://doi.org/10.1007/s11069-016-2175-6>
- Hirsch, C. (2007). *Numerical Computation of Internal and External Flows* (2nd ed.). <https://doi.org/10.1016/b978-0-7506-6594-0.x5037-1>

- Horritt, M. S., & Bates, P. D. (2002). Evaluation of 1D and 2D numerical models for predicting river flood inundation. *Journal of Hydrology*, 268, 87–99. Retrieved from www.elsevier.com/locate/jhydrol
- Joshi, M. M., & Shahapure, S. S. (2017). Two Dimensional Dam Break Flow Study Using HEC-RAS for Ujjani Dam. *International Journal of Engineering and Technology*, 9(4), 2923–2928. <https://doi.org/10.21817/ijet/2017/v9i4/170904032>
- MacDonald, T. C., & Langridge-Monopolis, J. (1984). Breaching Characteristics of Dam Failures. *Journal of Hydraulic Engineering*, 110(5), 567–586. [https://doi.org/10.1061/\(asce\)0733-9429\(1984\)110:5\(567\)](https://doi.org/10.1061/(asce)0733-9429(1984)110:5(567))
- Mazumder, S. (2016). *Numerical Methods for Partial Differential Equations: Finite Difference and Finite Volume Methods*. Elsevier Inc.
- Muchard, S., & Deo, S. (2012). *Dam Breach Modeling with Unsteady HEC-RAS: Common Techniques and Assumptions Compared Background – Dam Safety in Texas*. 1383–1398.
- Neelz, S., & Pender, G. (2009). *Desktop Review of 2D Hydraulic Modelling Packages*.
- Nguyen, S., & Weston, D. (2013). *Dam Break for the Dalles Dam*. 1687–1697. <https://doi.org/10.1061/9780784412947.166>
- Norris, S. E. (2000). *A Parallel Navier-Stokes Solver for Natural Convection and Free Surface Flow*. University of Sydney.
- Qi, H., & Altinakar, M. S. (2012). GIS-Based Decision Support System for Dam Break Flood Management under Uncertainty with Two-Dimensional Numerical Simulations. *Journal of Water Resources Planning and Management*. [https://doi.org/10.1061/\(ASCE\)WR.1943-5452.0000192](https://doi.org/10.1061/(ASCE)WR.1943-5452.0000192)
- Şahin, A. N. (2016). *Performance of FLO-2D Software on Flood Inundation Analysis (Middle East Technical University)*. Retrieved from <http://etd.lib.metu.edu.tr/upload/12620513/index.pdf>
- Sehili, A., Lang, G., & Lippert, C. (2014). High-resolution subgrid models: Background, grid generation, and implementation. *Ocean Dynamics*, 64(4), 519–535. <https://doi.org/10.1007/s10236-014-0693-x>
- Sharma, P. (2017). Dam Break Analysis Using HEC-RAS and HEC-GeoRAS – A Case Study of Ajwa Reservoir. *Journal of Water Resources and Ocean Science*, 5(6), 108. <https://doi.org/10.11648/j.wros.20160506.15>
- Soulis, J. V. (1992). Computation of two-dimensional dam-break flood flows. *International Journal for Numerical Methods in Fluids*, 14(6), 631–664. <https://doi.org/10.1002/flid.1650140602>

- Türkiye İstatistik Kurumu. (2018). Retrieved June 25, 2019, from <https://biruni.tuik.gov.tr/medas/?kn=95&locale=tr>
- Versteeg, H. K., & Malalasekera, W. (1995). *An Introduction To Computational Fluid Dynamics*. Longman.
- Von Thun, J. L., & Gillette, D. R. (1990). *Guidance on Breach Parameters*. Denver, Colorado: U.S. Bureau of Reclamation.
- Vreugdenhil, C. B. (1994). *Numerical Methods for Shallow-Water Flow* (1st ed.). <https://doi.org/10.1007/978-94-015-8354-1>
- Wahl, T. L. (1998). *Prediction of Embankment Dam Breach Parameters*.
- Wahl, T. L. (2004). Uncertainty of Predictions of Embankment Dam Breach Parameters. *Journal of Hydraulic Engineering*. [https://doi.org/10.1061/\(ASCE\)0733-9429\(2004\)130:5\(389\)](https://doi.org/10.1061/(ASCE)0733-9429(2004)130:5(389))
- Wahl, T. L. (2010). Dam Breach Modeling-An Overview of Analysis Methods. *2nd Joint Federal Interagency Conference, Las Vegas, NV, June 27 - July 1, 2010*. Denver, CO.
- Xiong, Y. (2011). A Dam Break Analysis Using HEC-RAS. *Journal of Water Resource and Protection*. <https://doi.org/10.4236/jwarp.2011.36047>
- Xu, Y., & Zhang, L. M. (2009). Breaching Parameters for Earth and Rockfill Dams. *Journal of Geotechnical and Geoenvironmental Engineering*. [https://doi.org/10.1061/\(asce\)gt.1943-5606.0000162](https://doi.org/10.1061/(asce)gt.1943-5606.0000162)

APPENDICES

A. Details of Inputs of the Analyses

Unsteady Flow Data - Unsteady Flow

File Options Help

Boundary Conditions Initial Conditions Apply Data

Boundary Condition Types

| | | | |
|--------------------|-----------------------|------------------------|-----------------------|
| Stage Hydrograph | Flow Hydrograph | Stage/Flow Hydr. | Rating Curve |
| Normal Depth | Lateral Inflow Hydr. | Uniform Lateral Inflow | Groundwater Interflow |
| T.S. Gate Openings | Elev Controlled Gates | Navigation Dams | IB Stage/Flow |
| Rules | Precipitation | | |

Add Boundary Condition Location

Add RS ... Add SA/2D Flow Area ... Add SA Connection ... Add Pump Station ...

Select Location in table then select Boundary Condition Type

| River | Reach | RS | Boundary Condition |
|-------|-------|----|--------------------|
| | | | |
| | | | |

Storage/2D Flow Areas

| | Boundary Condition |
|------------------------------|----------------------|
| 1 2DFlowArea BCLine: Outflow | Normal Depth |
| 2 Berdan Reservoir | Lateral Inflow Hydr. |

Figure A.1. Unsteady flow data

Table A.1. Inflow and outflow hydrograph of Berdan Dam

| T (hour) | Q_{in} (m³/s) | Water Level at Reservoir (m) | Q_{out} (m³/s) |
|-----------------|---|-------------------------------------|--|
| 0.0 | 95.20 | 56.000 | 0.00 |
| 1.0 | 111.04 | 56.050 | 0.92 |
| 2.0 | 162.05 | 56.117 | 3.24 |
| 3.0 | 252.92 | 56.216 | 8.19 |
| 4.0 | 398.61 | 56.370 | 18.42 |
| 5.0 | 607.48 | 56.603 | 38.61 |
| 6.0 | 891.43 | 56.944 | 76.15 |
| 7.0 | 1244.69 | 57.416 | 141.37 |
| 8.0 | 1667.85 | 58.037 | 247.08 |
| 9.0 | 2139.39 | 58.813 | 406.81 |
| 10.0 | 2626.33 | 59.731 | 630.89 |
| 11.0 | 3114.62 | 60.609 | 877.63 |
| 12.0 | 3575.25 | 61.511 | 1161.32 |
| 13.0 | 3998.26 | 62.465 | 1492.14 |
| 14.0 | 4364.69 | 63.437 | 1859.21 |
| 15.0 | 4666.66 | 64.392 | 2247.38 |
| 16.0 | 4908.27 | 65.302 | 2640.37 |
| 17.0 | 5094.45 | 66.143 | 3023.32 |
| 18.0 | 5230.79 | 66.903 | 3384.00 |
| 19.0 | 5347.54 | 67.578 | 3715.48 |
| 20.0 | 5360.00 | 68.157 | 4007.87 |
| 21.0 | 5344.31 | 68.631 | 4252.63 |
| 22.0 | 5273.16 | 69.002 | 4447.89 |
| 23.0 | 5186.18 | 69.277 | 4594.07 |
| 24.0 | 5068.70 | 69.465 | 4694.58 |
| 25.0 | 4934.00 | 69.573 | 4752.69 |
| 26.0 | 4780.88 | 69.609 | 4772.59 |
| 27.0 | 4613.65 | 69.583 | 4758.30 |
| 28.0 | 4430.27 | 69.500 | 4713.53 |
| 29.0 | 4241.42 | 69.367 | 4642.22 |
| 30.0 | 4034.60 | 69.190 | 4547.50 |
| 31.0 | 3826.16 | 68.973 | 4432.35 |
| 32.0 | 3601.81 | 68.720 | 4299.37 |
| 33.0 | 3377.39 | 68.435 | 4150.91 |
| 34.0 | 3153.04 | 68.122 | 3990.31 |
| 35.0 | 2932.47 | 67.788 | 3820.60 |
| 36.0 | 2721.09 | 67.436 | 3645.00 |
| 37.0 | 2518.43 | 67.073 | 3466.49 |

Table A.1. Inflow and outflow hydrograph of Berdan Dam (continued)

| T (hour) | Q_{in} (m³/s) | Water Level at Reservoir (m) | Q_{out} (m³/s) |
|-----------------|---|-------------------------------------|--|
| 38.0 | 2328.54 | 66.703 | 3287.72 |
| 39.0 | 2155.98 | 66.332 | 3111.49 |
| 40.0 | 1996.32 | 65.963 | 2939.97 |
| 41.0 | 1852.99 | 65.601 | 2774.76 |
| 42.0 | 1721.37 | 65.249 | 2617.01 |
| 43.0 | 1603.86 | 64.908 | 2467.39 |
| 44.0 | 1498.33 | 64.580 | 2326.45 |
| 45.0 | 1404.46 | 64.266 | 2194.40 |
| 46.0 | 1320.84 | 63.967 | 2071.25 |
| 47.0 | 1246.54 | 63.684 | 1956.82 |
| 48.0 | 1178.59 | 63.415 | 1850.70 |
| 49.0 | 1118.29 | 63.162 | 1752.39 |
| 50.0 | 1061.91 | 62.923 | 1661.34 |
| 51.0 | 1013.08 | 62.697 | 1577.10 |
| 52.0 | 968.00 | 62.485 | 1499.24 |
| 53.0 | 928.49 | 62.285 | 1427.35 |
| 54.0 | 892.33 | 62.097 | 1361.01 |
| 55.0 | 844.98 | 61.918 | 1298.83 |
| 56.0 | 817.52 | 61.748 | 1240.72 |
| 57.0 | 778.91 | 61.587 | 1186.59 |
| 58.0 | 757.66 | 61.434 | 1136.18 |
| 59.0 | 728.59 | 61.291 | 1089.52 |
| 60.0 | 711.92 | 61.156 | 1046.30 |
| 61.0 | 688.58 | 61.030 | 1006.36 |
| 62.0 | 675.40 | 60.911 | 969.38 |
| 63.0 | 655.21 | 60.799 | 935.16 |
| 64.0 | 644.86 | 60.695 | 903.47 |
| 65.0 | 628.29 | 60.597 | 874.16 |
| 66.0 | 620.27 | 60.505 | 847.02 |
| 67.0 | 607.15 | 60.419 | 821.96 |
| 68.0 | 601.16 | 60.339 | 798.81 |
| 69.0 | 590.59 | 60.265 | 777.44 |
| 70.0 | 585.63 | 60.195 | 757.70 |
| 71.0 | 577.40 | 60.130 | 739.49 |
| 72.0 | 573.22 | 60.070 | 722.66 |
| 73.0 | 565.74 | 60.014 | 707.08 |
| 74.0 | 562.35 | 59.951 | 689.96 |
| 75.0 | 552.56 | 59.890 | 673.37 |

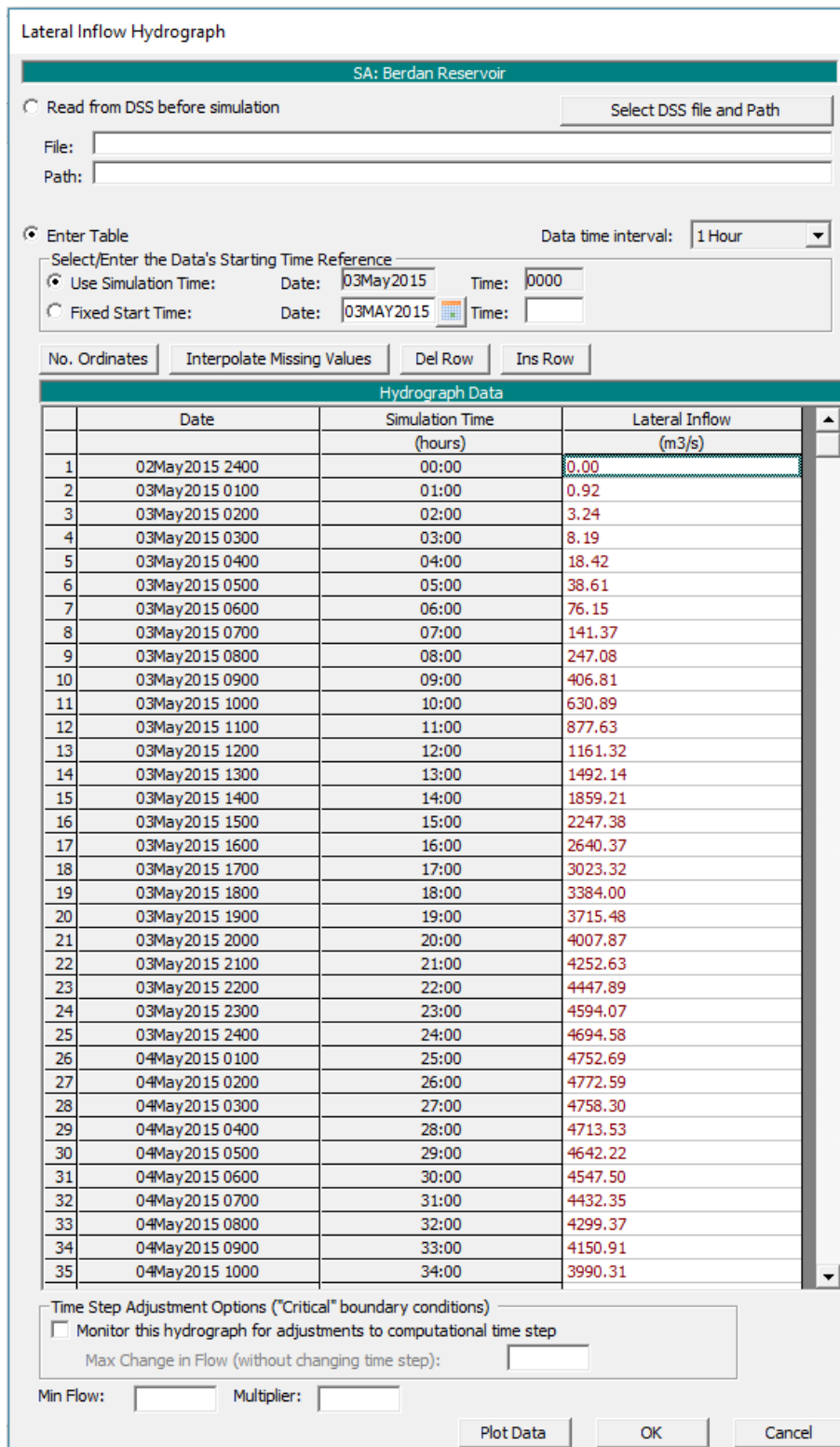


Figure A.2 . Outflow hydrograph

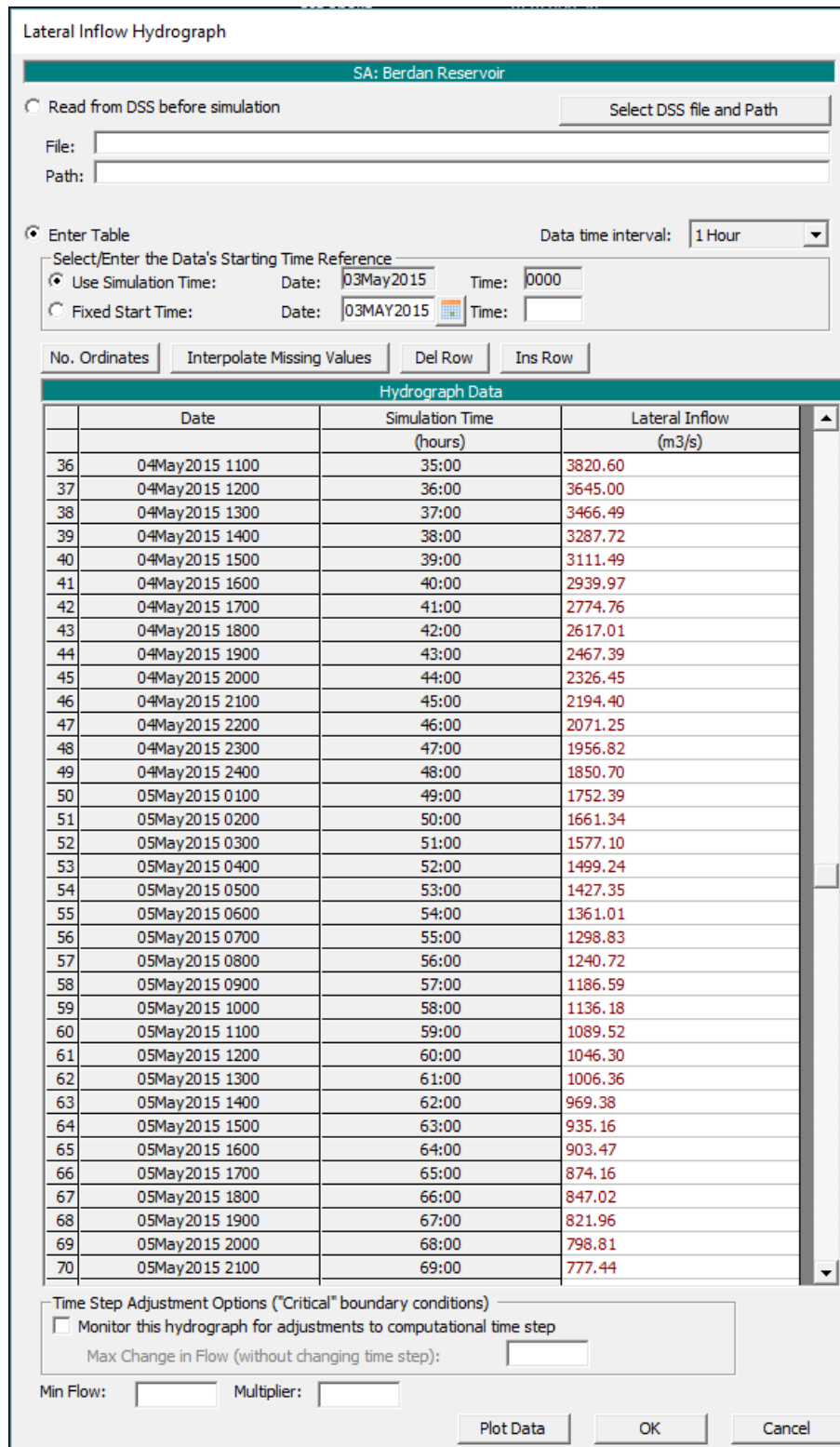


Figure A.2. Outflow hydrograph (continued)

Lateral Inflow Hydrograph

SA: Berdan Reservoir

Read from DSS before simulation Select DSS file and Path

File:

Path:

Enter Table Data time interval: 1 Hour

Select/Enter the Data's Starting Time Reference

Use Simulation Time: Date: 03May2015 Time: 0000

Fixed Start Time: Date: 03MAY2015 Time:

No. Ordinates

| Hydrograph Data | | | |
|-----------------|----------------|----------------------------|--------------------------|
| | Date | Simulation Time (hours) | Lateral Inflow (m3/s) |
| 66 | 05May2015 1700 | 65:00 | 874.16 |
| 67 | 05May2015 1800 | 66:00 | 847.02 |
| 68 | 05May2015 1900 | 67:00 | 821.96 |
| 69 | 05May2015 2000 | 68:00 | 798.81 |
| 70 | 05May2015 2100 | 69:00 | 777.44 |
| 71 | 05May2015 2200 | 70:00 | 757.70 |
| 72 | 05May2015 2300 | 71:00 | 739.49 |
| 73 | 05May2015 2400 | 72:00 | 722.66 |
| 74 | 06May2015 0100 | 73:00 | 707.08 |
| 75 | 06May2015 0200 | 74:00 | 689.96 |
| 76 | 06May2015 0300 | 75:00 | 673.37 |
| 77 | 06May2015 0400 | 76:00 | |
| 78 | 06May2015 0500 | 77:00 | |
| 79 | 06May2015 0600 | 78:00 | |
| 80 | 06May2015 0700 | 79:00 | |
| 81 | 06May2015 0800 | 80:00 | |
| 82 | 06May2015 0900 | 81:00 | |
| 83 | 06May2015 1000 | 82:00 | |
| 84 | 06May2015 1100 | 83:00 | |
| 85 | 06May2015 1200 | 84:00 | |
| 86 | 06May2015 1300 | 85:00 | |
| 87 | 06May2015 1400 | 86:00 | |
| 88 | 06May2015 1500 | 87:00 | |
| 89 | 06May2015 1600 | 88:00 | |
| 90 | 06May2015 1700 | 89:00 | |
| 91 | 06May2015 1800 | 90:00 | |
| 92 | 06May2015 1900 | 91:00 | |
| 93 | 06May2015 2000 | 92:00 | |
| 94 | 06May2015 2100 | 93:00 | |
| 95 | 06May2015 2200 | 94:00 | |
| 96 | 06May2015 2300 | 95:00 | |
| 97 | 06May2015 2400 | 96:00 | |
| 98 | 07May2015 0100 | 97:00 | |
| 99 | 07May2015 0200 | 98:00 | |
| 100 | 07May2015 0300 | 99:00 | |

Time Step Adjustment Options ("Critical" boundary conditions)

Monitor this hydrograph for adjustments to computational time step

Max Change in Flow (without changing time step):

Min Flow: Multiplier:

Figure A.2. Outflow hydrograph (continued)

Table A.2. Manning's roughness coefficient values (Chow, 1959)

| Type of Channel and Description | Minimum | Normal | Maximum |
|---|---------|--------|---------|
| 1. Main Channels | | | |
| a. clean, straight, full stage, no rifts or deep pools | 0.025 | 0.030 | 0.033 |
| b. same as above, but more stones and weeds | 0.030 | 0.035 | 0.040 |
| c. clean, winding, some pools and shoals | 0.033 | 0.040 | 0.045 |
| d. same as above, but some weeds and stones | 0.035 | 0.045 | 0.050 |
| e. same as above, lower stages, more ineffective slopes and sections | 0.040 | 0.048 | 0.055 |
| f. same as "d" with more stones | 0.045 | 0.050 | 0.060 |
| g. sluggish reaches, weedy, deep pools | 0.050 | 0.070 | 0.080 |
| h. very weedy reaches, deep pools, or floodways with heavy stand of timber and underbrush | 0.075 | 0.100 | 0.150 |
| 2. Mountain streams, no vegetation in channel, banks usually steep, trees and brush along banks submerged at high stages | | | |
| a. bottom: gravels, cobbles, and few boulders | 0.030 | 0.040 | 0.050 |
| b. bottom: cobbles with large boulders | 0.040 | 0.050 | 0.070 |
| 3. Floodplains | | | |
| a. Pasture, no brush | | | |
| 1. short grass | 0.025 | 0.030 | 0.035 |
| 2. high grass | 0.030 | 0.035 | 0.050 |
| b. Cultivated areas | | | |
| 1. no crop | 0.020 | 0.030 | 0.040 |
| 2. mature row crops | 0.025 | 0.035 | 0.045 |
| 3. mature field crops | 0.030 | 0.040 | 0.050 |
| c. Brush | | | |
| 1. scattered brush, heavy weeds | 0.035 | 0.050 | 0.070 |
| 2. light brush and trees, in winter | 0.035 | 0.050 | 0.060 |
| 3. light brush and trees, in summer | 0.040 | 0.060 | 0.080 |
| 4. medium to dense brush, in winter | 0.045 | 0.070 | 0.110 |
| 5. medium to dense brush, in summer | 0.070 | 0.100 | 0.160 |
| d. Trees | | | |
| 1. dense willows, summer, straight | 0.110 | 0.150 | 0.200 |
| 2. cleared land with tree stumps, no sprouts | 0.030 | 0.040 | 0.050 |
| 3. same as above, but with heavy growth of sprouts | 0.050 | 0.060 | 0.080 |
| 4. heavy stand of timber, a few down trees, little undergrowth, flood stage below branches | 0.080 | 0.100 | 0.120 |
| 5. same as 4. with flood stage reaching branches | 0.100 | 0.120 | 0.160 |

Table A.2. Manning's roughness coefficient values (Chow, 1959) (continued)

| Type of Channel and Description | Minimum | Normal | Maximum |
|---|---------|--------|---------|
| 4. Excavated or Dredged Channels | | | |
| a. Earth, straight, and uniform | | | |
| 1. clean, recently completed | 0.016 | 0.018 | 0.020 |
| 2. clean, after weathering | 0.018 | 0.022 | 0.025 |
| 3. gravel, uniform section, clean | 0.022 | 0.025 | 0.030 |
| 4. with short grass, few weeds | 0.022 | 0.027 | 0.033 |
| b. Earth winding and sluggish | | | |
| 1. no vegetation | 0.023 | 0.025 | 0.030 |
| 2. grass, some weeds | 0.025 | 0.030 | 0.033 |
| 3. dense weeds or aquatic plants in deep channels | 0.030 | 0.035 | 0.040 |
| 4. earth bottom and rubble sides | 0.028 | 0.030 | 0.035 |
| 5. stony bottom and weedy banks | 0.025 | 0.035 | 0.040 |
| 6. cobble bottom and clean sides | 0.030 | 0.040 | 0.050 |
| c. Dragline-excavated or dredged | | | |
| 1. no vegetation | 0.025 | 0.028 | 0.033 |
| 2. light brush on banks | 0.035 | 0.050 | 0.060 |
| d. Rock cuts | | | |
| 1. smooth and uniform | 0.025 | 0.035 | 0.040 |
| 2. jagged and irregular | 0.035 | 0.040 | 0.050 |
| e. Channels not maintained, weeds and brush uncut | | | |
| 1. dense weeds, high as flow depth | 0.050 | 0.080 | 0.120 |
| 2. clean bottom, brush on sides | 0.040 | 0.050 | 0.080 |
| 3. same as above, highest stage of flow | 0.045 | 0.070 | 0.110 |
| 4. dense brush, high stage | 0.080 | 0.100 | 0.140 |
| 5. Lined or Constructed Channels | | | |
| a. Cement | | | |
| 1. neat surface | 0.010 | 0.011 | 0.013 |
| 2. mortar | 0.011 | 0.013 | 0.015 |
| b. Wood | | | |
| 1. planed, untreated | 0.010 | 0.012 | 0.014 |
| 2. planed, creosoted | 0.011 | 0.012 | 0.015 |
| 3. unplaned | 0.011 | 0.013 | 0.015 |
| 4. plank with battens | 0.012 | 0.015 | 0.018 |
| 5. lined with roofing paper | 0.010 | 0.014 | 0.017 |

Table A.2. Manning's roughness coefficient values (Chow, 1959) (continued)

| Type of Channel and Description | Minimum | Normal | Maximum |
|--|---------|--------|---------|
| 4. Excavated or Dredged Channels | | | |
| c. Concrete | | | |
| 1. trowel finish | 0.011 | 0.013 | 0.015 |
| 2. float finish | 0.013 | 0.015 | 0.016 |
| 3. finished, with gravel on bottom | 0.015 | 0.017 | 0.020 |
| 4. unfinished | 0.014 | 0.017 | 0.020 |
| 5. gunite, good section | 0.016 | 0.019 | 0.023 |
| 6. gunite, wavy section | 0.018 | 0.022 | 0.025 |
| 7. on good excavated rock | 0.017 | 0.020 | |
| 8. on irregular excavated rock | 0.022 | 0.027 | |
| d. Concrete bottom float finish with sides of: | | | |
| 1. dressed stone in mortar | 0.015 | 0.017 | 0.020 |
| 2. random stone in mortar | 0.017 | 0.020 | 0.024 |
| 3. cement rubble masonry, plastered | 0.016 | 0.020 | 0.024 |
| 4. cement rubble masonry | 0.020 | 0.025 | 0.030 |
| 5. dry rubble or riprap | 0.020 | 0.030 | 0.035 |
| e. Gravel bottom with sides of: | | | |
| 1. formed concrete | 0.017 | 0.020 | 0.025 |
| 2. random stone mortar | 0.020 | 0.023 | 0.026 |
| 3. dry rubble or riprap | 0.023 | 0.033 | 0.036 |
| f. Brick | | | |
| 1. glazed | 0.011 | 0.013 | 0.015 |
| 2. in cement mortar | 0.012 | 0.015 | 0.018 |
| g. Masonry | | | |
| 1. cemented rubble | 0.017 | 0.025 | 0.030 |
| 2. dry rubble | 0.023 | 0.032 | 0.035 |
| h. Dressed ashlar/stone paving | 0.013 | 0.015 | 0.017 |
| i. Asphalt | | | |
| 1. smooth | 0.013 | 0.013 | |
| 2. rough | 0.016 | 0.016 | |
| j. Vegetal lining | 0.030 | | 0.500 |

B. Results of the Analyses for Different Piping Elevations with Base n

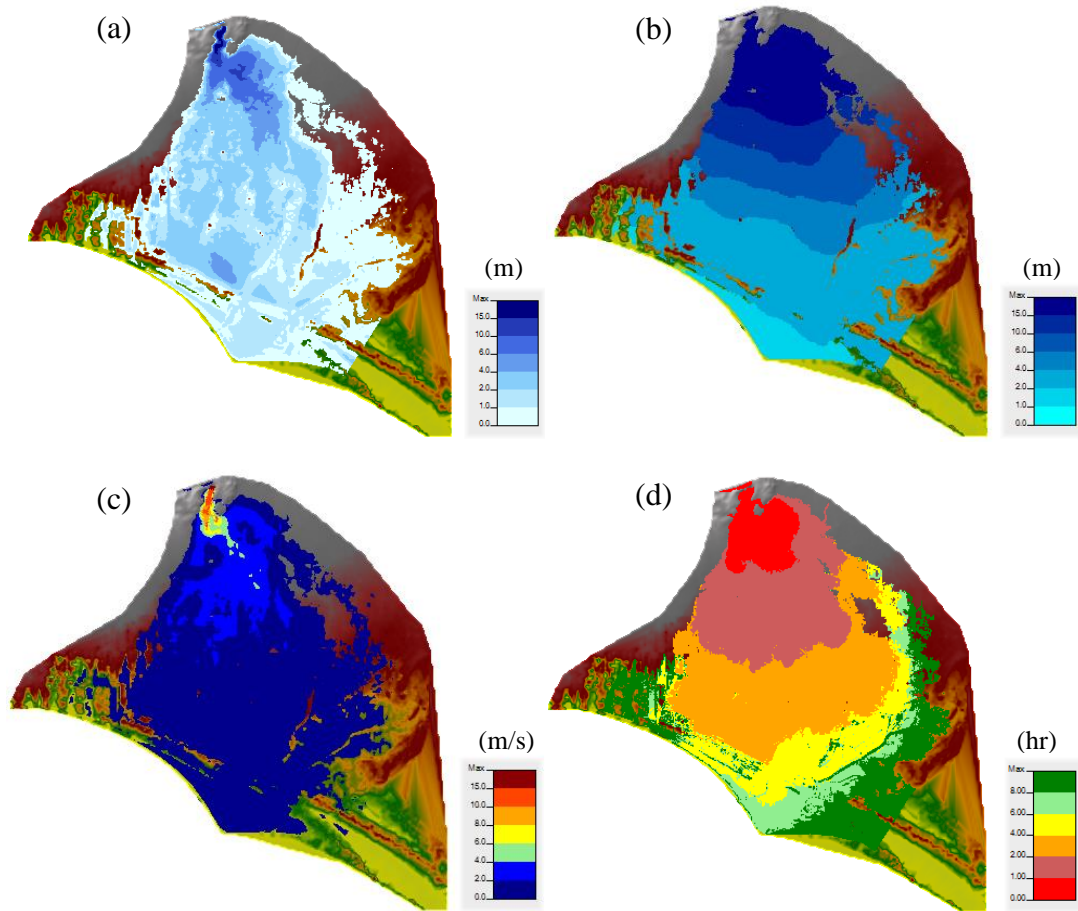


Figure B.1. Distribution of a) maximum depth of water, b) maximum water surface elevation, c) maximum velocity of water and d) flood arrival time for the piping elevation of 10 m with base n

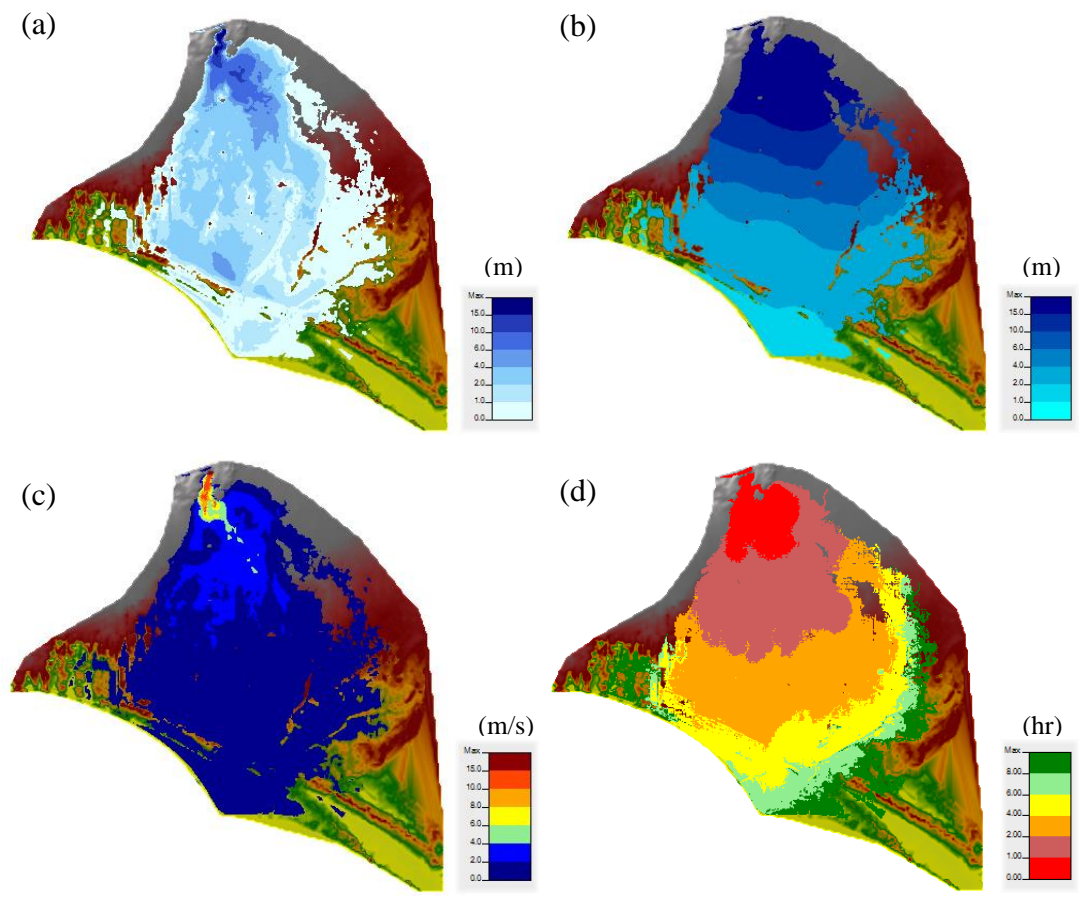


Figure B.2. Distribution of a) maximum depth of water, b) maximum water surface elevation, c) maximum velocity of water and d) flood arrival time for the piping elevation of 20 m with base n

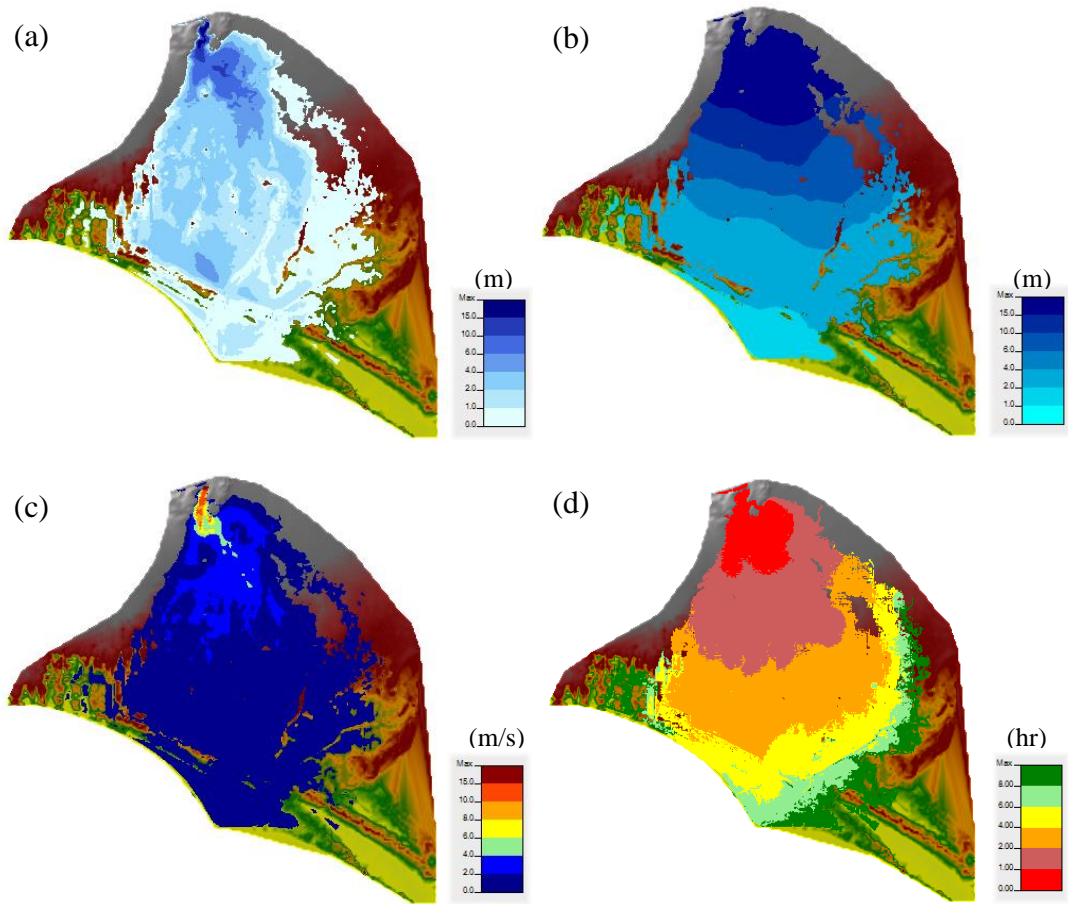


Figure B.3. Distribution of a) maximum depth of water, b) maximum water surface elevation, c) maximum velocity of water and d) flood arrival time for the piping elevation of 40 m with base n

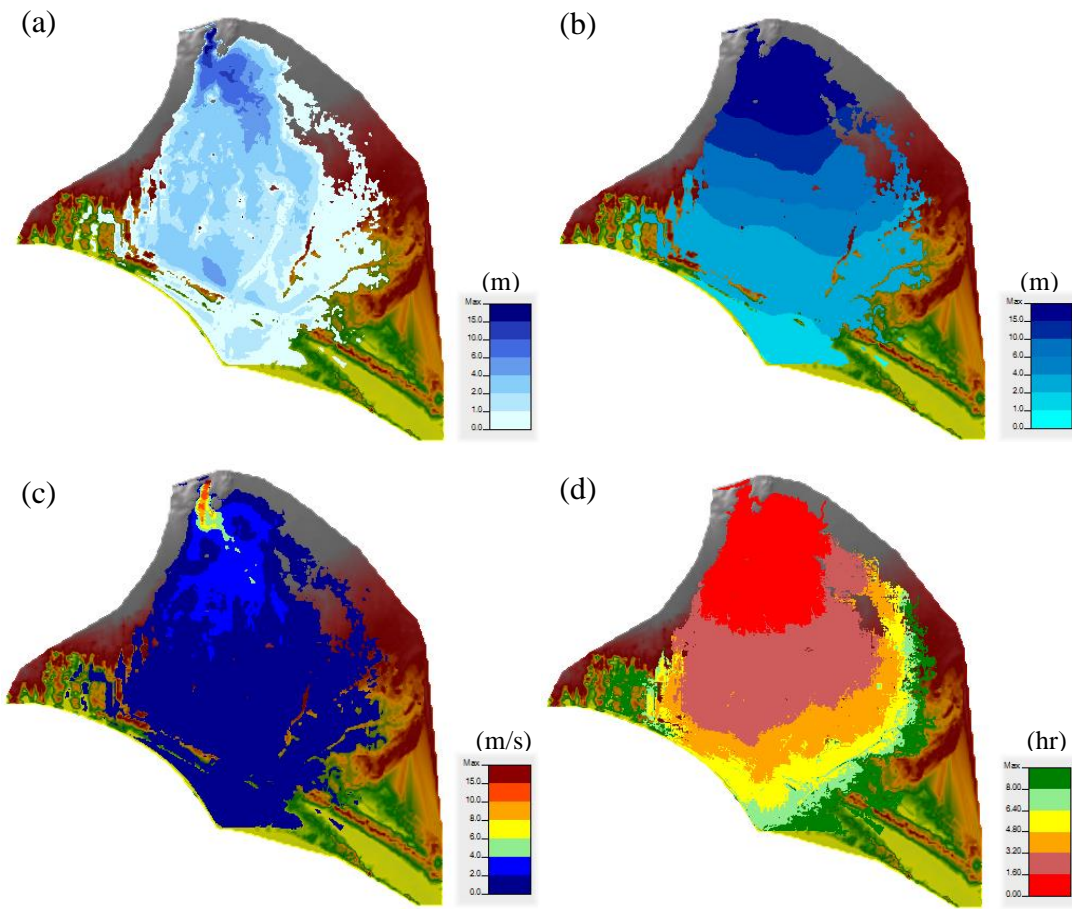


Figure B.4. Distribution of a) maximum depth of water, b) maximum water surface elevation, c) maximum velocity of water and d) flood arrival time for the piping elevation of 50 m with base n

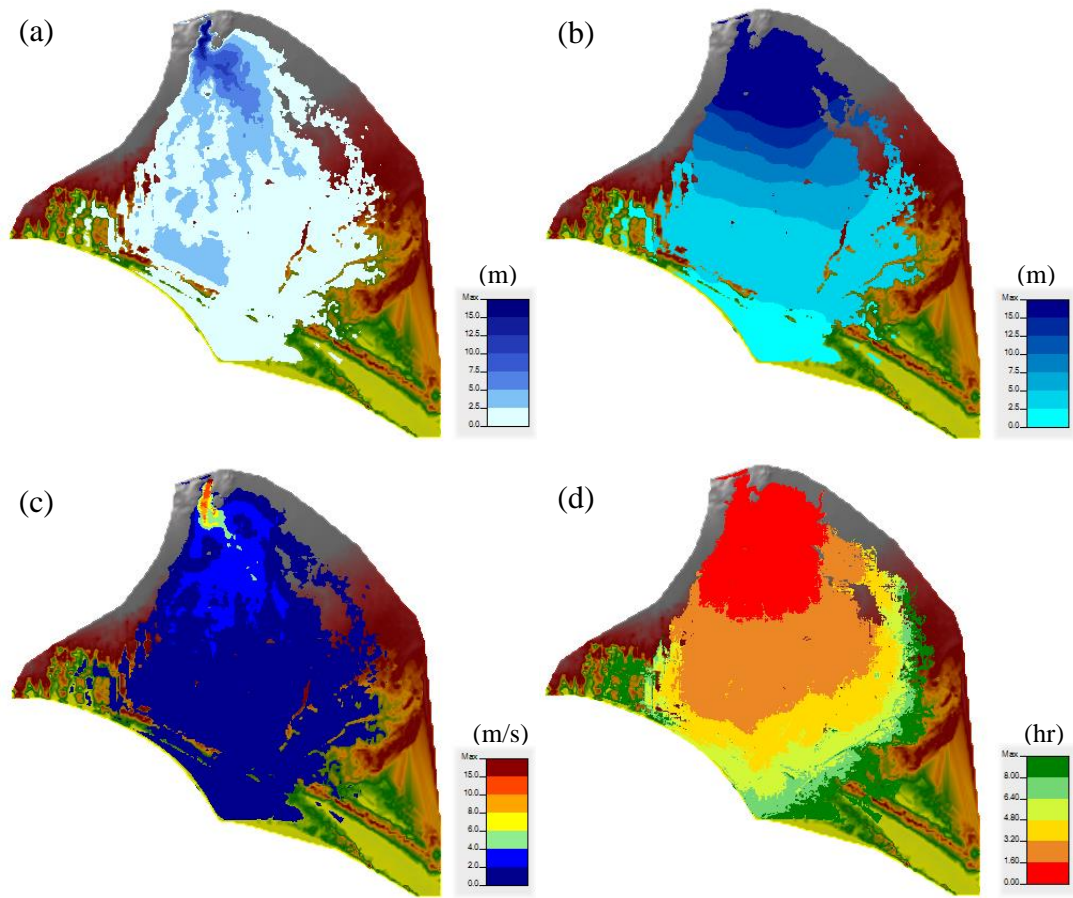


Figure B.5. Distribution of a) maximum depth of water, b) maximum water surface elevation, c) maximum velocity of water and d) flood arrival time for the piping elevation of 60 m with base n

C. Results of the Analyses for Different Initial Water Levels with Base n

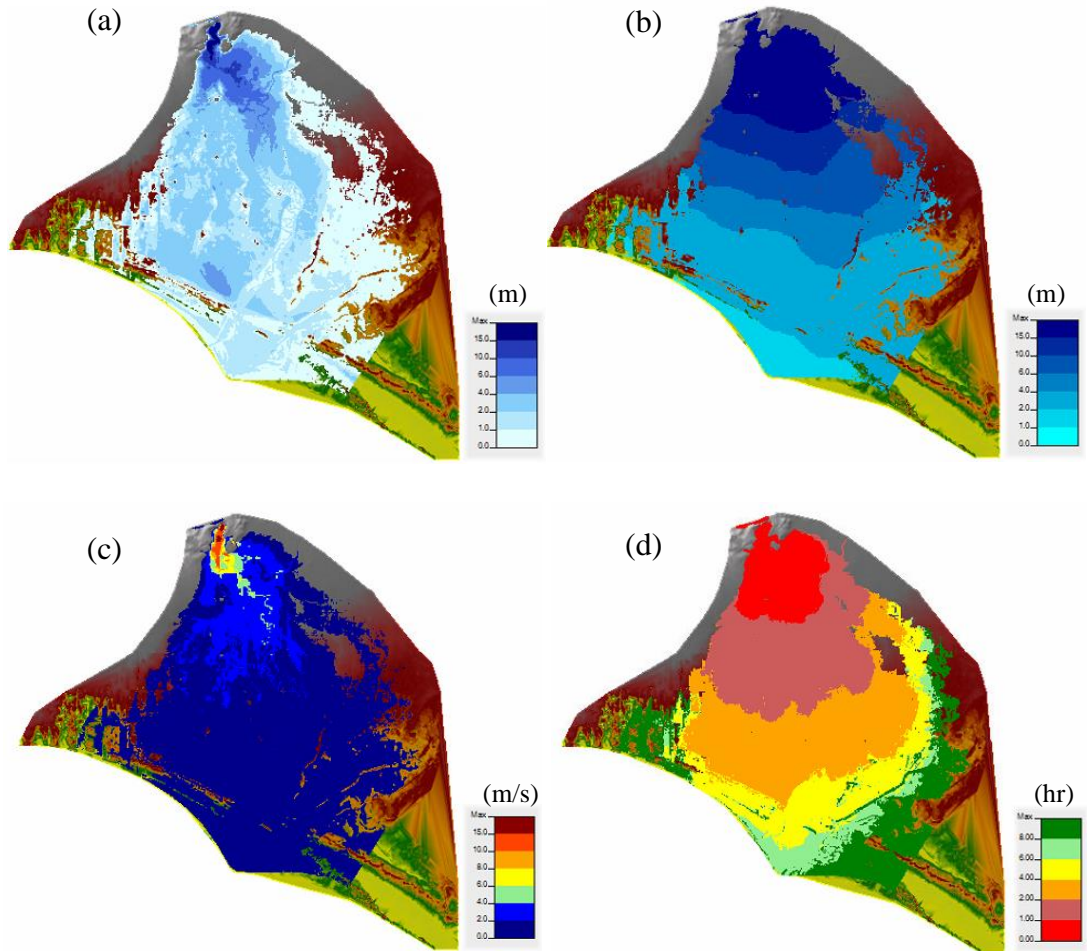


Figure C.1. Distribution of a) maximum depth of water, b) maximum water surface elevation, c) maximum velocity of water and d) flood arrival time for the initial reservoir water level of 71.6 m with base n (overtopping mode of failure)

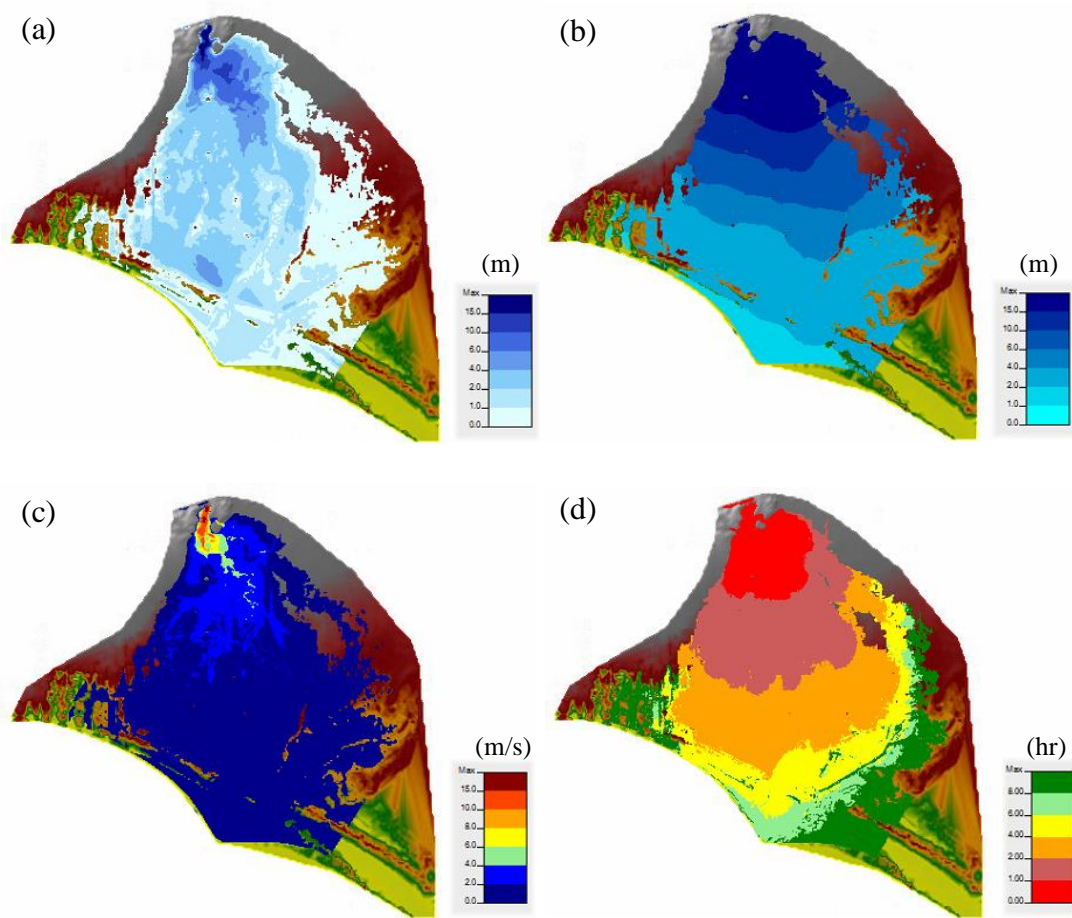


Figure C.2. Distribution of a) maximum depth of water, b) maximum water surface elevation, c) maximum velocity of water and d) flood arrival time for the initial reservoir water level of 71.8 m with base n (overtopping mode of failure)

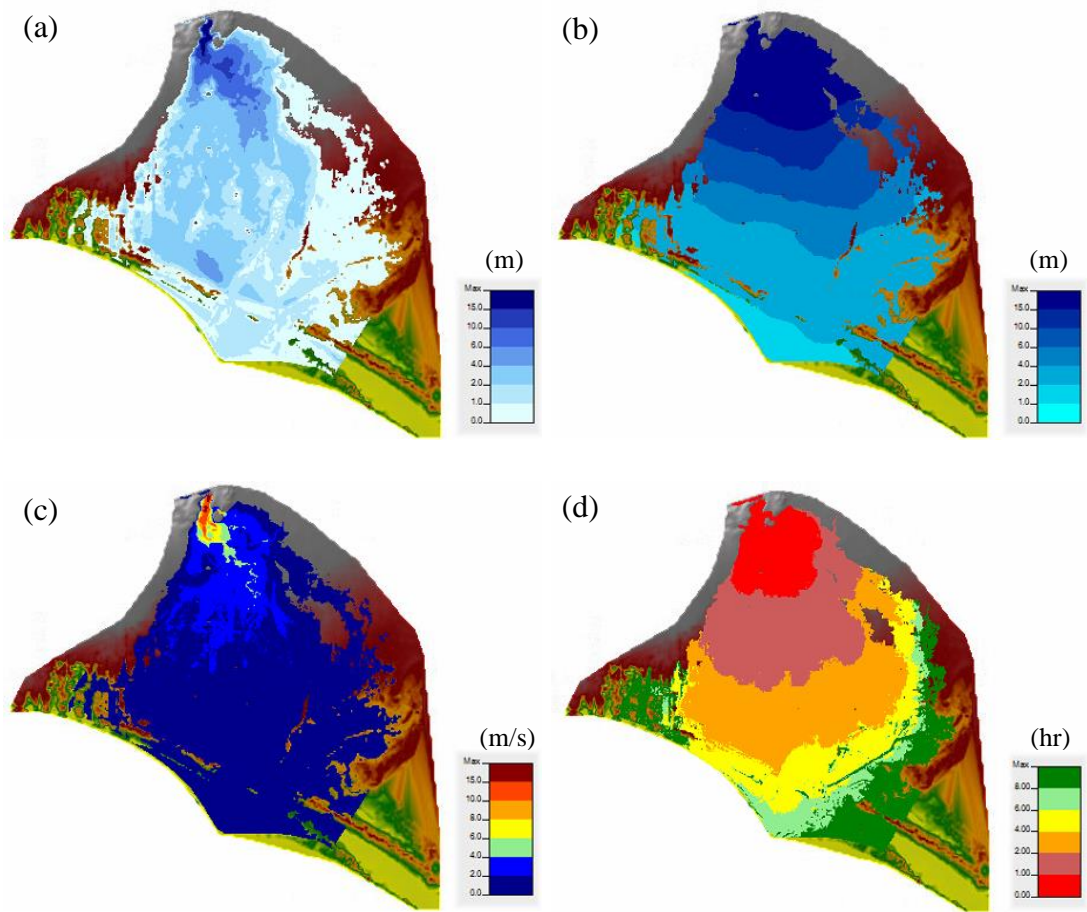


Figure C.3. Distribution of a) maximum depth of water, b) maximum water surface elevation, c) maximum velocity of water and d) flood arrival time for the initial reservoir water level of 72.2 m with base n (overtopping mode of failure)

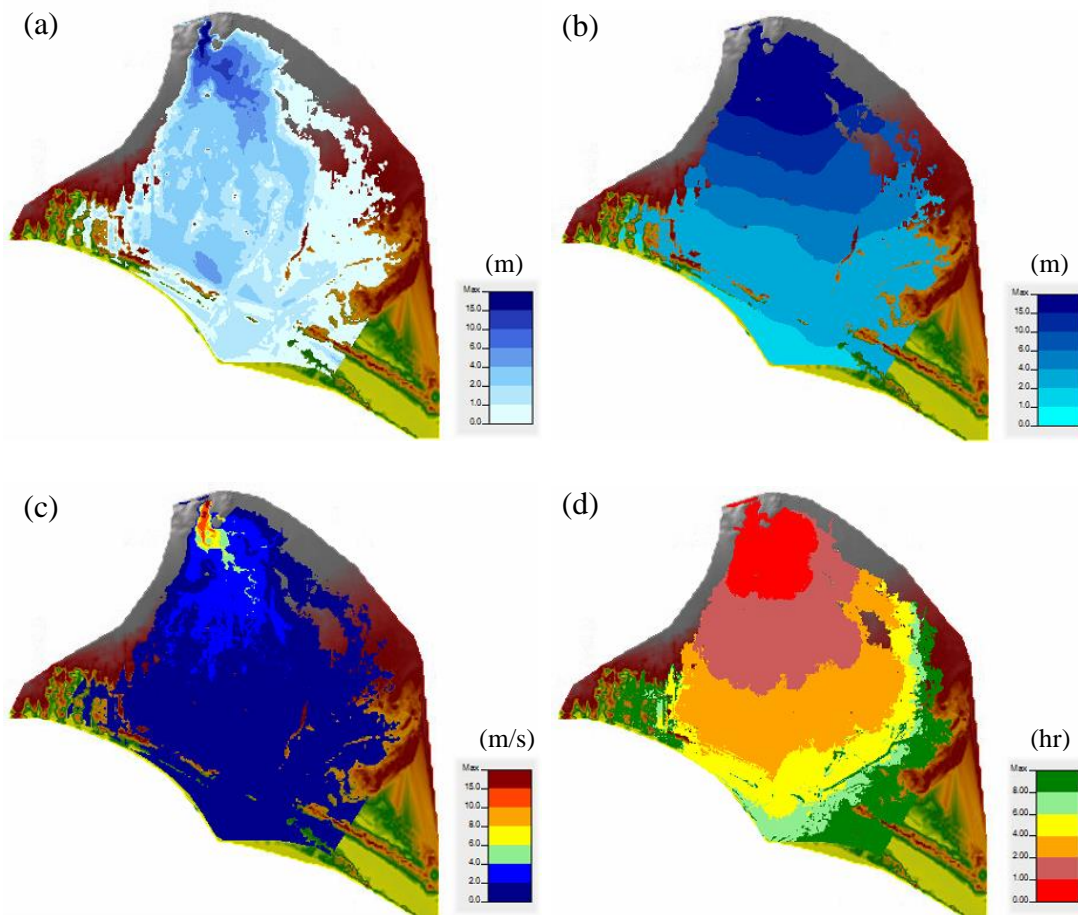


Figure C.4. Distribution of a) maximum depth of water, b) maximum water surface elevation, c) maximum velocity of water and d) flood arrival time for the initial reservoir water level of 72.4 m with base n (overtopping mode of failure)

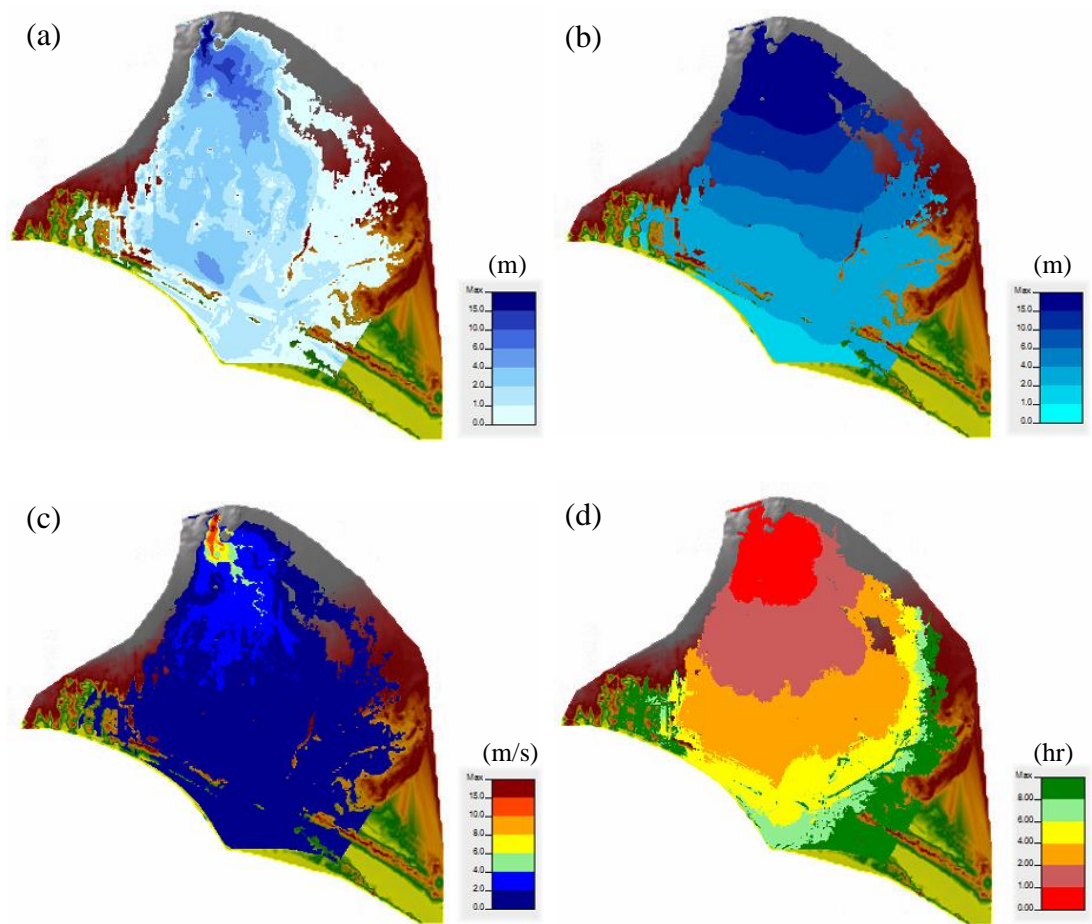


Figure C.5. Distribution of a) maximum depth of water, b) maximum water surface elevation, c) maximum velocity of water and d) flood arrival time for the initial reservoir water level of 72.6 m with base n (overtopping mode of failure)

D. Results of the Analyses for Different Initial Water Levels with $n=0.060$

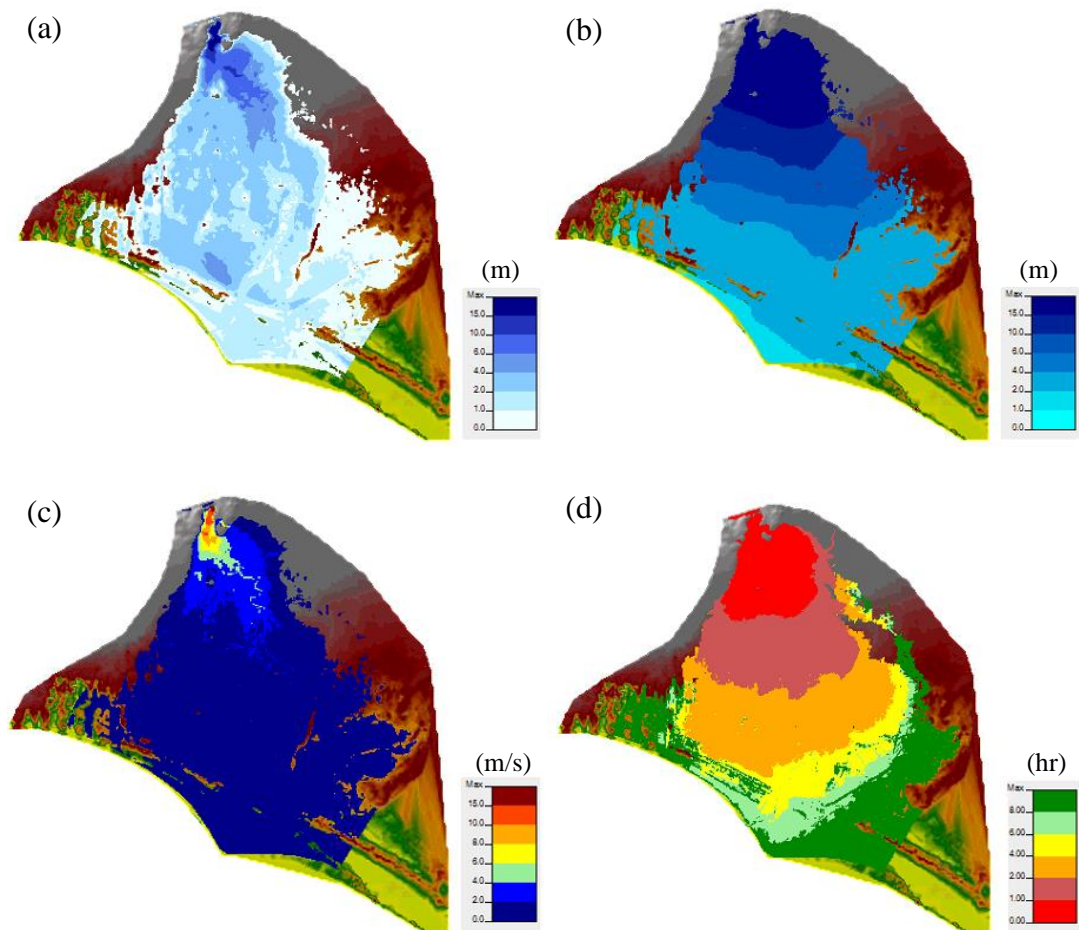


Figure D.1. Distribution of a) maximum depth of water, b) maximum water surface elevation, c) maximum velocity of water and d) flood arrival time for the of initial reservoir water level of 71.6 m with $n=0.060$ (overtopping mode of failure)

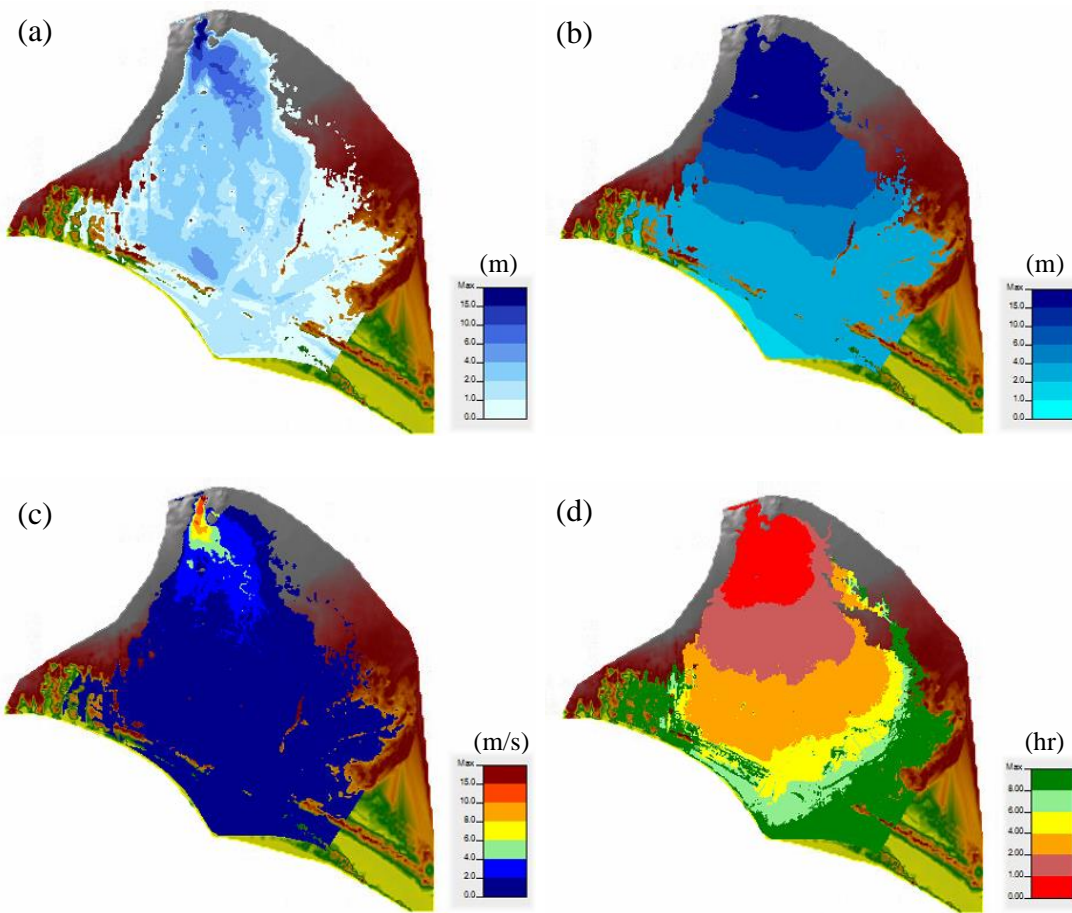


Figure D.2. Distribution of a) maximum depth of water, b) maximum water surface elevation, c) maximum velocity of water and d) flood arrival time for the initial reservoir water level of 71.8 m with $n=0.060$ (overtopping mode of failure)

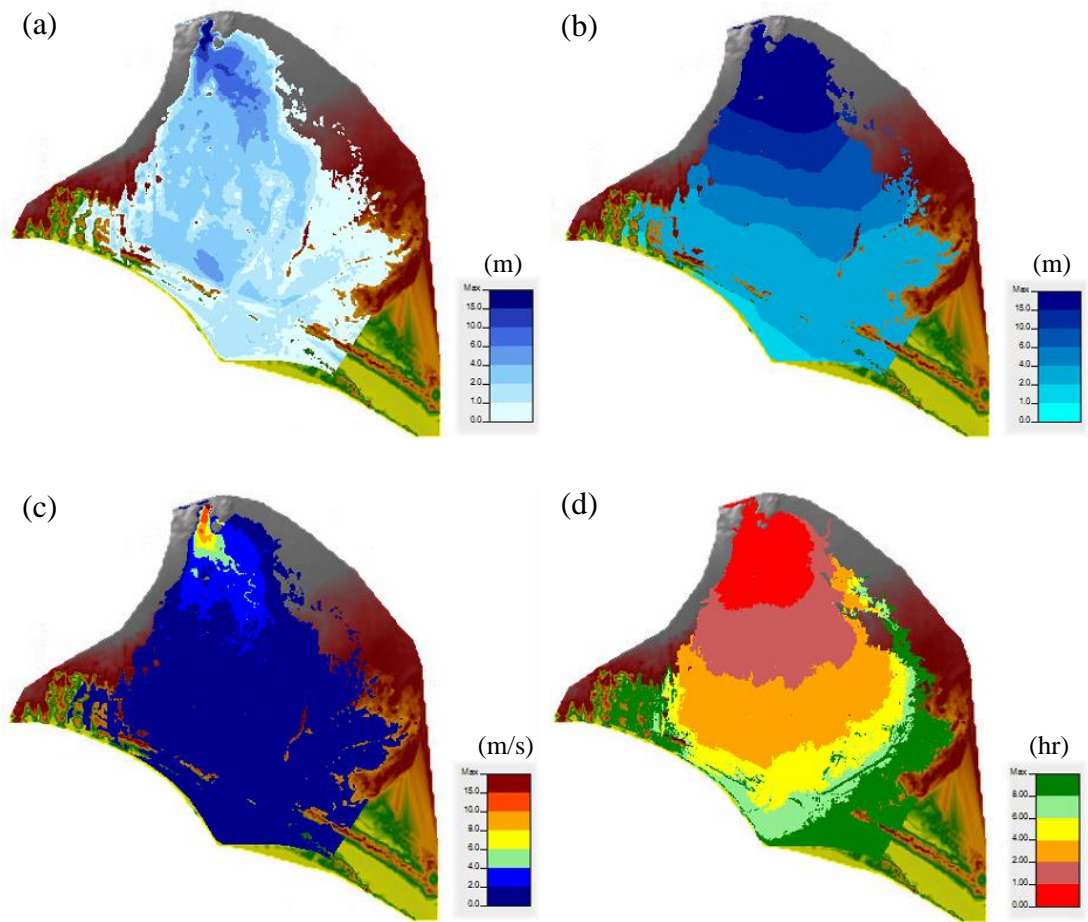


Figure D.3. Distribution of a) maximum depth of water, b) maximum water surface elevation, c) maximum velocity of water and d) flood arrival time for the initial reservoir water level of 72.2 m with $n=0.060$ (overtopping mode of failure)

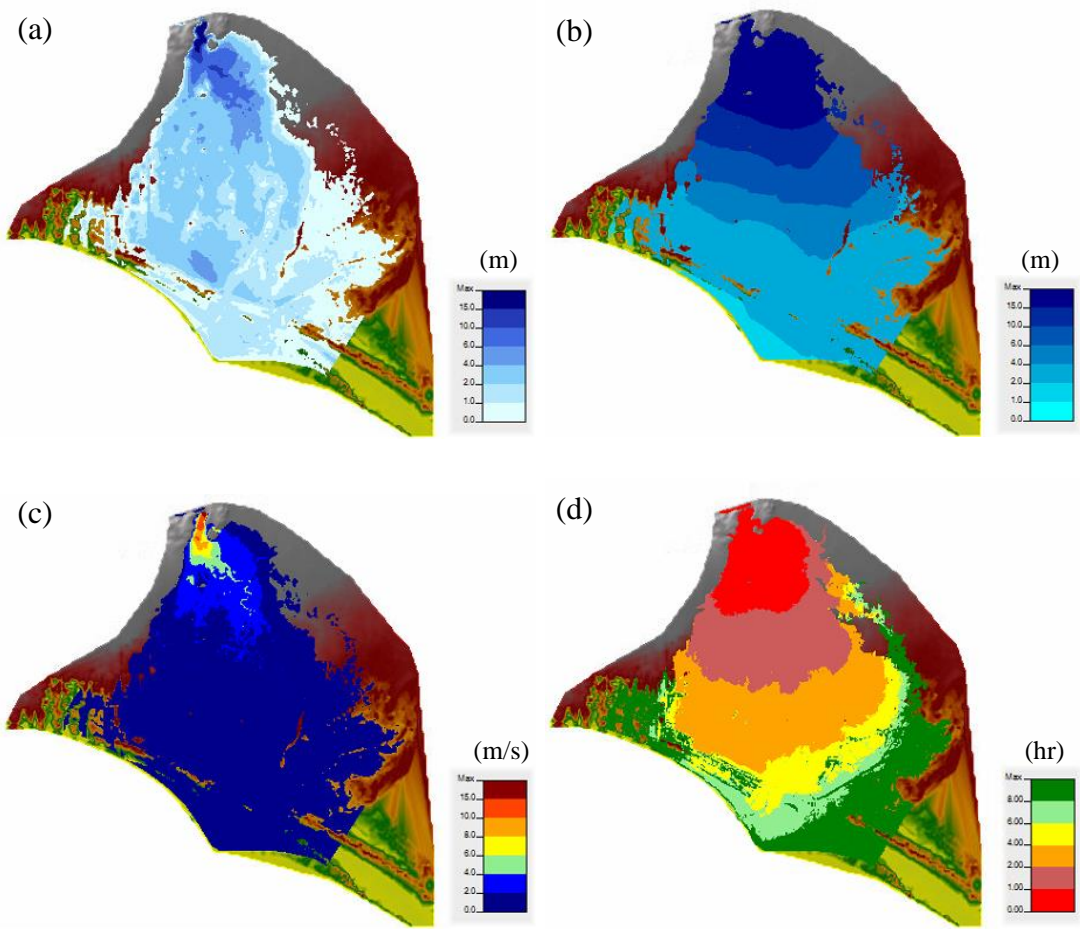


Figure D.4. Distribution of a) maximum depth of water, b) maximum water surface elevation, c) maximum velocity of water and d) flood arrival time for the initial reservoir water level of 72.4 m with $n=0.060$ (overtopping mode of failure)

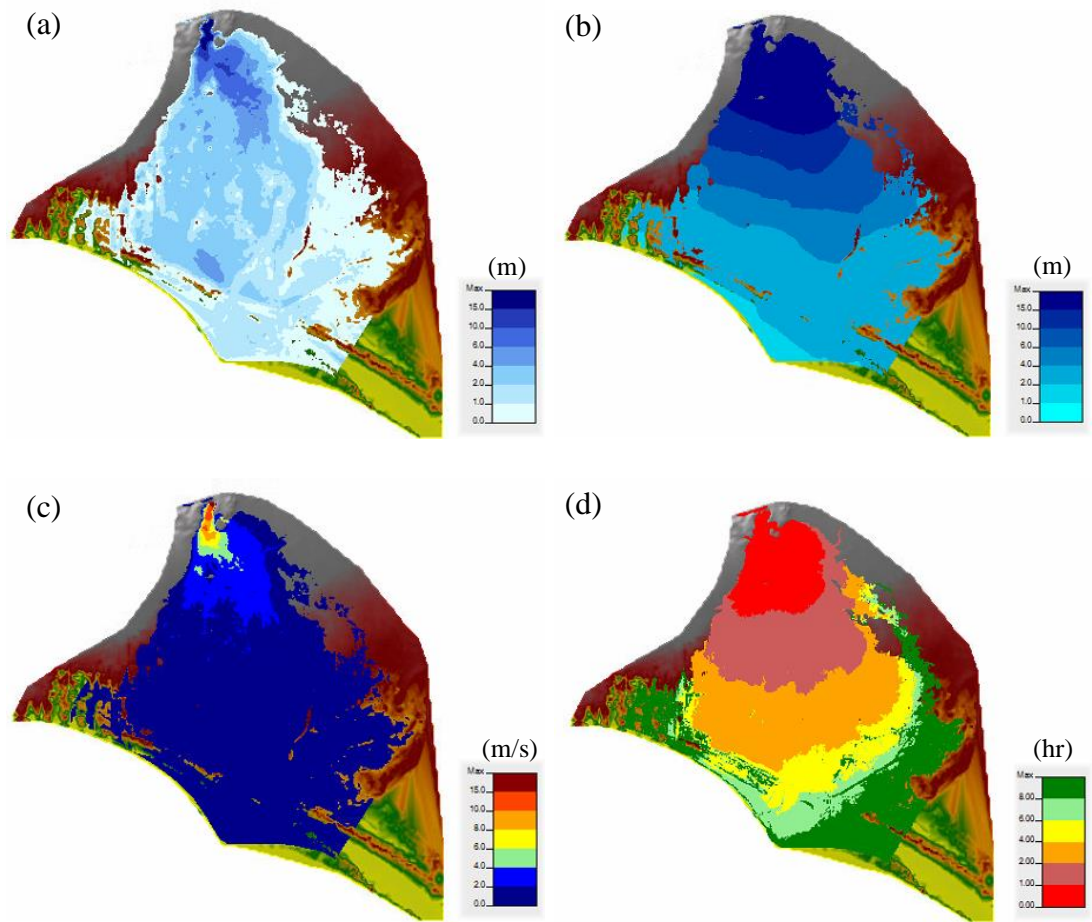


Figure D.5. Distribution of a) maximum depth of water, b) maximum water surface elevation, c) maximum velocity of water and d) flood arrival time for the initial reservoir water level of 72.6 m with $n=0.060$ (overtopping mode of failure)